University of California,
Irvine

The Search for Ultra-High Energy Neutrinos with AMANDA-II

Dissertation

submitted in partial satisfaction of the requirements
for the degree of

Doctor of Philosophy

in Physics

by

Lisa Marie Gerhardt

Dissertation Committee:
Professor Steven Barwick, Chair
Professor Gaurang Yodh
Professor Jonathan Feng

2007

The dissertation of Lisa Marie Gerhardt
is approved and is acceptable in quality and form for
publication on microfilm and in digital formats:

_____

_____

_____

Committee Chair

University of California, Irvine
2007

Dedication

This is dedicated to my family and friends:

My beloved husband Eric, for your constant faith and heart. I couldn't have done it without you and I definitely wouldn't have wanted to.

My mother, who was always proud of me.

My sister Jennifer, for endless phone calls, limitless support and for teaching me to knit.

My sister Stephanie, for constantly encouraging me.

My brother-in-law Chris, for the best darn quals good luck video bar none.

My nephew Rowan, for wearing all the dopey physics t-shirts I bought.

My friend Kyler, for helping me be a better scientist and person.

Finally, Murr and BoBear, who have been place-holders here so long it feels funny to leave them out.

Table of Contents

List of Figures

List of Tables

Acknowledgements

I would like to thank my advisor Dr. Steven Barwick for the suggestion to look for UHE neutrinos and his support and guidance during the search. There were many days when progress would have been impossible without his help. I thank Kyler Kuehn for his patient help with reading numerous papers and web pages and for being my sounding board.
I would like to thank everyone in the AMANDA and IceCube Collaborations for their help during this analysis. Specifically, I would like to thank Stephan Hundertmark for helping me to learn the AMASIM software, JiWoo Nam for numerous statistical discussions and Gary Hill for his help understanding the statistical uncertainties on zero events.
I would like to thank the University of California, Irvine MPC computational cluster, for making their systems available for signal simulation. I would also like to thank the Achievement Rewards for College Scientists (ARCS) for their support during my studies.

Curriculum Vitae

Lisa Gerhardt
Department of Physics & Astronomy
University of California, Irvine
4129 Frederick Reines Hall
Irvine, CA 92697-4575
949-824-3424
949-824-2174 fax
lgerhard@uci.edu

EDUCATION

Ph.D., Physics (Experimental Astroparticle), University of California, Irvine, August 2007.
Advisor: Dr. Steven Barwick
Thesis title: The Search for Ultra-High Energy Neutrinos with AMANDA-II
Master of Science, Physics, University of California, Irvine, 2000.
Bachelors of Science, Physics, University of California, Davis, 1998.
Bachelors of Arts, Geology, University of California, Davis, 1998.

RESEARCH EXPERIENCE

Doctoral Research, Department of Physics, University of California, Irvine, June 2000 - present.
Data Analysis

- Conducted search with the Antarctic Muon and Neutrino Detector Array (AMANDA) for neutrinos with energies in excess of 10^5 GeV against a background of muon showers from cosmic rays.
- Studied detector response in previously unexplored ultra-high energy region.
- Developed experimental background rejection procedures utilizing neural net and minimization software.
- Extended analysis to three years of data to generate the most stringent limit on neutrino flux at these energies to date.
- Mentored and assisted other graduate students.
- Presented results to scientific and nonscientific audiences.

Detector Simulation

- Created new Monte Carlo detector simulation Fortran code and modified existing code to incorporate effects specific to this analysis.
- Optimized existing Monte Carlo detector simulation code to decrease memory usage and to allow the user to modify many system features including detector size and photoelectron to amplitude ratio.
- Generated and analyzed high volumes of Monte Carlo simulation specific to this analysis.

Detector Calibration

- Compiled and maintained detector geometry and photon response data.
- Verified detector simulation response for high energy laser calibration blasts.

Research Assistant, Department of Physics, University of California, Davis, January - June 1997.

- Designed and constructed circuits for prototype testing for upgrades to the Collider Detector at Fermi lab (CDF).

TEACHING EXPERIENCE

Teaching Assistant, Department of Physics, University of California, Irvine, September 1999 - March 2005.
Gave classroom presentations of basic physics concepts and solved problems for introductory physics courses. Prepared and evaluated homework and exams.
Teaching Assistant, Department of Physics, University of California, Davis, September 1997 - January 1998.
Led interactive discussion sessions for introductory physics course for non-physics majors.

TECHNICAL SKILLS

Proficient in C, Fortran, PAW, zsh and tcsh scripts. Familiar with C++ and ROOT. Conversant with Linux, UNIX and OS X. Experienced with data reduction and analysis techniques. Adept at handling and analyzing large volumes of data and long-running simulation chains.

HONORS AND AWARDS

Achievement Rewards for College Scientists (ARCS) Scholar, 2002 - 2004
University of California, Davis Dean's List, 1994 - 1995 Hubert Wakeham Scholarship, 1993

PRESENTATIONS

"Three Year Search for Ultra-high Energy Neutrinos using AMANDA-II," presented at the American Physical Society Annual Meeting, Jacksonville, FL, April 2007.

"Search for Ultra High Energy Neutrinos with AMANDA," presented at the 14th International Conference on Supersymmetry and the Unification of Fundamental Interactions, Irvine, CA, June 2006.

"Search for Ultra-high Energy Neutrinos with AMANDA-II," presented at the American Physical Society Annual Meeting, Dallas, TX, April 2006.

"Sensitivity of AMANDA-II to UHE Neutrinos," presented at the 29th International Cosmic Ray Conference, Pune, India, August 2005.

"Search for Extremely High Energy Neutrinos with AMANDA-II," presented at the American Physical Society Annual Meeting, Tampa, FL, April 2005.

"The Search for Ultra-high Energy Neutrinos with AMANDA," presented at the American Physical Society Annual Meeting, Denver, CO, May 2004.

Achievement Rewards for College Scientists (ARCS) Scholar, 2002 - 2004.
Award required explaining research to foundation members and invited guests at numerous luncheons and poster sessions.

Numerous presentations at AMANDA and IceCube collaboration meetings of up to 100 other graduate students and professors, detailing progress in research or new simulation algorithms, June 2000 - present.

SELECTED PUBLICATIONS

L. Gerhardt for the IceCube Collaboration, "Search for Ultra-High Energy Neutrinos with AMANDA-II," The Astrophysical Journal, in preparation.

L. Gerhardt for the IceCube Collaboration, "The Search for UHE Neutrinos with AMANDA-II," Proceedings of the 14th International Conference on Supersymmetry and the Unification of Fundamental Interactions, in publication.

L. Gerhardt for the AMANDA Collaboration, "Sensitivity of AMANDA-II to UHE Neutrinos," Proceedings of the 29th International Cosmic Ray Conference, 5: 111-114 (2005). Ackermann et al (AMANDA collaboration), "Flux Limits on Ultra High Energy Neutrinos with AMANDA-B10," Astroparticle Physics 22:339-353 (2005)

Ackermann et al (AMANDA collaboration), "Search for Extraterrestrial Point Sources of High Energy Neutrinos with AMANDA-II using Data Collected in 2000-2002," Physics Review D 71:077102 (2004)

Ackermann et al (AMANDA collaboration), "Search for Neutrino-Induced Cascades with AMANDA," Astroparticle Physics 22:127-138 (2004)

Ahrens et al (AMANDA and SPASE collaboration), "Calibration and Survey of AMANDA with the SPASE Detectors," Nuclear Instruments and Methods A, 522:347-359 (2004)

Ahrens et al (AMANDA collaboration), "Muon Track Reconstruction and Data Selection Techniques in AMANDA," Nuclear Instruments and Methods A 524:169-194 (2004)
Ahrens et al (AMANDA and SPASE collaboration), "Measurement of the Cosmic Ray Composition at the Knee with the SPASE-2/AMANDA-B10 Detectors," Astroparticle Physics 21:565-581 (2004)
Ahrens et al (AMANDA collaboration), "Search for Extraterrestrial Point Sources of Neutrinos with AMANDA-II," Physics Review Letters 92:071102 (2004)
Ahrens et al (AMANDA collaboration), "Limits on diffuse fluxes of High-Energy Extraterrestrial Neutrinos with the AMANDA-B10 detector," Physics Review Letters 90:251101 (2003)
Ahrens et al (AMANDA collaboration), "Search for Point Sources of High Energy Neutrinos with AMANDA," Astrophysical Journal 583:1040-1057 (2003)
Ahrens et al (AMANDA collaboration), "Results from AMANDA," Modern Physics Letters A 17:2019-2037 (2002)

Abstract of the Dissertation

The Search for Ultra-High Energy Neutrinos with AMANDA-II

By

Lisa Marie Gerhardt

Doctor of Philosophy in Physics

University of California, Irvine, 2007

Professor Steven Barwick, Chair

A search for non-localized neutrinos with energies in excess of 10^5 GeV was conducted with 456.8 days of AMANDA-II data recorded between 2000 and 2002. Above 10^7 GeV the Earth is essentially opaque to neutrinos. This, combined with the limited overburden above the AMANDA-II detector (roughly 1.5 km), concentrates these ultra-high energy neutrinos at the horizon. The primary background for this analysis is bundles of downgoing, high-energy muons from the decay of cosmic rays in the atmosphere. Since no statistically significant excess above the expected background was seen in the data, an upper limit on the flux of $E^2\,\Phi_{90\%CL} < 2.7 \times 10^{-7}$ GeV cm^{-2} s^{-1} sr^{-1} valid over the energy range of 2×10^5 GeV to 10^9 GeV is set on the diffuse flux of the sum of all three flavors of neutrinos. A number of models which predict neutrino flux from active galactic nuclei are excluded at the 90% confidence level by this analysis.

Chapter 1

Introduction

1.1 Why Neutrinos?

The detection of neutrinos is one of the few methods available for studying distant astrophysical objects with energies in excess of 10^5 GeV. This ultra-high energy (UHE) region remains largely unexplored by conventional astronomical methods for a number of reasons. Photons, the traditional workhorse of astronomy, are not ideal for imaging the UHE universe. Distant, high energy photons will annihilate with the cosmic microwave background (CMB) and produce e^+/e^- pairs. Due to this interaction, photons from the Galactic Center with energies above 10^6 GeV will not reach the Earth [57]. For more distant objects, this cutoff begins at lower energies (Fig. 1.1).

Likewise, UHE cosmic rays from distant objects will also interact with the CMB via the reaction first proposed by Greisen [38], Zatsepin and Kuzmin [90]

$$p + \gamma \rightarrow \Delta \rightarrow \pi^+ + n \tag{1.1}$$

This GZK mechanism predicts that cosmic rays with energies in excess of 10^{10} GeV will be fully degraded into lower energy particles after traveling about 50 Mpc [57]. Additionally, cosmic rays are bent by the ambient magnetic field of the universe, so the lower energy cosmic rays which do reach the Earth do not point back to their sources.

Neutrinos do not suffer from any of these disadvantages. They interact only through the weak interaction, with a cross section on the order of 10^{-33} cm^2 for

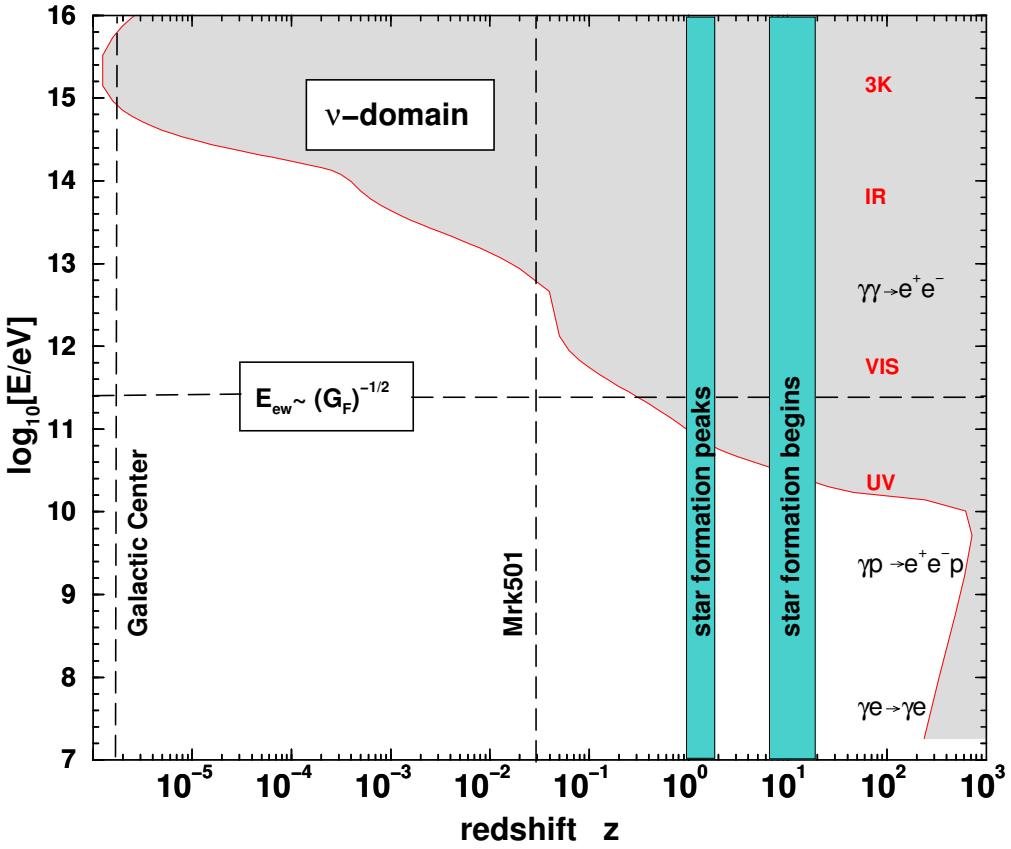

Figure 1.1: Gamma-ray absorption processes as a function of red shift. The shaded areas are invisible to gamma-ray astronomy. Figure taken from [57].

neutrino energies greater than 10^5 GeV (Fig. 1.2). Their small cross sections allow them to pass through the CMB (as well as other more solid barriers such as dust clouds and stellar coronae). Neutrinos can travel long distances and pass through barriers which would stop more volatile photons or cosmic rays. Neutrinos are neutral, so they will not be bent by magnetic fields. These characteristics make neutrinos ideal for astronomical observations. They can fill in gaps left by observations of photons and cosmic rays, supplement existing observations, and provide new insight into the UHE universe.

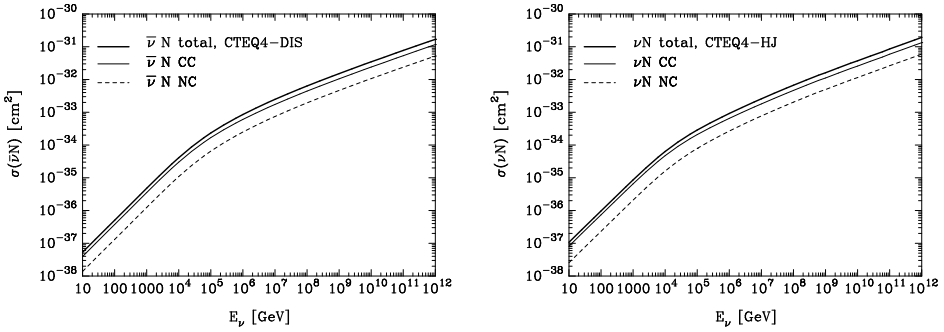

Figure 1.2: Anti-neutrino (left) and neutrino (right) interaction cross sections as a function of energy. Figures taken from [35].

1.2 UHE Neutrino Sources

This work describes the search for neutrinos with energies above 10^5 GeV. These neutrinos are of interest because they are associated with the potential acceleration of hadrons by active galactic nuclei [39, 61, 62, 69, 76, 77, 75], they could potentially be produced by the decays of exotic phenomena such as topological defects [70] or the interaction of energetic neutrinos with relic neutrinos via the Z-burst [49, 87], and they are guaranteed by-products of the interactions of high energy cosmic rays with the cosmic microwave background [31, 50].

1.2.1 Active Galactic Nuclei

Active Galactic Nuclei (AGN) are highly luminous objects that are isotropically distributed throughout the sky. Their total luminosity ranges between 10^{42} erg/s and 10^{48} erg/s [34]. It is theorized that these enormous energies are fueled by gravitational energy released as matter accretes onto a central black hole with a mass of at least 10^8 $M_\odot$ [57]. AGNs emit photons in non-thermal spectra spanning over 20 orders of magnitude, with luminosities as high as 10^{46} erg/s per decade of energy [34]. Black body radiation consistent with emissions from the last stable orbit of material around the black creates a characteristic "UV bump" in the

spectrum. AGNs can also have jets along the axis of rotation which are strong emitters in the radio spectrum. These jets are composed of highly beamed sheets of matter traveling with a bulk Lorentz factor of $\gamma \approx 10$. Variations in jet emission intensity on the order of a day have been observed [39], which provides a rough estimate of the size of the sheet of $\Gamma c\Delta t = 10^{-2}$ pc. AGNs are typically classified according to the fraction of energy emitted in the radio spectrum, with 10% of AGNs considered "radio-loud" and the rest "radio-quiet." Roughly 1% of all bright galaxies contain an AGN [57].

Charged particles in AGNs are accelerated via Fermi acceleration in which a charged particle scatters repeatedly across a shock front, gaining energy from the shock front's kinetic energy. On average, these particles gain energy and the change in energy is proportional to the square of the velocity of the shock front. Some particles scatter away from the shock and the statistical equilibrium between escape and acceleration yields an energy spectrum of

$$dN = N_0 E^{-s} dE \tag{1.2}$$

with

$$s = 2 + \frac{4}{M^2} \tag{1.3}$$

where M is the Mach number. For typical ultrarelativistic shock speeds, the theoretical prediction for s is roughly 2.2 - 2.4, leading to a spectrum that goes roughly as E^{-2} [57]. In order for Fermi acceleration to operate, several conditions must be met:

the energy loss per unit time from scattering and synchrotron radiation must be less than the energy gain from scattering across the shock

the scattering length must be less than the shock radius

the lateral diffusion time scale must be greater than the acceleration time scale

the shock thickness must be smaller than the particle's gyroradius, and both must be smaller than the particle's Coloumb mean free path

If the charged particle is a proton, neutrinos can be produced via the reaction in equation 1.1. The maximum possible energy of the neutrino that can be produced from this is on the order of 10^9 GeV [34].

AGN models are classified according to where the acceleration of particles takes place. In "core" or "hidden core" AGN models, first described in detail by Stecker et al. [76], protons are accelerated inside of the cores of radio-quiet AGNs. Here, infalling matter forms an accretion shock some distance from the black hole. Protons are accelerated to energies as high as 25×10^9 GeV by Fermi-acceleration with this shock front. It is known from the lack of absorption features in the x-ray spectrum that the x-rays are produced in the regions of low gas density, which limits the number of lower-energy protons available for proton-proton interaction, leaving p-γ as the dominant energy loss process for these accelerated protons via Eqn. 1.1. The high photon density (particularly at the energies that make up the UV bump) ensures that the secondary neutrons will interact before they escape the core region via the process

$$n + \gamma \rightarrow \pi^0 + X \tag{1.4}$$

Roughly half the energy loss goes into generation of $\pi^{\pm}$'s (via Eqn. 1.1) and half goes into π^0's (Eqn. 1.4).

Initial observations indicated the emitted x-ray spectrum was consistent with electromagnetic cascades from the secondaries created in Eqn. 1.4. Since the ratio between neutrino luminosity and x-ray luminosity is known, the generated neutrino flux can be normalized to the AGNs' x-ray spectrum. In Stecker et al.

[76] the neutrino flux was normalized to the diffuse x-ray luminosity as measured by the GINGA satellite with the assumption that all of the x-ray background was non-thermal radiation from AGNs. However, this number has been updated to reflect more recent observations of AGN spectra, which indicate the x-ray emission is thermal and not directly associated with high energy particles [75]. Instead the neutrino flux is normalized using the assumption that 10% of the diffuse extragalactic MeV background is produced from the decay of energetic π^0 accelerated in AGNs. This produces a neutrino flux that is a factor of 10 lower than the flux predicted in [76] and is shown in Fig. 1.3 labeled "St05".

In contrast to the hidden core model of AGNs, jet models accelerate particles in highly relativistic jets. In this model, protons are accelerated via Fermi acceleration at shock fronts in the sheets of matter which make up the jet. The AGNs emission spectrum is produced by interaction of these protons with the ambient radiation in the AGN. In Protheroe [69] the protons interact with photons radiated from the accretion disk and the neutrino flux is estimated using the luminosity function for blazars measured by EGRET [27] integrated over redshift and luminosity. Mannheim [61] gives an estimate for the neutrino flux for a model in which both protons and electrons are accelerated in the jets of radio-loud AGNs. Neutrinos are generated from the interaction of the accelerated protons with synchrotron photons produced by the electrons. Two neutrino fluxes are calculated, normalized to the diffuse gamma-ray background above 100 MeV and to the diffuse gamma-ray background from 1 MeV to 100 MeV. A model independent estimate of the flux of neutrinos from AGN jets using only observed parameters has been calculated in Halzen & Zas [39]. Here the neutrino flux is normalized to the gamma-ray luminosity function of AGNs measured by EGRET [27]. These three models produce fluxes of neutrinos that are in rough agreement in shape and normalization because similar values are used for the dominant

parameters in the flux calculation, such as the accelerated proton spectrum, the maximum proton energy and the magnetic field, which are either natural outflows of the mechanism used or the result of simple dimensional analysis of the AGN emission. A maximal model for neutrino flux from blazars has been proposed in Mannheim et al. [62]. The model calculates the maximum possible neutrino flux that is consistent with theoretical bounds (see sect 1.4) using source evolution functions for blazars and varying the energy at which the cosmic ray spectrum has a change in spectral slope. Because this model uses more recent cosmic ray flux estimates to normalize the neutrino spectrum and because it assumes the some of the blazars are transparent to neutrons, the flux is generally an order of magnitude below the predictions of the previous models. The fluxes of these AGN models are shown in Fig. 1.3.

Electrons may also be accelerated in AGN jets, but descriptions of these models are omitted here because they do not lead to the production of neutrinos.

1.2.2 GZK Neutrinos

GZK neutrinos are named after Greisen [38], Zatsepin and Kuzmin [90] who first proposed that high energy cosmic rays would interact with the ambient cosmic microwave background (CMB) and lose a significant fraction of their energy before they reach the Earth. Since the highest energy cosmic rays are thought to be extragalactic, this theory predicts a marked decrease in the flux of cosmic rays above $\sim 5 \times 10^{10}$ GeV, commonly referred to as the GZK cutoff. There is some controversy surrounding the existence of the GZK cosmic ray cutoff. Although the theory is well-accepted, some experimental measurements seem to contradict its predictions (Fig. 1.4).

A number of detectors have measured the flux of cosmic rays above 10^{10} GeV, most recently HiRes which searched for fluorescent light from extensive cosmic

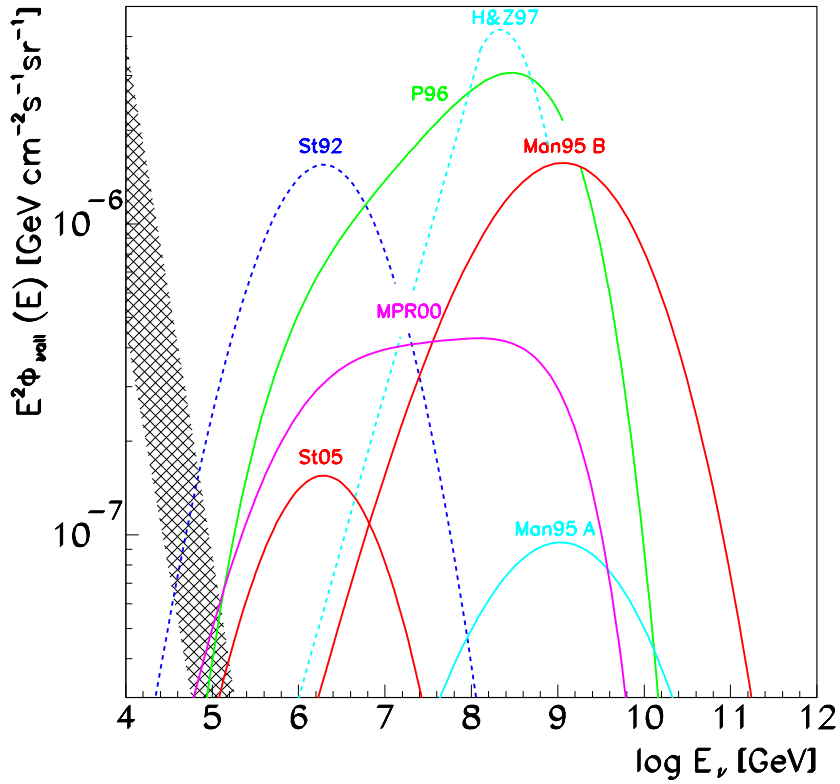

Figure 1.3: All flavor neutrino fluxes for various AGN models. The key is as follows: St05 from [75], St92 from [76], P96 from [69], MPR00 from [62], Man95 A & B from [61], and H&Z97 from [39].

ray air showers in the atmosphere [2], AGASA which used a ground array to measure the number of secondary leptons produced in a cosmic ray shower [40] and Auger which uses both techniques [4]. Measurements from AGASA show a spectrum that is consistent with no GZK cutoff [40], while measurements from HiRes see a cosmic ray spectrum consistent with a GZK cutoff to within 5σ [3]. Initial measurements from the Auger detector seem to confirm the existence of a GZK cutoff, but they are still in the early stages of data analysis and collection [73] (Fig. 1.4).

The same interaction which prevents high energy cosmic rays from reaching the Earth will also produce neutrinos (via the reaction in Eqn. 1.1). Detection of

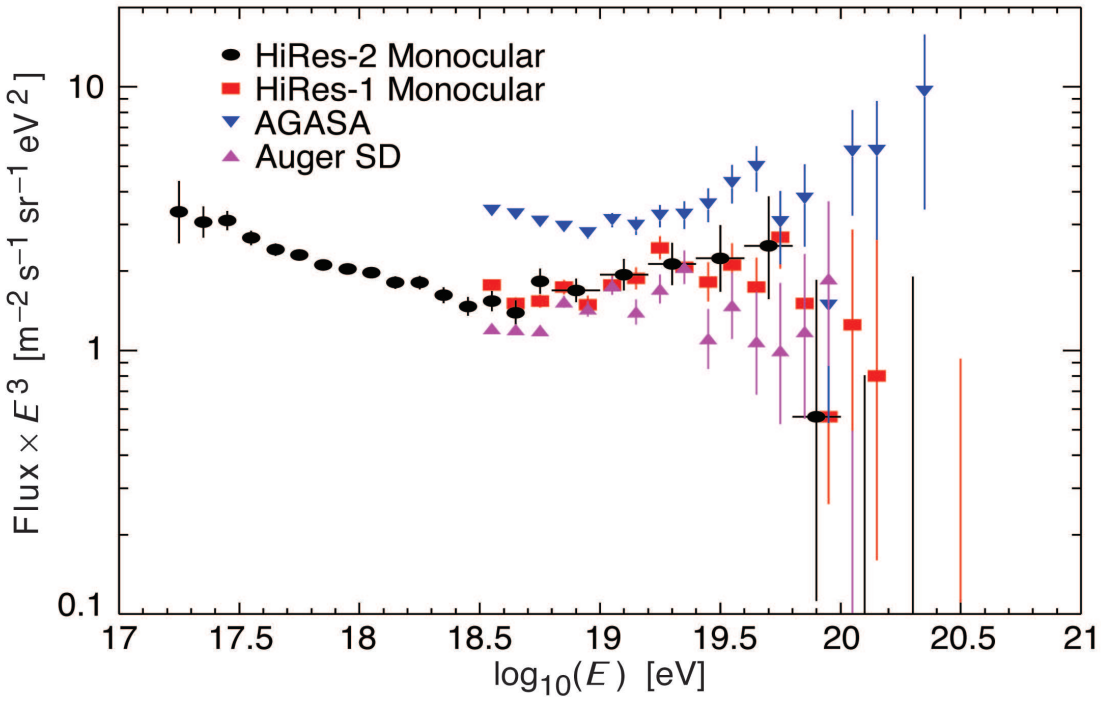

Figure 1.4: Highest energy cosmic ray fluxes measured in various experiments: HiRes-1 and -2 Monocular from [2], AGASA from [40], and Auger from [73]. Figure is taken from [67].

these neutrinos would help resolve the uncertainty surrounding the highest energy cosmic rays. However, estimates of the flux of these GZK neutrinos vary widely depending on the spectrum, evolution, maximum proton energy, and normalization of cosmic rays. A number of different approaches are used to calculate the expected neutrino flux.

In Engel et al. [31], the flux of neutrinos at the Earth is calculated for uniformly distributed sources with identical proton injection spectra. The neutrino yield per proton is calculated using the SOPHIA Monte Carlo code [66]. The cosmic ray energy spectrum used is

$$\frac{dN}{dE} = P_0 E^{-2} \times exp(-E/E_c) \tag{1.5}$$

where $P_0 = 4.5 \pm 1.5 \times 10^{44}$ erg/Mpc^3/yr is taken from Waxman [80] and E_c is assumed to be $10^{12.5}$ GeV. The effects of cosmological evolution are accounted for

by applying a parameterization taken from Waxman [80]

$$\mathcal{H}(z) = \begin{cases} (1+z)^n, & z < 1.9, \\ (1+1.9)^n, & 1.9 < z < 2.7, \\ (1+1.9)^n \exp\{(2.7-z)/2.7\}, & z > 2.7 \end{cases} \tag{1.6}$$

with n=3. By varying the parameters used in this calculation within their uncertainties, the muon neutrino flux was shown to vary by as much as a factor of 3. The conservative flux predicted by this calculation (using n=3, E_c =10^{13} GeV, Λ = 0.7 and P_0 as given above) is shown in Fig. 1.5 labeled "GZK (Eng01)".

In Kalazhev et al. [50], a different method is used. Here two independent Monte Carlo codes are used to propagate nucleons, gamma-rays, electrons and neutrinos from their sources to the Earth accounting for all relevant interactions. The injection spectrum of protons is given by

$$\phi(E,z) = f(1+z)^m E^{-\alpha} \Theta(E_{max} - E),\ z \leq z_{max} \tag{1.7}$$

where f is a normalization factor, and the free parameters are

m, the redshift evolution index

E_{max}, the maximum energy of the accelerated protons

z_{max}, the maximum redshift

α the spectra index of the accelerated protons

As these free parameters are varied, the resulting fluxes of all particles are normalized so that the flux of nucleons is below the observed cosmic ray spectrum and the flux of gamma-rays is below the observed gamma-ray background measured by EGRET [74]. The maximal neutrino fluxes are shown in Fig. 1.5 labeled GZK mono (maximal values used are m=4, z_{max}=3, α=0, and

E_{max}=10^{12} GeV) and GZK α=2 (maximal values used are m=5, z_{max}=3, α=2, and E_{max}=10^{13} GeV) and are an order of magnitude higher than the conservative calculations from Engel et al. [31] described above.

1.2.3 Top-Down Models

In contrast to AGN models, top-down models start with a highly massive object which decays or interacts and produces showers of standard model particles, including neutrinos. These objects could be gauge bosons, Higgs bosons, superheavy fermions, magnetic monopoles, cosmic necklaces or a number of other non-standard model physics particles. Generally these models are proposed to explain the apparent lack of a GZK cutoff in the flux of high energy cosmic rays (Fig. 1.4). In Sigl et al. [70], an "object-independent" approach is followed, where the fluxes of nucleons, gamma-rays and neutrinos are calculated for a particle of mass m_X with an injection rate of

$$\frac{dn_x}{dt} \propto t^{-3} \tag{1.8}$$

which is consistent with the theoretical expectations of injection rate for a number of exotic objects. The resulting particles are propagated to the Earth where their fluxes of particles are normalized to gamma-ray observations from EGRET [74]. Figure 1.5 shows the all flavor prediction with m_X = 10^{16} GeV and an extragalactic magnetic field of 10^{-10} G (labeled "TD (Sig98)").

1.2.4 Z-Bursts

Z-burst models use highly energetic neutrinos as the progenerating particles. Neutrinos with energies in excess of 10^{13} GeV will interact with relic neutrinos through the Z resonance if the neutrino has a mass in the 0.1 to 10 eV range [82].

Those high energy neutrinos which do not interact could be detected at the Earth. Z-burst models may be able to explain the highest energy cosmic rays, but the mechanism for accelerating the neutrinos to the high energies necessary to reach the Z resonance is unknown. In Yoshida et al. [87] the hadrons from a Z-burst are propagated to the Earth including effects of interactions with the CMB, and the infrared, optical and universal radio background. These simulations used a number of free parameters including the redshift evolution index, the strength of the extragalactic magnetic field, and the mass of the neutrino. The resulting gamma-ray fluxes at the Earth for each model were required to be consistent with the flux measured by EGRET [74]. Models which produced too high of a flux were discarded. The flux shown in Fig. 1.5 labeled "Z-Burst (Yos98)" is for a model with a redshift evolution index of 3, a maximum redshift of 3, an extragalactic magnetic field of 10^{-9} G, and a neutrino mass for all three flavors of 1 eV. Another calculation of the neutrino flux from Z-bursts was performed in Kalashev et al. [49], here the parameters were tuned to generate the maximum neutrino flux that is still consistent with gamma and cosmic ray measurements. The resultant neutrino flux, labeled "Z-burst (Kal02)" is shown in Fig. 1.5. This neutrino flux is so large that it has already been rejected at the 90% confidence level by the ANITA-lite experiment [24] and is shown only to illustrate the possible range of fluxes from Z-burst models.

1.3 Microscopic Black Holes

In the standard model, microscopic black holes can be produced in the collision of particles with center of mass energies above the Planck scale of $\sim 10^{19}$ GeV. However, if there are more than the standard four spacetime dimensions, the Planck scale (M_P) can be reduced to values on the order of a TeV [33]. This is

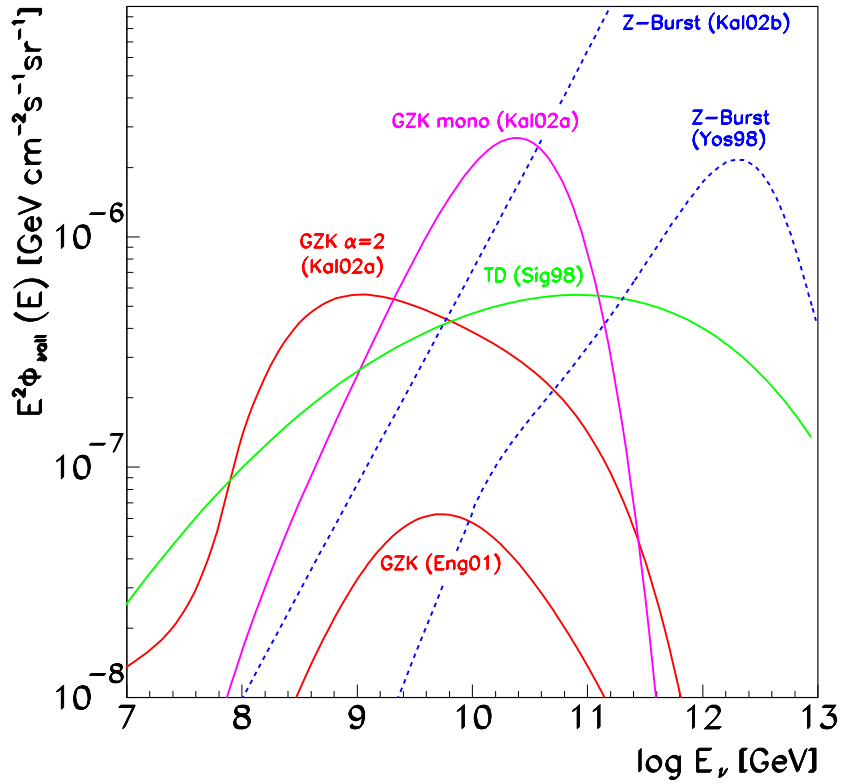

Figure 1.5: All flavor neutrino fluxes for various GZK, top down and Z-burst models. The key is as follows: Kal02a from [50], Eng01 from [31], Sig98 from [70], Kal02b from [49], and Yos98 from [87].

within reach of the highest energy cosmic rays and UHE neutrinos, which can have center of mass energies in excess of 100 TeV. The resulting black holes decay quickly (on the order of 10^{-27} s after formation) into showers of particles, with about 75% of the black hole's energy going into hadronic channels [15]. For neutrino-nucleon interactions, the cross section for creation of microscopic black holes goes as

$$\sigma_{BH} \propto \left(\frac{1}{M_D^2}\right)^{\frac{2+n}{1+n}} \tag{1.9}$$

where M_D is related to the Planck mass by

$$M_D = \left(\frac{(2\pi)^n}{8\pi}\right)^{\frac{1}{n+2}} M_P \tag{1.10}$$

and n is the number of extra dimensions (above four) [18]. Fig. 1.6 shows the cross section for M_D = 1 TeV. There is a wide range of theoretical uncertainties in the minimum black hole mass, so two different minimum black hole masses are shown. The microscopic black hole cross section dominates the standard model cross section at ultra-high energies, and would cause an unexplained excess of events in AMANDA-II.

In Anchordoqui et al. non-detection of neutrinos by numerous experiments has been used to place limits on the cross section of 2.8×10^5 pb [19]. However, these calculations were done using an assumed flux for GZK neutrinos, so enhanced cross sections may still be possible if the GZK flux is smaller than expected.

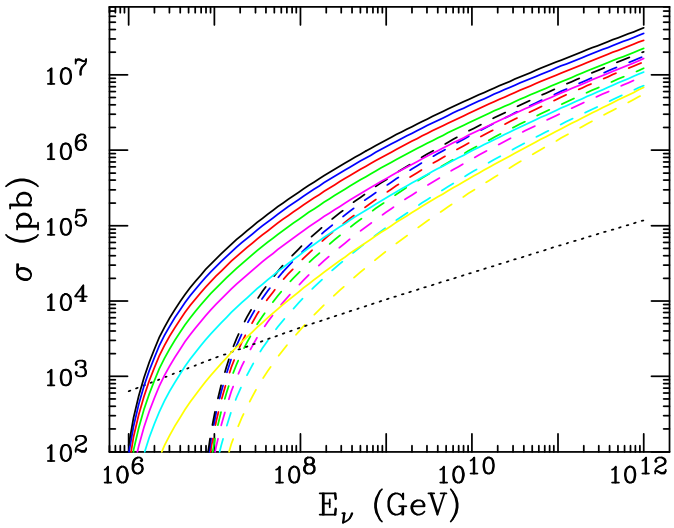

Figure 1.6: Cross section for the production of a microscopic black hole from a neutrino nucleon interaction for n = 1 - 7 extra dimensions (starting from top) and M_D = 1 TeV and $M_{min}{}^{BH} = M_D$ (solid lines) or $M_{min}{}^{BH} = 3M_D$ (dashed lines). The standard model cross section is the dotted line. Figure taken from [18].

1.4 Theoretical Bounds and Experimental Neutrino Flux Limits

1.4.1 Theoretical Bounds

Theoretical bounds have been placed on the flux of neutrinos produced by photo-meson interactions based on the observed cosmic ray spectrum. The crucial assumption is that any mechanism which can accelerate protons to sufficient energies to produce neutrinos will also contribute to the flux of protons in the cosmic ray spectrum with energies in excess of 10^{10} GeV. Any mechanism which is opaque to protons is exempt from this bound. In Waxman & Bahcall [81] a bound on the neutrino flux is derived for mechanisms in which protons are accelerated by Fermi acceleration, giving them a characteristic E^{-2} spectrum. Using the measured energy-dependent generation rate of cosmic rays from Waxman [80] of

$$E_{CR}^2 \frac{d\dot{N}_{CR}}{dE_{CR}} = 10^{44} \text{ erg Mpc}^{-3} \text{ yr}^{-1} \tag{1.11}$$

and assuming the protons lose all of their energy into photo-meson production before escaping the source, a value for the maximum muon neutrino intensity can be derived via

$$I_{max} = 0.25 \xi_Z t_H \frac{c}{4\pi} E_{CR}^2 \frac{d\dot{N}_{CR}}{dE_{CR}} \approx 1.5 \times 10^{-8} \xi_Z \text{ GeV cm}^{-2} \text{ s}^{-1} \text{ sr}^{-1} \tag{1.12}$$

where ξ_Z is a factor which describes the effects of the evolution of neutrino sources as a function of redshift. Estimates of ξ_Z vary from 0.6 for the case of no evolution of neutrino sources (other than co-moving volume) to ~3 for an evolution following the luminosity density evolution measured for quasi-stellar objects [81]. The factor of 0.25 in Eqn. 1.12 is due to the fact that charged pions are

only produced half the time and the resulting neutrino carries away half the pion energy. These factors yield values for this theoretical upper bound (referred to as the Waxman-Bahcall bound) on the E^{-2} flux of muon neutrinos of

$$E^2_{\nu_\mu}\Phi_{\nu_\mu} < 0.9 \; - \; 4.5 \; \times \; 10^{-8}\,\mathrm{GeV\,cm^{-2}\,s^{-1}\,sr^{-1}}. \tag{1.13}$$

This bound was calculated using the assumption of a 1:2:0 ν_e:ν_μ:ν_τ ratio. It can be extended to all three flavors of neutrinos (with a flavor ratio of 1:1:1 ν_e:ν_μ:ν_τ) by multiplying by 1.5:

$$E^2_{\nu}\Phi_{\nu} \; < \; 1.35 \; - \; 6.75 \; \times \; 10^{-8}\,\mathrm{GeV\,cm^{-2}\,s^{-1}\,sr^{-1}}. \tag{1.14}$$

The Waxman-Bahcall bound assumes that accelerated protons escape the source and contribute to the flux of cosmic rays. This bound does not apply to models such as the one described by Stecker et al. [75] (see Section 1.2.1) where the proton photo-meson optical depth is much greater than one ($\tau >> 1$). Most of the AGN jet models mentioned in section 1.2.1 have neutrino fluxes that are in violation of this theoretical limit, including the models from Halzen & Zas [39], Protheroe [69], Mannheim et al. [62] and Mannheim's [61] A model. Although these models are disfavored by this bound, it is still reasonable to search for neutrinos from these model. This bound depends on the assumption that the cosmic ray spectrum goes as E^{-2}, and as shown below, relaxing this assumption can lead to a more permissive bound.

The calculations for the Waxman-Bahcall bound were revisited in Mannheim et al. [62] with a cosmic ray spectrum derived from observations of cosmic rays, rather than the assumed E^{-2} flux used in the original calculation. Because this bound is more general, it is less restrictive than the Waxman-Bahcall bound. However, it has the advantage of being applicable to any model which produces

neutrinos and allows the escape of protons or neutrons from the source, not just those which produce protons with an E^{-2} spectrum. They also give an upper bound on the flux of neutrinos from hidden-core models (those with $\tau >> 1$) by assuming the dominant part of the emitted gamma radiation is in the range measured by the EGRET gamma-ray detector. These theoretical upper bounds, collectively referred to as the MPR bound, as well as the Waxman-Bahcall upper bound, are shown in Fig. 1.7.

1.4.2 Experimental Limits

Fig 1.7 also shows experimental limits for the benchmark E^{-2} neutrino flux in the UHE energy range.

The Radio Ice Cherenkov Experiment (RICE) consists of 19 radio receivers stationed under the ice at the south pole. The receivers were installed in conjunction with the AMANDA-II detector, using the same holes drilled in the ice. RICE searched for radio Cherenkov light from electron neutrino cascades. Using data taken from 1999 - 2005, a 95% confidence level limit was placed on the flux of all three flavors of neutrinos of

$$E^2\Phi_\nu < 10^{-6}\ \text{GeV cm}^{-2}\ \text{s}^{-1}\ \text{sr}^{-1} \tag{1.15}$$

valid over the energy range of 10^8 GeV to 10^{11} GeV [54].

In 2003, a prototype of the balloon-borne Antarctic Impulsive Transient Antenna (ANITA-lite) searched for coherent radio Cherenkov emission from neutrino-induced electromagnetic particle cascades within the Antarctic ice sheet. After flying for 18.4 days with an average lifetime of 40%, ANITA-lite provided an

upper limit to the total flux of all flavors of neutrinos of

$$E^2\Phi_\nu < 1.6 \times 10^{-6}\ \mathrm{GeV\ cm^{-2}\ s^{-1}\ sr^{-1}} \tag{1.16}$$

valid over the energy region of $10^{9.5}$ GeV to $10^{14.5}$ GeV [24]. Observations with the full ANITA detector, which had more antennas and a longer flight time, was completed in December 2006 and are expected to improve this limit by two orders of magnitude [24].

The Baikal Neutrino Telescope is located 1.1 km under the surface of Lake Baikal in Siberia. It consists of 8 strings of 24 optical modules which search for Cherenkov light from charged particles from neutrino secondaries in the water. Using data taken from 1998 - 2003, Baikal limited the diffuse flux of all three flavors of neutrinos to

$$E^2\Phi_\nu < 8.1 \times 10^{-7}\ \mathrm{GeV\ cm^{-2}\ s^{-1}\ sr^{-1}} \tag{1.17}$$

valid over the energy range of 2×10^4 GeV to 5×10^7 GeV [21].

Additionally, a previous analysis using an earlier configuration of the AMANDA detector, consisting of 302 optical modules (see Ch. 2 for a description of the AMANDA detector), has limited the all flavor UHE flux to

$$E^2\Phi_\nu < 9.9 \times 10^{-7}\ \mathrm{GeV\ cm^{-2}\ s^{-1}\ sr^{-1}} \tag{1.18}$$

over the energy range of 10^6 GeV to 3×10^9 GeV [7].

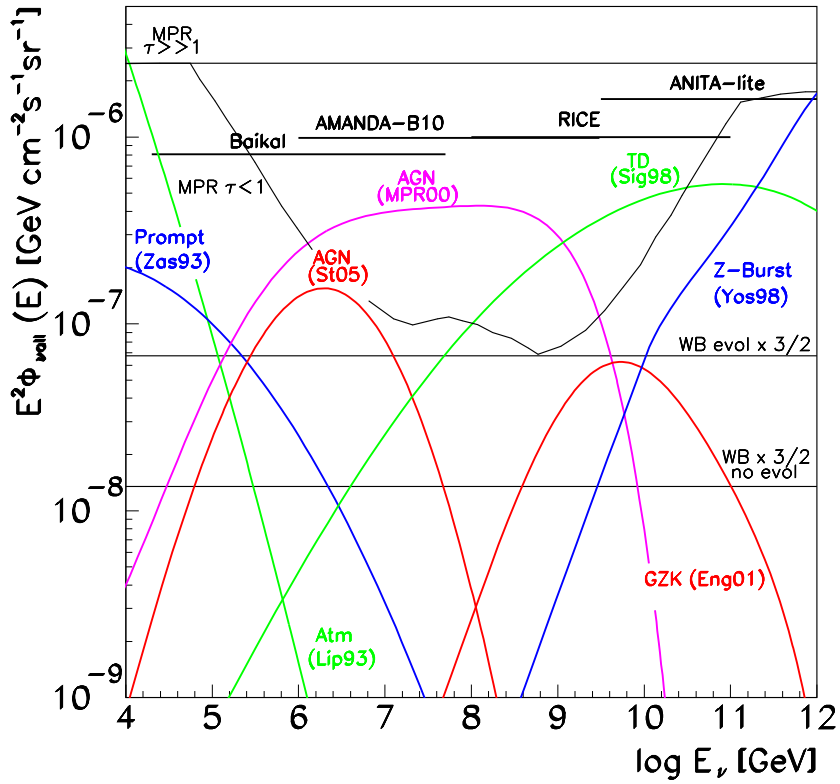

Figure 1.7: Existing all flavor neutrino flux experimental limits and theoretical bounds. Experimental limits shown are from the RICE [54], ANITA-lite [24], Baikal [21] and AMANDA-B10 [7] experiments. Theoretical bounds are WB from [22] and MPR from [62]. Several representative models are shown: St05 from [75], MPR00 from [62], Eng01 from [31], Sig98 from [70], and Yos98 from [87]. Also shown are atmospheric neutrinos (Lip93) from [59] and prompt neutrinos from charm decay (Zas93) [89].

1.5 Atmospheric Neutrinos

Cosmic ray interactions in the atmosphere produce muons and neutrinos. Muons from cosmic ray interactions comprise the primary background for this analysis and are discussed in Chapter 3. Atmospheric neutrinos are produced when a proton (or neutron) interacts and produces a pion or kaon, which then decays into a muon and a muon neutrino. The muon will decay into an electron neutrino. The spectrum of atmospheric neutrinos goes roughly as $E^{-3.7}$, making their

contribution much lower than that of astrophysical neutrino sources at ultra-high energies. In Lipari [59], the flux of atmospheric neutrinos is calculated using Monte Carlo simulations to propagate the cosmic rays through the atmosphere and the resulting flux of muon neutrinos is shown in Fig 1.7 labeled "Atm (Lip93)."

Charmed particles can also be produced in the interaction of cosmic rays in the atmosphere. Semi-leptonic decays of these charmed particles can produce atmospheric neutrinos. The decay occurs quickly, passing on most of the energy to the neutrino, and the resulting neutrinos are referred to as prompt neutrinos. The prompt neutrinos follow the spectrum of the cosmic rays up to energies of $\sim 10^7$ GeV, dominating the conventional atmospheric neutrino flux at high energies [89]. The cross section for charmed particle decay is very poorly constrained by experiment and theoretical predictions at these energies are highly dependent on the assumed quark mass and renormalization scale [89], leading to a large uncertainty in prompt neutrino event rates. In Zas et al. [89], a number of different models for the energy dependence of the charmed cross section were calculated in an attempt to bracket the range of expectations for prompt neutrinos. This analysis uses the "C" parameterization, which uses a fit to experimental measurements for the charmed cross section. This is the highest of the prompt neutrino flux models which have not been eliminated by the lower energy diffuse analysis conducted with four years of AMANDA-II data [5]. The flux for prompt neutrinos is shown in Fig. 1.7, labeled "Prompt (Zas93)."

Atmospheric neutrinos from conventional and charmed cosmic ray secondaries are considered a negligible background for this analysis. They populate a lower energy region and are easily separated from UHE signal events (Fig. 1.8). The event rates for atmospheric and prompt neutrinos at an intermediate and final selection level for the UHE analysis are shown in Table 1.1.

These values have been calculated assuming no neutrino oscillation.

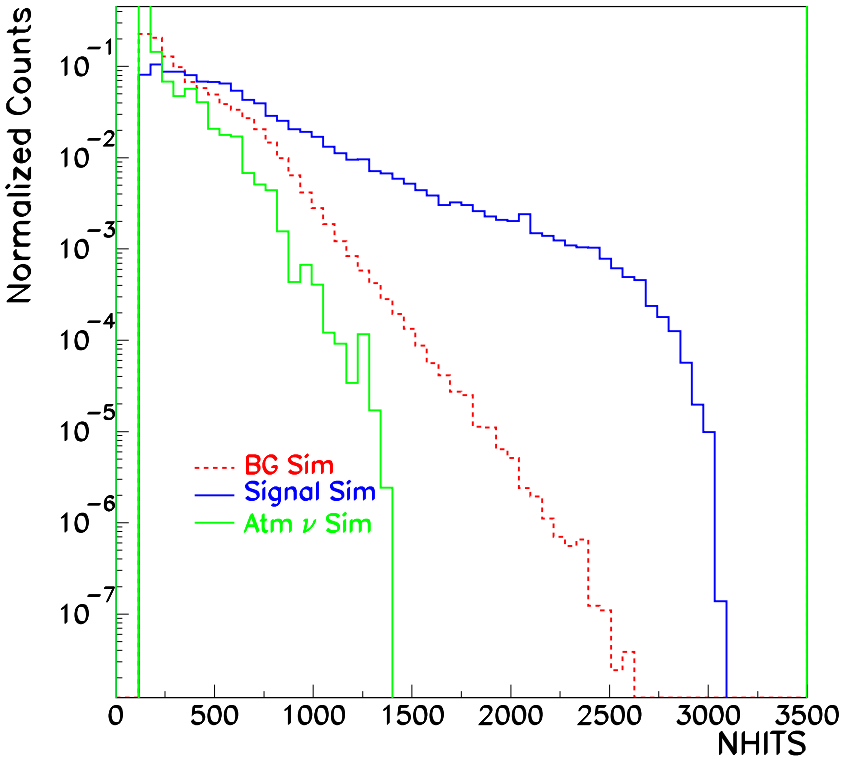

Figure 1.8: The distribution of NHITS for atmospheric neutrinos [59], UHE muon signal (with an E^{-2} spectrum) and muon bundles from cosmic rays. Energy-based distributions, such as NHITS, fall off more quickly for atmospheric neutrinos than muon bundles from cosmic rays, making the bundles the dominant background for this analysis.

1.6 This Analysis

This analysis searched for neutrinos with energies in excess of 10^5 GeV. It uses 677 optical modules (OMs) of the AMANDA-II detector and gives a combined result using three years of data from 2000, 2001 and 2002. A description of the AMANDA-II detector is given in chapter 2. Section 3 discusses the characteristics of astrophysical neutrinos and background, and the simulation of both. The

Table 1.1: Event rates for atmospheric and prompt neutrinos for 456.8 days of livetime at selection level 2 and the final selection level (see Chapter 4 for a full description of selection criteria).

Level	Atmospheric	Prompt
2	9.9	8.8
Final	0.1	0.51

selection criteria used to separate UHE signal from background and the results of this UHE analysis are discussed in section 4. The conclusions and outlook for the future are discussed in section 5.

Chapter 2

The AMANDA-II Detector

2.1 Description

The AMANDA detector consists of 677 optical modules (OMs) deployed below the surface of the ice at the geographic South Pole. The OMs were installed by drilling holes deep into the Antarctic ice with hot water drills. Strings of OMs connected together with cables were then lowered into the water-filled hole. After 4 - 5 days, the water column re-froze with the OMs inside. The OMs are deployed on nineteen vertical strings arranged in a cylinder approximately 200 m in diameter and 500 m long. The OMs are stationed at depths between 1500 m and 2000 m beneath the ice (Fig. 2.1). Each OM contains a Hamamatsu 8-inch photomultiplier tube (PMT) coupled with silicon gel to a spherical glass pressure housing. They are connected to the surface by cables which supply high voltage and carry the signal from the PMT's anode to data acquisition electronics at the surface [84].

The deployment of AMANDA-II occurred in batches during the austral summers in 1995 through 2000, with corresponding improvements in PMT signal transmission technology. The inner four strings were deployed in 1995/1996 and carried the signal to the surface with coaxial cables. OMs on these strings were encased in Billings glass, which lets 85% of the Cherenkov light through compared to the Benthos glass used to encase the rest of the OMs. The next six strings were deployed in 1996/1997 and used twisted pair cables to transmit the signal to the surface. This 10-string configuration of AMANDA is known as AMANDA-B10 and was used for numerous analyses [7, 10, 11, 12]. OMs on these

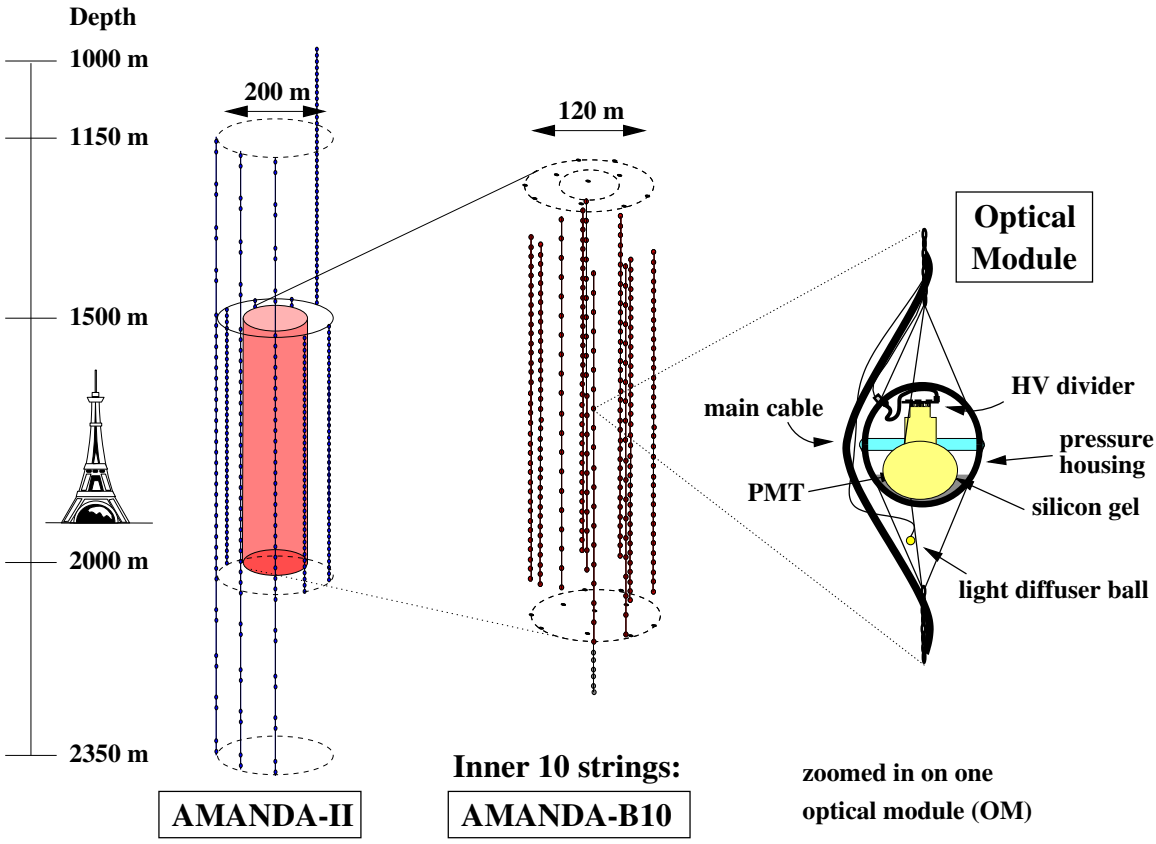

Figure 2.1: The AMANDA-II Detector.

ten strings are operated at a gain of 10^9 in order to transmit the relatively weak 1 photoelectron signals over 2 km of cable [84]. Finally, nine more strings were deployed from 1997 to 2000, bringing the total to 19 strings. This configuration is known as AMANDA-II and is the configuration used in this analysis. PMT signals from the OMs on these nine outer strings are primarily transmitted to the surface via optical fibers, with twisted pair cables installed as a backup. Since the failure rate of the optical connectors and fibers during the high pressures of re-freezing is about 10%, OMs on these nine strings use either optical or twisted pair cables to transmit the pulses to the surface. OMs on strings 14-19 use a transformer to multiply the PMT anode current and are operated at a lower gain of 3 x 10^8. This increases the dynamic range of these OMs compared to the range of the rest of OMs on optical fibers. Signals from OMs with coaxial and twisted

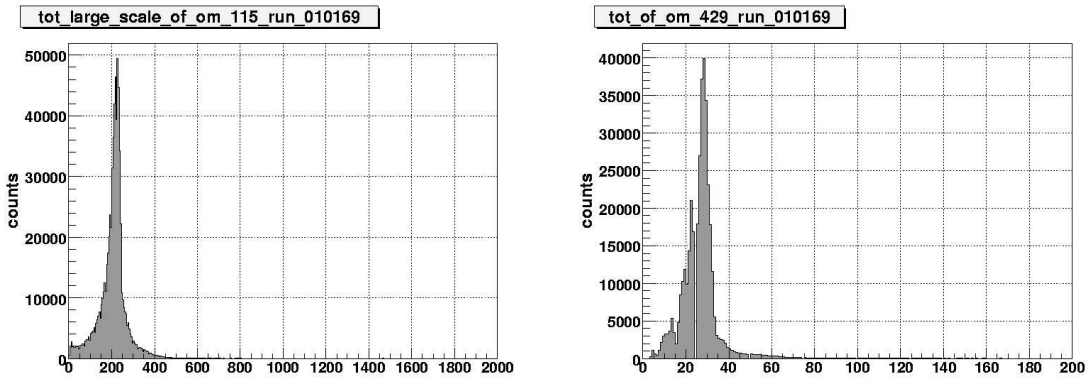

Figure 2.2: Typical pulse width in ns for an OM connected to the surface with an electrical cable (left) and an optical cable (right). Note the differences in scale on the x-axis.

pair (henceforth referred to as electrical) cables are widened by dispersion, leading to a typical pulse width as large as 200 ns, while optical fiber OMs have pulse widths on the order of 20 ns (Fig. 2.2).

There are 87 OMs deployed on strings 1 - 4 with an inter-OM separation of 20 m, 216 OMs on strings 5 - 10 with a separation of 10 m, 122 OMs on strings 11 - 13 with a separation of 20 m, and 252 on strings 14 - 19 with a separation of 12 m. Additionally, on strings 11 - 13, 44 OMs are deployed outside of the main instrumented volume of the detector; 20 of them are deployed between 1150 m and 1500 m beneath the ice and 24 are deployed between 2050 m and 2400 m beneath the ice. Also, during deployment the hole for string 17 froze more quickly than expected, leaving to the string stuck too close to the surface, between 1000 m and 1550 m beneath the ice. These OMs on strings 11 - 13 and string 17 extend into ice that is poorly understood so they are excluded from this analysis.

The AMANDA-II detector uses a majority trigger of 24 OMs hit within a time window of 2.5 μs. Additional triggers are also used, e.g. to capture low energy ($<$ 100 GeV) muons from WIMP interactions, but their descriptions are omitted because they are not relevant to this analysis. At the surface, signals from the OMs are amplified and split into two pulses. One pulse is used to build the trigger and

then fed into the Time to Digital Converter (TDC) which stores a time stamp for the leading and trailing edge of each pulse (a maximum of 16 edges can be stored for each OM, generally this is equal to 8 pulses or "hits", although it is possible for an edge to missed by the electronics). The time resolution of these edges is less than 5 ns despite the dispersion in the cables [84]. The second pulse is delayed by 2 μs and fed into the Analog to Digital Converter (peak ADC) which records the maximum amplitude of all the pulses in that OM. Once the trigger conditions have been satisfied, a signal is sent to the Data Acquisition system (DAQ). After a delay, the DAQ reads out the whole array over a time window of 32 μs.

AMANDA-II has been collecting data since February 2000 with brief breaks only for calibration and hardware maintenance each austral summer. In 2002/2003 transient waveform recorders were installed which record the full pulse shape from each OM [71]. This analysis uses only the years 2000-2002, with analyses for later years utilizing the greater information generated by the transient waveform recorders.

An earlier version of the AMANDA detector called AMANDA-A was deployed in 1993/1994 at depths between 800 m and 1000 m. It was found that residual air bubbles reduced the scattering length to ~10 cm, a value too short to allow reconstruction of the muon track [88]. Because of this, the AMANDA-A detector was abandoned and AMANDA-B10 and AMANDA-II deployments were performed at greater depths where time and pressure have forced the air bubbles out of the ice (see Section 2.4 for more details).

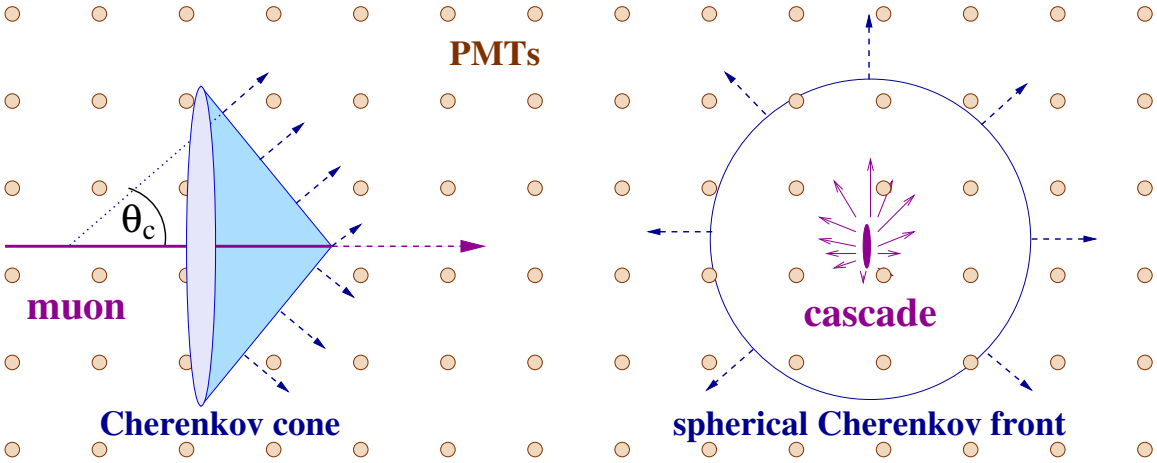

Figure 2.3: Neutrino interactions in the AMANDA-II detector. On the left is a Cherenkov cone from a muon, while the right shows a spherical cascade from an electron or tau. Figure taken from [13].

2.2 Neutrino Detection

AMANDA-II detects neutrinos using the particles produced when a neutrino undergoes a charged current interaction with a nucleon N

$$\nu + N \rightarrow l + X \tag{2.1}$$

and produces a hadronic cascade and an electron, muon or tau. For a muon neutrino, the resulting muon is produced with a mean angle difference of $0.7^\circ \times (E_\nu/\text{TeV})^{-0.7}$ [57], which for UHE energies is well below the angular resolution of the AMANDA-II detector. Muons are identified in AMANDA-II by their Cherenkov light which is given off at a fixed angle

$$\theta_c = arccos(n\beta)^{-1} \tag{2.2}$$

with $\beta \approx 1$ and n=1.33, giving a Cherenkov angle of ~41° relative to the muon track (Fig. 2.3). UHE muons have a range of tens of kilometers [60], which allows detection of muon neutrinos at distances far outside the actual instrumented

volume of AMANDA-II.

Electron neutrinos interact and produce electromagnetic cascades (in addition to the hadronic cascade at the interaction vertex). These cascades are spherical (Fig. 2.3) with slightly larger intensity in the forward direction [13]. Tau neutrinos will produce hadronic cascades and a tau lepton. The tau lepton will travel some distance and decay into a cascade, leading to a "double bang" event signature [58]. However, at the ultra-high energies of this analysis, the tau can travel ~100 m before decaying into a cascade [58], so the UHE tau neutrino event signature for AMANDA-II is likely to be either only a single cascade (either from the neutrino interaction or the subsequent tau decay), a cascade and a tau track or only a tau track.

2.3 Detector Calibration

Every year during the austral summer the detector is calibrated to determine the time delay of signals and the position of the OMs. The calibration is done using bright laser light sources that were either deployed in the ice with the OMs or transmitted down the OM strings.

2.3.1 Time Calibration

Every austral summer the delay time between when a photon hits an OM and the time when that hit is recorded by the DAQ is remeasured. This quantity is known as the T_0 and it is measured for each OM using a 532 nm YAG laser located at the surface. Pulses from the YAG laser are sent via an optical fiber which terminates in a diffusive nylon ball near or inside each OM. Strings 1 - 4 have optical fibers outside of every OM (with the exception of OMs 81 - 86, which have no optical fibers). Strings 5 - 10 have optical fibers near the even numbered OMs. Since the

OM spacing on strings 5 - 10 is half that of strings 1 - 4, the spacing between the fibers is constant for the two sets of strings. Strings 11 - 19 have optical fibers inside each OM.

The total time difference between the laser firing and the recording of the pulse by the DAQ is given by

$$T_0 = t_{le} - t_{pulse} - t_{laser} - t_{otdr} - t_{glass} \tag{2.3}$$

where

t_{le}=measured time of hit from DAQ

t_{pulse}=delay due to rise time of pulse

t_{laser}=time laser pulse enters fiber

t_{otdr}=propagation time of laser pulse in the fiber

t_{glass}=time for light to propagate from diffuser ball to OM

The t_{pulse} time is measured in a separate calibration by sending pulses of varying intensity to the OM. Voltage from multi-photon pulses will rise more quickly than single-photon pulses, so larger peaks will cross the threshold sooner than smaller peaks. The delay time between when a pulse is initiated and when it crosses the threshold goes as

$$t_{pulse} = \alpha \times \frac{1}{\sqrt{ADC}} \tag{2.4}$$

and is determined by a linear fit of leading edge time versus $\sqrt{ADC}$. At low voltages the slope changes rapidly, while at high voltages the PMT saturates. For these reasons, the fit for alpha is typically done between 0.5 and 3 photoelectrons.

The t_{laser} time is measured by splitting the beam of the the YAG laser. One part of the beam is sent down the fiber to the OM. The other part of the beam goes directly to the discriminator and TDC readout. This triggers a delay after which the DAQ begins readout of the array. This delay allows time for the laser pulse to propagate through the surface electronics and down the cable to the OM being measured. This delay depends solely on geometry and changes from OM to OM.

Th t_{otdr} time is measured in a separate calibration run which measures the surface arrival time of the light which is reflected at the end of the fiber. A different wavelength is used which reflects strongly from the end of the fiber for these Optical Time Domain Reflectometer (OTDR) measurements.

The t_{glass} time is calculated using the known speed of light in ice and an estimated distance between the diffuser ball and the OM. Since the distance is very short (~0.3 m), scattering from the ice can be neglected.

Measurements of the T_0's for all OMs were compared to downgoing muon data taken during 2000. The results were found to agree within 0.6% [65].

2.3.2 Geometry Calibration

At the same time that timing calibrations are performed, calibrations to determine the position of each OM are done. Initial position estimates were made during deployment based on a GPS survey of the surface position of the holes, drill logs and spacing of the OMs on each string. However, these initial estimates of depth are not precise enough (primarily due to inaccuracies in the drill logs) and laser measurements are used to supplement these results [85]. Nitrogen UV lasers (337 nm) situated on the bottoms of string 1 and string 5 are used to determine the relative depth of the OMs as well as the distance between strings. These lasers are capable of delivering in excess of 10^{11} photons per blast (see Section 2.5), which allows many OMs to see the light from these blasts and minimizes differences in

leading edge time from scattering in the ice. The relation between the distance to each receiving module and the relative shift in depth is given by

$$D = \sqrt{P^2 + (\Delta z)^2} \tag{2.5}$$

where

P is the perpendicular distance between the emitter and the receiver

Δz is the vertical distance between the receiving OM and the point where P touches the string on which the receiving OM is placed

For strings 14 - 19, two different pressure sensors were deployed with each string, which allowed the cancellation of systematic shifts in depth. Using data from the pressure sensors, the depths of the OMs could be calculated to within 4 m. Using surface GPS surveys and reports of drill drift from the drill logs, the x and y position of each OM could be calculated to with in 1 m [86].

2.3.3 Photoelectron to mV Calibration

A photon which strikes the PMT releases an electron which is accelerated by the dynodes, causing a cascade of electrons. This cascade is measured at the surface in millivolts, with the typical value for 1 photoelectron (pe) varying from OM to OM. During periods of data taking, the most common pulses in an OM will be pulses generated by a single photoelectron. Plotting the ADC value in mV of one OM for many events will show a prominent peak at the single photoelectron value. The pe-mV conversion value is determined by fitting this distribution with a Gaussian and taking the mean.

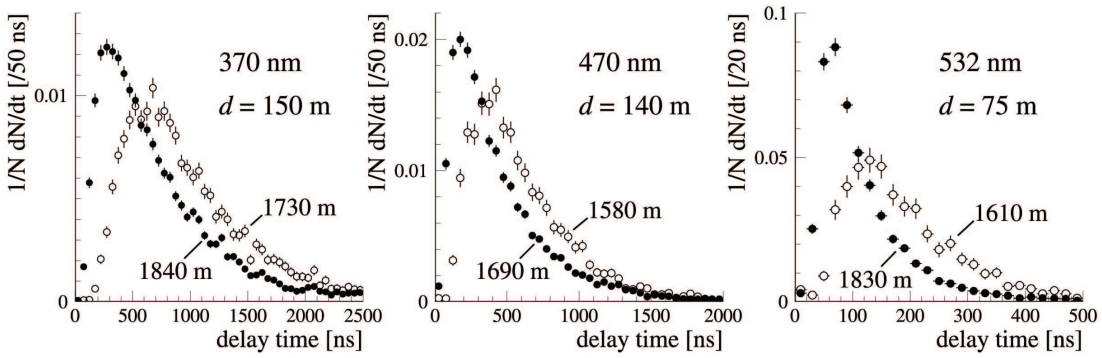

Figure 2.4: Delay time distributions for three different light sources in the AMANDA-II array. The solid circles are from depths where the ice is clear, the hollow circles are from depths where the ice is dustier, resulting in more scattering and longer delay times. Figure taken from [8].

2.4 Ice Properties

As light travels from a muon or cascade to an OM, it will be both scattered and absorbed by the ice. The intrinsic molecular properties of the ice, as well as the amount of impurities, determine the scattering and absorption lengths (λ_s and λ_a respectively). These values can effect both the number of photons and the delay in arrival times at an OM (Fig. 2.4), so accurate measurements of λ_a and λ_s are necessary to understand events in AMANDA-II. In the Antarctic ice it is not possible to separate measurements of λ_s from measurements of the average scattering angle $<cos\theta>$, so instead an effective scattering length is measured, defined as

$$\lambda_e = \frac{\lambda_s}{1 - < cos\theta >}. \tag{2.6}$$

The ice properties have been measured as a function of wavelength and depth using in-situ laser light sources [8]. The absorption and effective scattering lengths are determined by comparing the measured delay times to Monte Carlo simulations done with a range of different absorption and effective scattering lengths. Figure 2.5 shows the effective scattering coefficient ($b_e = \frac{1}{\lambda_e}$) as a function

of depth and wavelength. At lower depths, b_e is dominated by bubbles in the ice. As the depth increases, the pressure increases, and at ~1500 m, these bubbles undergo a phase change to solid air-hydrate clathrates, which has an index of refraction very close to that of ice [8]. Below this depth air bubbles no longer effect light traveling through the ice and dust becomes the dominant factor. The peaks labeled A - D correspond to layers of ice which are very dusty (and also to periods of geologic time where temperatures were unusually cool). Light which passes through these layers is scattered or absorbed at a much higher rate than clear ice.

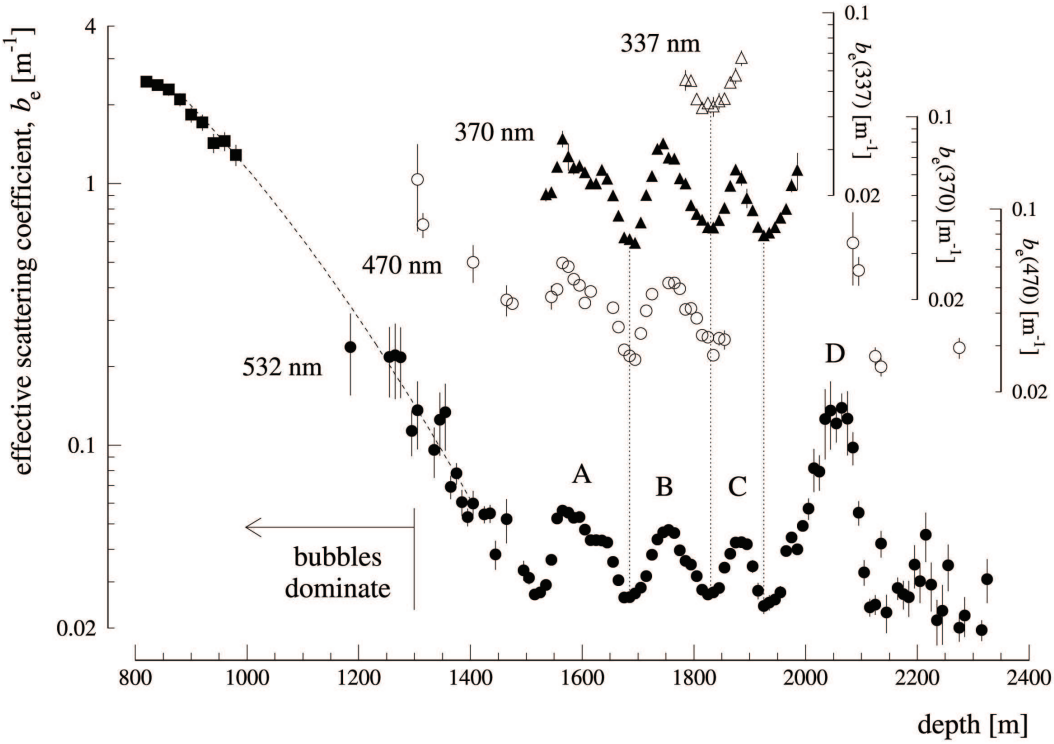

Figure 2.5: The effective scattering coefficient measured with laser sources at four wavelengths as a function of depth. Data at 337, 370, and 470 nm are scaled according to the axes to the right. The four peaks labeled A through D correspond to stadials in the last glacial period. Figure taken from [8].

Scattering lengths range between 14 to 28 m and absorption lengths range between 60 to 120 m in the ice at AMANDA-II depths. These values are included in the simulation using the PTD software package [51], which generates large

tables of photon intensities and delay times. Crude layering is introduced by using PTD tables generated with different absorption and effective scattering lengths at different depths. This analysis uses the MAM ice model, which has an average scattering length of 21 m and an average absorption length of 94 m. The MAM ice model is based on an iterative adjustment of the measured ice properties to obtain better agreement between time-residuals of well reconstructed simulated muon tracks and experimental data [44]. Photonics, a more complete simulation package which can implement the measured ice properties with any desired resolution as well as incorporate the wavelength dependence of absorption and scattering lengths, is under development and was not used for this analysis.

2.5 UHE Calibration

Atmospheric neutrinos and cosmic ray muons are a calibration source for the AMANDA-II detector [20]. Simulations of these two types of events can be compared to experimental data to verify that the understanding of the detector is correct. However, these calibration sources are only useful for lower energies. The flux of atmospheric neutrinos falls as $E^{-3.7}$, with less than a handful of events per year expected with energies above 10^5 GeV, too few to verify the detector response at high energies. Although the flux of cosmic ray muons falls off less sharply (as $E^{-2.7}$), the large uncertainties in cosmic ray flux above 10^6 GeV (see Section 4.8 for a description of these uncertainties) make it very difficult to discern the source of any disagreements between detector simulations and experimental data. This analysis searches for signals with energies as high as 10^{12} GeV, where the detector response is virtually unverified. Are there saturation effects that are only important at the highest energies? Is the detector response at these high energies sufficiently well modeled by simulations based on lower energy events?

Table 2.1: The attenuation factors for each step of light from LM2. FR stands for Fresnel Reflection.

Billings Glass	FR (Billings)	UG-11	FR (UG-11)	Teflon	Age	Total
0.00967	0.95	0.84	0.91	0.25	0.59	0.00104

The AMANDA-II detector has a number of in-situ laser devices which can be used to answer these questions. UHE calibration efforts focused on a nitrogen laser deployed on the bottom of string 5 between OMs 121 and 122 at a depth of ~2750 m. The 337 nm nitrogen laser (named LM2) was chosen because it is situated near the center of the array and generates events with the highest number of hit OMs (NCH) compared to other in-situ laser devices (Fig. 2.6). LM2 is a VSL-337i OEM nitrogen laser from Laser Science, Inc. purchased in June 1997. It can generate pulses with a maximum energy of 200 μJ. Technicians from Laser Science Inc. estimate that the pulse energy will decrease by a factor of 0.7 every two years. LM2 is encased in a glass sphere made of Billings glass. Light from LM2 passes through an attenuator, then the Billings glass sphere, then a UG-11 filter from Schott glass (to filter out any fluorescence from the laser light passing through the sphere), and finally a teflon diffuser from Oriel which gives the light a modified $\cos(\theta)$ distribution. Each step reduces the intensity of the laser light, with the dominant factor coming from the Billings glass, which only allows 0.967% of the light through at 337 nm [78]. Table 2.1 shows the reduction in light intensity for each step for data taken in 2000. Applying all of these factors leaves a maximum energy in the ice of 0.207 μJ or 3.5×10^{11} photons.

LM2 data was taken in the austral summer between 2000 and 2001. Because there was no way to trigger the DAQ each time the laser fires, data taking was triggered by a hit in OM 121, the OM just above the laser. The strength of the laser pulse can be adjusted by moving an attenuation wheel, which attenuates the laser pulse by a factor of $10^{3.5}$, 10^{3}, $10^{2.5}$, 10^{2}, $10^{1.5}$, 10^{1}, $10^{1.5}$, 10^{1}, $10^{0.5}$, and 1 (i.e. no

attenuation). Data was taken at each of these attenuations and compared with simulations of laser blasts at the same position.

Before data could be compared with simulation, it had to be cleaned. First a minimum NCH cut is necessary to remove cosmic ray muon events which happen to include OM 121, as well as events generated when the laser misfired (firing before its highest intensity could be reached). For laser runs without attenuation, the laser events are clearly separated (Fig. 2.7), but at the highest attenuations these events start to overlap (Fig. 2.8) and it is estimated that 40% of the events in the highest attenuation sample are due to misfirings after applying the NCH cut. Since the number of hit OMs will decrease as the attenuation of the laser blast increases, separate NCH cuts were applied for each attenuation (Fig. 2.9). LM2 is very powerful, even after the intensity of the laser light is reduced by a factor of $10^{3.5}$, it still fills about one-fifth of AMANDA-II.

Next, OMs which are malfunctioning must be removed. Because the LM2 data was taken in between data taking periods, the electronics were in a state of constant flux. For example, a concerted effort was made to revive OMs which had not functioned during the year 2000. This effort was ongoing during the laser runs, so the dead OMs during these runs were not the same as those that were dead during either 2000 or 2001. Instead dead OMs were defined as OMs which had no hits in 1000 laser events. Also, on strings 1 - 10, it is common for a hit in one OM to induce small signals in the cables of other OMs at the surface. This phenomenon is known as cross-talk and is usually removed from the data by requiring that the TOT of a each pulse be greater than a certain threshold (125 ns for 2000). There are some OMs in which a large fraction of the hits are caused by cross-talk (which are typically removed during data taking runs). For the laser runs, OMs in which more than 35% of their first hits were found in the cross-talk region (i.e. with TOTs < 125 ns) were removed. Additionally, OMs with more

than 10% of their hits missing both leading edge and TOT information were removed. Finally, OMs on strings 5 and 6 (the next closest string to 5) were removed because light which struck these OMs included effects that aren't included in the simulation, such as shadowing of the OMs on string 5 (since the light source is located directly on string 5, OMs between the receiving OM and the laser could block light that would reach these OMs in simulation). After these OMs were removed, the remaining hits were cleaned by requiring that they have a sufficiently large TOT and are not isolated in time or space. The same cleaning for OMs and hits was applied to both experimental and simulation events.

After cleaning, the number of photons was determined by matching the mean of the NCH distributions for simulation and experimental datasets at each attenuation. Fig 2.10 shows the number of photons as a function of LM2 attenuation as well as the best fit line for these points. The best fit for these points has a slope of -0.81, which is within 20% of the expected value of -1.0. Also, the absolute normalization is within a factor of 5 of the values calculated above for number of photons with no attenuation.

Comparisons were also made between simulation and experiment for a number of variables used in the UHE analysis which are correlated with energy (for a full description of these variables see Chapter 4). The fraction of OMs with one hit is shown in Fig. 2.11 for five different laser attenuations. The simulation shows good agreement in shape with the laser events over a wide range of attenuations and agreement within 15% of the mean values of the distributions. A similar agreement can be seen for the fraction of OMs on electrical cables with one hit (Fig. 2.12), although here the means agree to within 20%. The total number of hits in the array shows agreement of the means to within 20%, but the shapes are in disagreement (Fig. 2.13). The widths of the peaks are much thinner for simulation than for actual data. This could have two possible explanations. The

first is fluctuations in laser intensity on the order of 20%. The laser has been seen to fire at a lower intensity during some of the runs with a higher attenuation (Fig. 2.8). By varying the intensity of photons in the simulation, the width of the NHITS distribution can be explained if we allow the number of photons to shift by 20% in either direction. The NCH distribution is relatively insensitive to this fluctuation but, as can be seen in Fig. 2.14, the resulting NHITS widths are in good agreement. A second possible explanation is inadequate modeling of ice layers. As mentioned in Section 2.4, layers of dust in the ice can effect the number of photons. Figure 2.15 shows the percentage disagreement between the number of hits in an OM for laser data and simulations versus depth. The OMs with the greatest disagreement lie at depths below 1980 m, which is roughly the beginning of the dusty ice layer labeled "D" shown in Fig. 2.5, indicating that the ice around these OMs may not be properly modeled in the simulation.

Simulations of the nitrogen laser events show good agreement with experiment. This demonstrates that the behavior of the AMANDA-II detector is well understood in the ultra-high energy region. Despite minor disagreements in some variables, these calibrations demonstrate that the gross behavior of the detector at ultra-high energies is sufficiently understood.

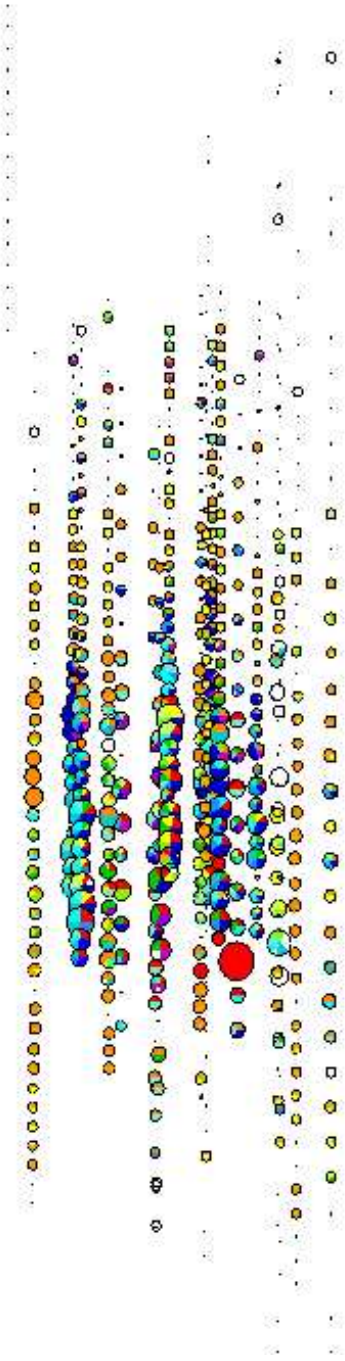

Figure 2.6: Schematic view of a LM2 event without attenuation. Colored circles represent hit OMs (black dots are OMs that are not hit). The color of the circle indicates the hit time (red is earliest), with multiple colors indicating multiple hits in that OM. The size of the circle is correlated with the number of photoelectrons produced.

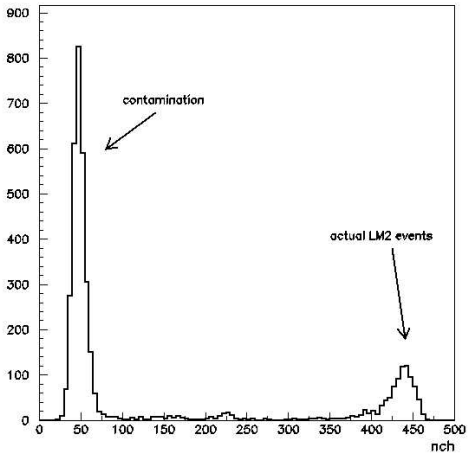

Figure 2.7: The number of hit OMs during firing of LM2 without attenuation. The peak at low NCH is due to events from cosmic ray muons and the peak at ~225 is from laser misfirings. The smaller peak at ~430 are events from LM2 with no attenuation.

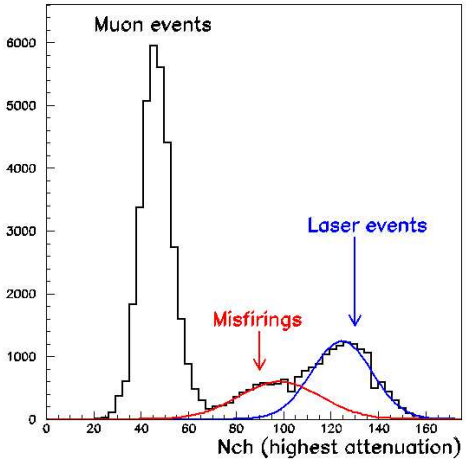

Figure 2.8: The number of hit OMs during firing of LM2 with an attenuation of 3.5. The peak at low NCH is due to events from cosmic ray muons. The peak at ~90 is due to laser misfiring and the peak at ~130 are events from LM2.

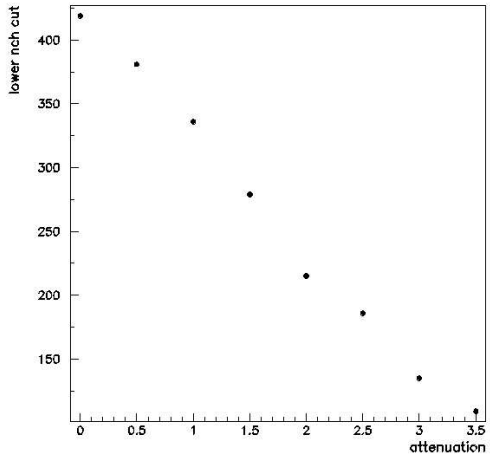

Figure 2.9: The minimum number of hit OMs required versus LM2 attenuation.

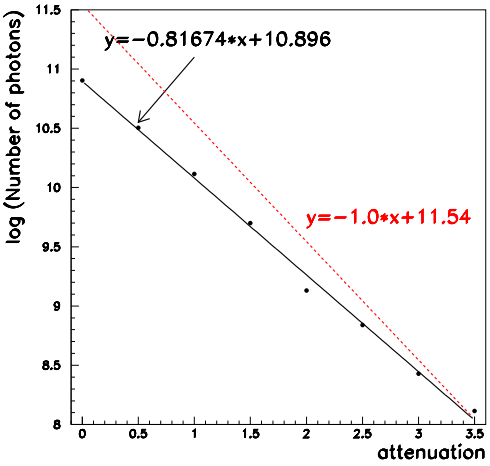

Figure 2.10: The logarithm of the best fit (black solid line) for simulated number of photons versus LM2 attenuation. Also shown is a line with the slope expected for attenuation steps of $\sqrt{10}$ (red dashed line).

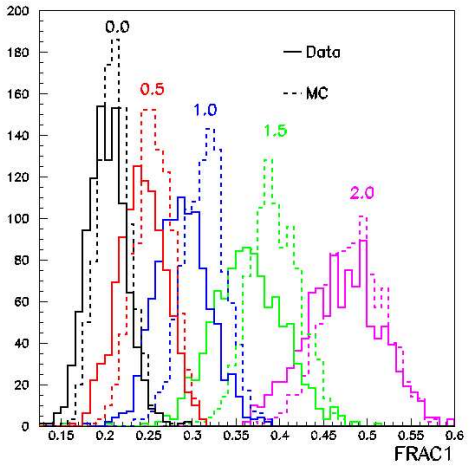

Figure 2.11: The distribution of the fraction of OMs with one hit for simulation and experimental LM2 runs at different attenuations.

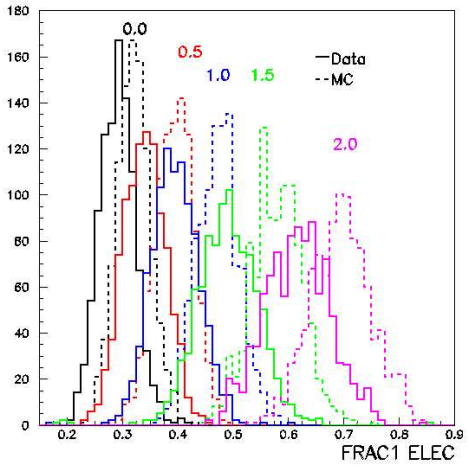

Figure 2.12: The distribution of the fraction of OMs on electrical cables with one hit for simulation and experimental LM2 runs at different attenuations.

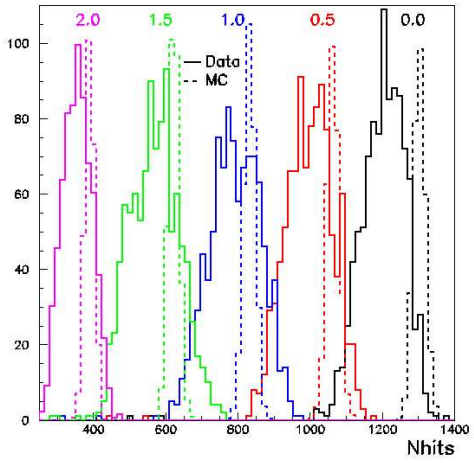

Figure 2.13: The distribution of the total number of hits for simulation and experimental LM2 runs at different attenuations.

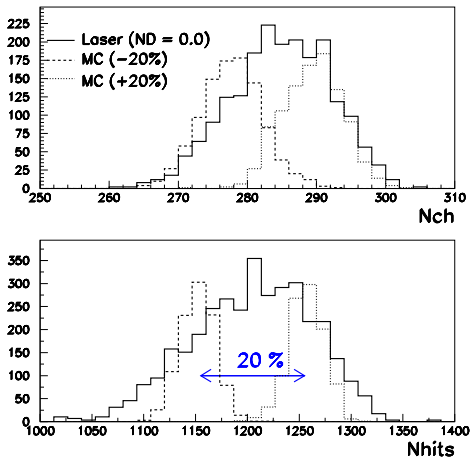

Figure 2.14: The NCH (top) and NHITS (bottom) distributions for simulation and experimental LM2 runs without attenuation. The simulation is varied by 20% around the value which shows the best agreement in NCH

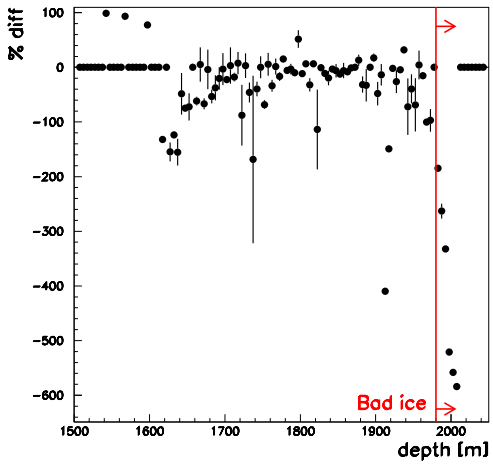

Figure 2.15: The percentage disagreement between simulation and experimental data in NHITS versus depth.

Chapter 3

Experimental and Simulated Datasets

3.1 Background Characteristics and Simulation

The primary background for the UHE analysis consists of bundles of muons from cosmic ray interactions in the atmosphere. Because the UHE search is conducted in the down-going direction, the Earth cannot be used to screen out muons from cosmic rays as in other AMANDA analyses [6, 10, 12]. The high energy threshold of this analysis removes AMANDA events triggered by lower energy cosmic rays, leaving events with bundles of 100s-10000s of muons from higher-energy cosmic rays as the background for the UHE analysis (Fig. 3.1). These muons are coplanar and can spread over cross-sectional areas as large as 200 m^2. The highest energy events can deposit energies as high as 4×10^5 GeV in the ice.

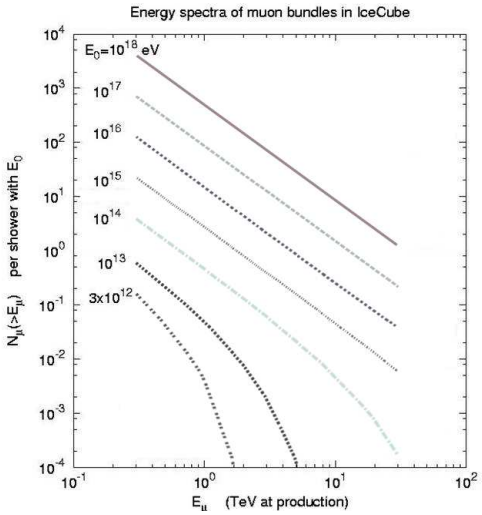

Figure 3.1: The number of muons with energies greater than E_μ for various cosmic ray primary energies. Figure drawn by T. Gaisser.

The simulated background muon bundles from cosmic rays are generated

using the CORSIKA simulation program with the QGSJET hadronic interaction model [41]. CORSIKA propagates cosmic rays from the top of the atmosphere to the Earth's surface. At early levels of this analysis, cosmic ray primaries are generated with composition and spectral indices from Wiebel-Sooth et al. [83], with energies of the primary particles ranging between 8×10^2 GeV and 10^{11} GeV. Generation of cosmic ray primaries is extremely computationally intensive and makes up the bulk of computer simulation time for this analysis. Since the energy spectrum of cosmic rays falls as $E^{-2.7}$, the majority of events which are produced with full-spectrum particle simulation are low energy events which are cut away at the earliest levels. As shown in Fig. 3.2, at trigger level (level 0) the majority of simulated cosmic ray events have energies less than 10^6 GeV. After the level 2 selection criteria have been applied, the average energy is 4.6×10^6 GeV.

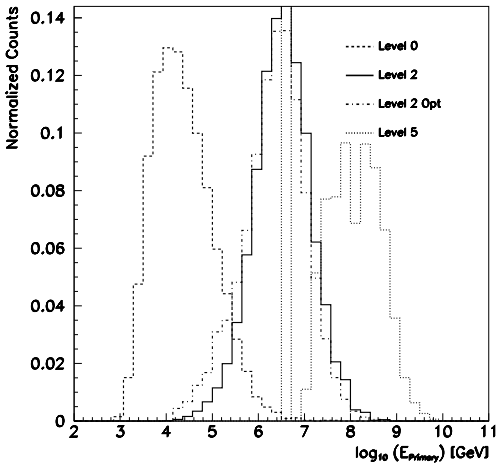

Figure 3.2: The energy of the simulated cosmic ray primaries as a function of selection level. "Level 2 Opt" and "Level 5" are simulated with an optimized spectrum, the rest are simulated with full spectrum simulations described in the text.

In order to reduce simulation time, and optimized simulation is used for selection level 2 and beyond. It was shown in Glasstetter et al. [37] that the flux of all cosmic rays primaries can be approximated by the sum of proton and iron

primaries. Fig. 3.3 shows the cosmic ray flux measured by the KASCADE collaboration along with reweighted iron and proton curves. The spectral slope of the proton flux is -2.67 until 4.1×10^6 GeV, where it steepens to -3.39; the spectral slope of the iron flux is -2.69 until 10^8 GeV, where is steepens to -3.1. The sum of the proton and iron curves are a good approximation of the full cosmic ray flux. Using this approximation reduces computation time for background simulation

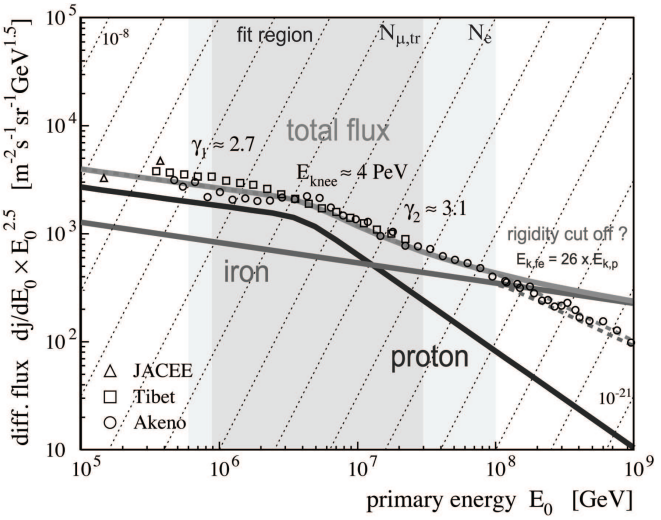

Figure 3.3: The two-component model for cosmic ray flux. Figure taken from [37].

by allowing generation of only two particles types with an optimal spectra. In order to minimize statistical uncertainty at the highest energies, proton and iron primaries are generated with an E^{-2} spectra. Additionally, the lower energy threshold is raised to 8×10^4 GeV. These primaries are then reweighted to the spectrum of the cosmic ray flux shown in Fig. 3.3. The formula used to reweight the optimized spectra to the one given in Glasstetter et al. [37] was adapted from Hill [43] and is given by

$$weight = \frac{C \times A_{gen} \times \Omega \times T \times \int_{E_{low}}^{E_{high}} E^{-2}\, dE \;\times E^{-\Delta\gamma}}{N} \tag{3.1}$$

where C is taken from Fig. 3.3, $\Delta\gamma = 0.67$ for protons and 0.69 for iron, A_{gen} is the

generation area, Ω is the solid angle of generation, T is the time period, E_{low} and E_{high} are the lower and upper energy bounds of the simulation, respectively, and N is the number of primaries generated.

Fig. 3.2 shows cosmic ray energy spectrum for full-spectrum and optimized simulation samples at selection level 2 (labeled "Level 2" and "Level 2 Opt," respectively). These two samples show good agreement in spectra and demonstrate the feasibility of using an optimal simulation set. They also demonstrate that optimized simulation sets can only be used at later levels of the UHE analysis, as earlier levels will be dominated by low energy primaries.

For simulations using 2000 geometry (here geometry refers to pe/mV and T0 values for each OM as well as removing non-functioning OMs), only full-spectrum and optimized background simulations were used. For 2001/2002, full-spectrum background simulation was not generated, but the energy threshold of the optimized simulation was lowered to 10^4 GeV and a third set of optimized simulation was added with the lower energy threshold raised to 10^6 GeV in an attempt to decrease the statistical uncertainty at later cut levels. A subset of proton and iron primaries that were generated for 2001 were reprocessed with 2002 geometry to further decrease the statistical uncertainty. The numbers of proton and iron primaries generated for the various sets of simulations are listed in Table 3.1.

After the cosmic ray primaries are generated, the resulting muons are propagated through the ice above the AMANDA detector using the Muon Monte Carlo (MMC) simulation package [28]. MMC tracks energy loss due to ionization losses, bremsstrahlung, photo-nuclear interactions and e^+/e^- pair production as the muons travel through the ice. Although most of these energy losses are stochastic in nature, for simplicity of simulation, energy losses along the muon track are only written to the output file when the loss exceeds $0.05 \times E_{muon}$.

Table 3.1: Number of proton and iron primaries generated for each simulated background dataset per year. Rows marked with "R 2001" are 2001 files reprocessed with 2002 geometry.

Year	Type	Proton	Iron
2000	Full-Spectrum	78.7 days	78.7 days
	E_{thres}=8×10^4 GeV	6.82×10^7	9.93×10^7
2001	E_{thres}=10^4 GeV	2.476×10^8	6.023×10^8
	E_{thres}=10^6 GeV	2.4710×10^7	2.1469×10^7
2002	E_{thres}=10^4 GeV	1.904×10^8	3.592×10^8
	E_{thres}=10^4 GeV (R 2001)	1.431×10^8	2.927×10^8
	E_{thres}=10^6 GeV (R 2001)	3.4×10^6	6.899×10^6

The detector response is simulated using the AMASIM2 simulation package [46]. To reduce simulation time, large, pregenerated tables of photon intensities and time delays relative to each OM have been made using the PTD software package [51]. Optical properties of the ice are included in the creation of these tables. The UHE analysis uses the MAM ice model, which is based on an iterative adjustment of ice properties to obtain better agreement between time-residuals of well reconstructed simulated muon tracks and experimental data [44]. A number of different MAM ice tables have been generated, each with a different absorption and scattering length to approximate the fluctuations in ice clarity measured in the Antarctic ice (see Section 2.4 for more details) and are collectively referred to as the layered MAM ice model. For each energy deposit from each muon track, AMASIM obtains the number and timing distribution of photoelectrons generated in every OM from the PTD tables. Each photoelectron induces a pulse in the OM with a characteristic pulse shape (the simulation includes 9 different pulse shapes; OMs are classified according to deployment and type of cable connection to the surface). These pulses are summed over all energy deposits and all tracks for all OMs. As described in Chapter 2, if a majority trigger of 24 hit OMs in a window of 25 μs is satisfied, then output from the OMs is written out in the same format as experimental data.

Table 3.2: Relative uncertainty of background simulation and experimental data at selection level 4 for each year. The uncertainty on the data is $\sqrt{N_{events}}$.

Year	Experiment	BG Sim
2000	0.18	0.38
2001	0.12	0.20
2002	0.14	0.36

3.1.1 Estimating Background Simulation Livetime

Generation of background simulation is very computationally demanding. The ideal standard in most analyses is to generate at least twice as much simulated livetime as experimental livetime, but that was not possible for the UHE analysis. It takes on average about 0.03 (0.02) seconds to generate and fully process one iron (proton) primary. This gives a total generation time of ~830 (~570) days for the iron (proton) simulation generated with 2001 geometry. Table 3.2 shows the relative uncertainty of simulation and experimental data for 2000, 2001 and 2002 at selection level 4 of the UHE analysis. Despite heroic simulation efforts, the relative uncertainty of the simulation is still greater than the experiment, indicating that the generation livetime of the simulation is less than the livetime of the experiment.

3.2 Signal Characteristics and Simulation

Signal for the UHE analysis consists of leptons and cascades from electron, muon and tau neutrinos. The neutrino interaction length decreases with energy (Fig. 3.4) and becomes less than the diameter of the Earth above 10^6 GeV [36]. Thus, Earth absorption limits the direction of UHE neutrinos to the horizon and southern hemisphere. In order to be detected in the AMANDA-II detector, the neutrino must interact within a few hundred meters of the instrumented volume. Neutrinos coming from a vertical downgoing direction have only the limited

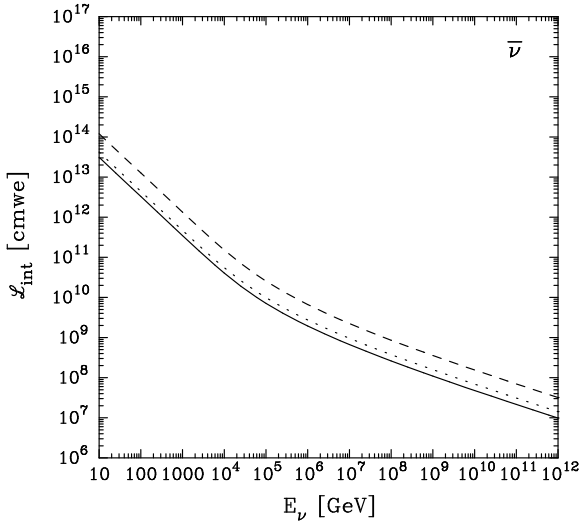

Figure 3.4: The anti-neutrino charged-current (dashed line), neutral-current (dotted line) and total (solid line) interaction length as a function of energy. Figure taken from [36].

overburden of 1.5 km of ice in which to interact. This limits the number of triggered neutrino events from the vertical, down-going direction, leaving the neutrino signal concentrated around the horizon (Fig. 3.5).

Simulated UHE neutrino signal events are generated using the All Neutrino Interaction Simulation (ANIS) package [53]. ANIS is a Monte Carlo event generator for neutrinos of all flavors. It begins by throwing neutrinos randomly on the surface of the Earth and then propagating the neutrinos through the Earth accounting for all relevant interaction and decay processes. The tau decay is simulated using the TAUOLA simulation package [48]. At the energies of interest in this analysis, the interaction cross sections for neutrinos and anti-neutrinos are nearly identical (Fig. 1.2) and only neutrinos with energies between 10^3 GeV and 10^{12} GeV are generated with an E^{-1} spectrum. To reduce statistical uncertainty, additional signal events were generated for the energy ranges of 10^3 GeV to 10^6 GeV. For electron neutrinos additional signal events were also generated between the energies of 1.5×10^6 GeV and 10^7 GeV. Signal files were generated until the statistical uncertainties on the signal at the final cut level were on the order of 5%

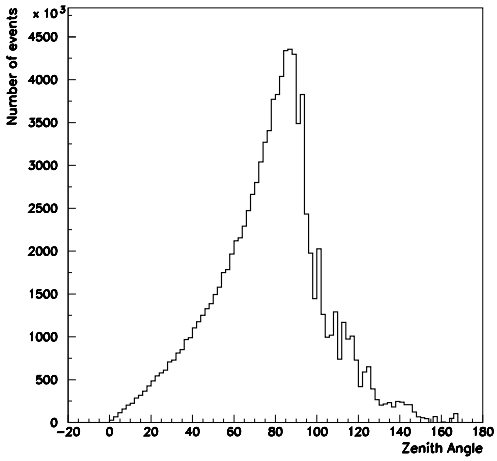

Figure 3.5: The true zenith angle of E^{-2} muon neutrino signal at selection level 2 of the UHE analysis. Vertical events have a zenith angle of 0°, while horizontal events have a zenith angle of 90°

(see Table 3.3 for exact numbers).

Leptons produced by the simulated neutrinos are propagated through the rock and ice close to the detector with MMC. Since these neutrinos could come from any direction, it is important that rock by included in the propagation of the neutrinos. This is done using a three layer model, first a less dense ice layer (density of 0.756 g/cm^3) that ends 200 meters below the surface, then an ice layer with a density of 0.917 g/cm^3 and finally a rock layer (density 2.65 g/cm^3) starting 2800 meters below the surface of the ice. Otherwise, all simulation parameters are the same as the background simulation described previously.

The detector simulation parameters used in AMASIM are also very similar to those used for simulation of background with the exception of the PTD ice tables. Background simulation uses layered MAM PTD tables, with a number of different tables with different ice properties as a function of depth. During simulation, if a light deposit occurs at the depth of a particular table, it is assumed that all OMs struck by that light will lie in ice with the same characteristics. This is generally a reasonable assumption for the lower energy processes associated with

Table 3.3: Number of electron, muon and tau neutrinos simulated per year and their statistical uncertainties at the final selection level of the UHE analysis.

Year	Flavor	10^3 GeV - 10^6 GeV	1.5×10^6 GeV - 10^7 GeV	10^3- GeV 10^{12} GeV	Statistical Error
2000	ν_e	-	-	3.295×10^7	5.7%
	ν_μ	3.554×10^7	-	2.610×10^7	4.7%
	ν_τ	1.208×10^7	-	0.836×10^7	7.2%
2001	ν_e	1.338×10^7	2.029×10^7	2.541×10^7	4.2%
	ν_μ	4.573×10^7	-	1.441×10^7	4.5%
	ν_τ	2.221×10^7	-	0.960×10^7	5.9%
2002	ν_e	2.069×10^7	2.057×10^7	2.527×10^7	3.1%
	ν_μ	2.504×10^7	-	0.943×10^7	5.2%
	ν_τ	2.790×10^7	-	1.142×10^7	5.5%

background simulation. However, for signal, the energy of the photons can be orders of magnitude higher, so it's reasonable that photons from UHE neutrinos can pass through many different ice layers before striking an OM. For this reason, one PTD ice table (called a bulk MAM table) is used with absorption and scattering parameters equal to the average values used in the layered MAM tables.

3.3 Experimental Data

Data used in this analysis was recorded in the time period between February 2000 and November 2002, with breaks each austral summer for detector maintenance, engineering, and calibration lasting approximately four months. In addition to maintenance downtime, the detector also has a brief period while recording each event in which it cannot record new events. Data-taking periods ("runs") with anomalous characteristics (such as excessive trigger rates or large numbers of OMs not functioning) are discarded. These factors combine to give a deadtime of 17% of the total data taking time for 2000, 22% of the total data-taking time for 2001, and 15% of the total data taking time for 2002. Additionally, 26 days are excluded from 2000 because the UHE filtered events are polluted with high

number of events with incomplete hit information, likely due to a minor detector malfunction (Fig. 3.6). Since the cause of this absence is unknown, to ensure data quality events from these days were not included in the UHE analysis. Taking

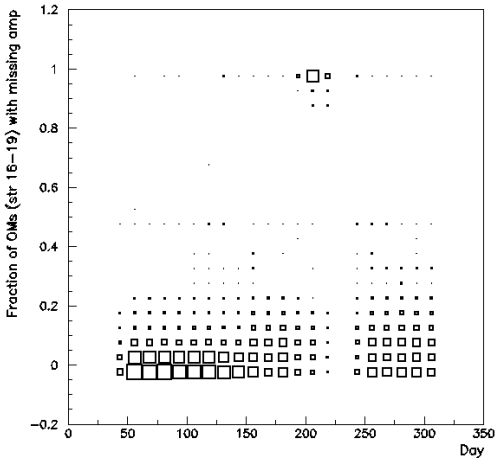

Figure 3.6: Fraction of events missing amplitude information on strings 16 - 19 versus day of the year. Days 199 - 228 are excluded because of this irregular detector behavior.

these factors into account, there are 173.5 days of livetime in 2000, 192.5 days of livetime in 2001 and 205.0 days of livetime in 2002. Finally, 20% of the data from each year is set aside for comparison with simulations and to aid in the choice of selection criteria, leading to a total livetime for the three years of 456.8 days.

In the data-taking period studied in this analysis (456.8 days), AMANDA-II recorded 1.3×10^9 events in 2000, 2.0×10^9 events in 2001, and 1.9×10^9 events in 2002 at trigger.

Chapter 4

UHE Analysis

4.1 Strategy

This analysis uses a few general strategies to distinguish UHE neutrinos from cosmic ray muon bundles. First, UHE neutrinos are more energetic than the background of bundles of muons from cosmic rays. Observables that are correlated with energy are used to reject lower energy background events. Second, background muon bundles come primarily from the downgoing direction, while UHE neutrinos are clustered around the horizon, so selecting on the reconstructed direction of events helps remove background events. Finally, observables which emphasize large localized energy deposits are used to distinguish signal from background.

This analysis exploits the differences in light deposition from bundles of many low energy muons and single UHE muons or cascades from UHE neutrinos. A muon bundle with the same total energy as a UHE neutrino spreads its light over a larger volume, leading to a lower light density in the array. Variables which are correlated with the amount of light deposited inside the array are useful for separating UHE neutrinos from muon bundles. Reconstruction variables are also useful for separating the primarily horizontal signal from downgoing muon bundles. The specifics of this are described below.

4.2 Method

All variables used in this analysis are expected to show good agreement between simulated and experimental data, especially at lower levels where the data is expected to be dominated by background. Variables with too strong of a disagreement are discarded (see Fig. 4.1 for an example). Additionally, in order to

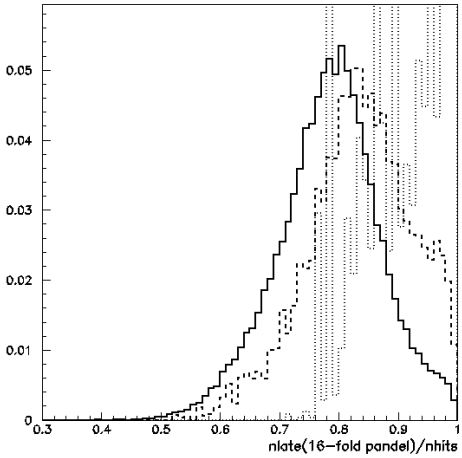

Figure 4.1: An example of a discarded variable. This is the number of hits with a time residual greater than 150 ns divided by the total number of hits. Although this variable shows some separation between background (dashed line) and signal (dotted line), the disagreement between data (solid line) and background simulation is too large to include this variable in the UHE analysis.

avoid choosing overly precise selection criteria values, selection values were used in units no smaller than 1/30 of the variable range, which is a reasonable estimate of the discriminating power of the detector. Final selection values were determined by optimizing the model rejection factor (MRF) for an E^{-2} muon neutrino spectrum [45]. The MRF is given by:

$$\mathrm{MRF} = \frac{\bar{\mu}_{90}}{N_{\mathrm{signal}}} \tag{4.1}$$

Table 4.1: Selection criteria for the UHE analysis.

Level	Selection Criteria	
0	Preprocessing	
1	F1H < 0.72 NHITS > 140	
2	Flare Cleaning F1H < 0.53	
	Cascade-like	Muon-like
3	$L_{casc} < 7$	$L_{casc} \geq 7$
	NN > 0.93	Zenith Angle > 85
4	F4H < 0.1	$L_{muon} < 6.9$
5	$F1H_{ELEC} < 0.56$	-
6	$L_{60} < 6.6$	-

where $\bar{\mu}_{90}$ is 90% confidence level (CL) average event upper limit given by Feldman & Cousins [32], and N_{signal} is the number of muon neutrinos expected for an E^{-2} spectrum. The selection criteria are summarized in Table 4.1.

4.3 Preprocessing & Flare Cleaning

Unless specifically stated otherwise, experimental and simulated data sets underwent the same steps of preprocessing. The data from 2000 was processed using the Siegmund software package [29]. Study of the 2000 data after processing led to some minor changes in hit cleaning for the 2001/2002 data which improved the rejection of background atmospheric muon events for lower energy analyses. Additionally, improvements in computer processing speed allowed the addition of some extra noise filtering. The 2001/2002 data was processed using the Sieglinde software package [30].

File Selection: A file is the smallest data unit and covers roughly 10 minutes of data taking time. A list of bad files were selected using the noise and leading edge rates of all OMs. If more than 10% of the OMs in a file have a noise rate

that is too high, this file is rejected. Simulation data sets do not undergo this selection.

OM Selection: A list of bad OMs is generated by looking at their global noise and leading edge rates. For 2000, 115 OMs were found to be bad, with shorter lists of additional OMs excluded for three separate periods during the year. For 2001, 99 OMs were found to be bad and 98 OMs were found to be bad in 2002. These OMs are removed.

TOT Cleaning: TOT cleaning is done to remove hits caused by noise or cross-talk, a phenomenon which occurs when signals in one OM induce a signal in the electrical cables of another OM. These hits will have a very different TOT value; thus hits with TOTs that are too short or too long are removed. For OMs on strings 1 - 10 the TOTs values were generally required to be between 75 ns and 2000 ns. For OMs on strings 11 - 19 the TOT range was 5 - 2000 ns for OMs connected to the surface with optical cables and 75 - 2000 for OMs connected with electrical cables. For 2001/2002 the allowed TOT range for strings 1 - 4 was tightened to 200 ns - 2000 ns.

Retriggering: The hardware trigger of 24 OMs hit within 25 μs is reapplied after removal of bad OMs and tot cleaning.

Amplitude and Isolation Cleaning: In order to further reduce noise, all hits in 2001/2002 are required to have an amplitude greater than 0.1 photoelectrons and must have one neighboring OM within 100 m hit within ± 500 ns.

Timing: For 2000, all hits earlier than 2 μs before the trigger time are removed. In 2001/2002 all hits earlier than 4 μs before the trigger time are removed.

For 2001/2002, an additional set of data quality criteria were added called flare variables [68]. These variables are designed to remove non-physical events caused

Table 4.2: Flare variable values which reject the highest 1% of data from 2001/2002.

Flare Variable	2001 Value	2002 Value
long_missing	1.9	1.9
only_adc	5	-
nch_dead	1.9	2.0
missing_ch	2.2	2.5

by short term detector instabilities. These indicators used in this analysis are:

long_missing - the number of very long hits that started before the data-taking window (i.e. they have no leading edge) + number of hits that started in the noise region and yet have no trailing edge (no TOT)

only_adc - the number of hits that have only an adc value and no leading edge or TOT

nch_dead - the number of hits in OMs that are known to be dead

missing_ch - the number of hits with missing edges between the first and last hit.

Following a procedure outlined in Pohl [68], flare variable selection criteria were chosen such that the highest 1% of the data from 2001/2002 were rejected for each of these variables. These values are shown in Table 4.2. For simplicity, the more stringent values from 2001 were applied to both 2001 and 2002. This results in a loss of 4.4% of observed events for 2001 and 4.2% for 2002. Since these values do not scale with energy, the loss to signal is estimated to be the same as the loss for data. These cuts are applied at selection level 2.

4.4 Level 1 & 2

Due to the large number of events (5.2×10^9 in the three-year analysis), a filter was devised to reduce the data to a manageable size. The filter was designed to

eliminate obvious low energy background events. Criteria were chosen that were effective and computationally fast. This level 1 filter reduces the data sample to 1 - 2% while retaining as much signal as possible.

The first level UHE filter relies on the light density for background muon bundles being less than UHE neutrinos. UHE neutrinos deposit equal or greater amounts of light in the ice than background muon bundles, but background muon bundles spread the light over the cross sectional area of the entire muon bundle, rather than just along a single muon track. Both types of events can generate a large number of hits in the array (Fig. 4.2), but for the same number of hit OMs, the muon bundle has a lower total number of hits, NHITS (recall each OM may have multiple separate hits in one event) as can be seen in Fig. 4.3. The number of secondary hits is further increased by the tendency of bright signals to produce afterpulses in the PMT (for a typical signal file, afterpulse hits account for ~4% of all hits, compared to ~2% for background).

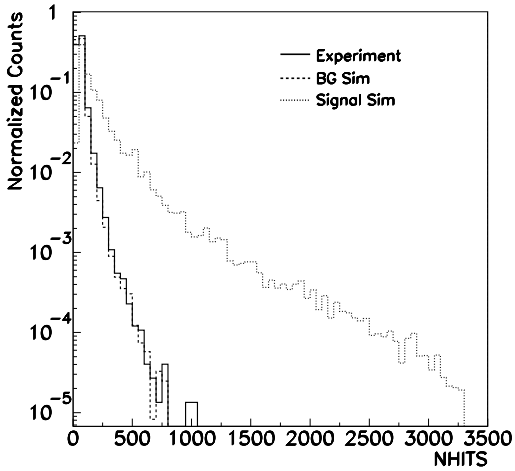

Figure 4.2: NHITS for experiment, background and E^{-2} muon neutrino signal simulation at trigger level.

Background muon bundles also have a higher fraction of OMs with a single hit (F1H), while the UHE neutrino generates more multiple hits (Fig. 4.4). This can be

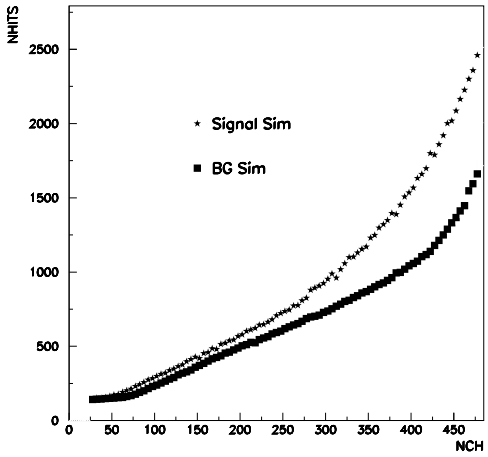

Figure 4.3: Average values of NHITS versus number of hit OMs for E^{-2} muon neutrino and background simulation at selection level 2.

seen in Fig. 4.5, which shows a muon neutrino signal event with an energy of 2×10^{11} GeV and background event from an iron primary with an energy of 10^7 GeV. Both events fill the array with light, but the signal event has higher NHITS and lower F1H values.

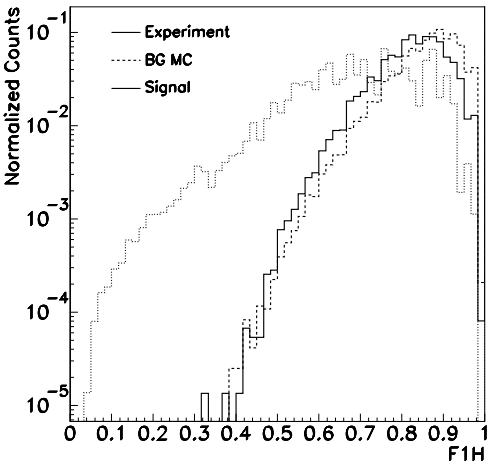

Figure 4.4: F1H for experiment, background and E^{-2} muon neutrino signal simulation at trigger level.

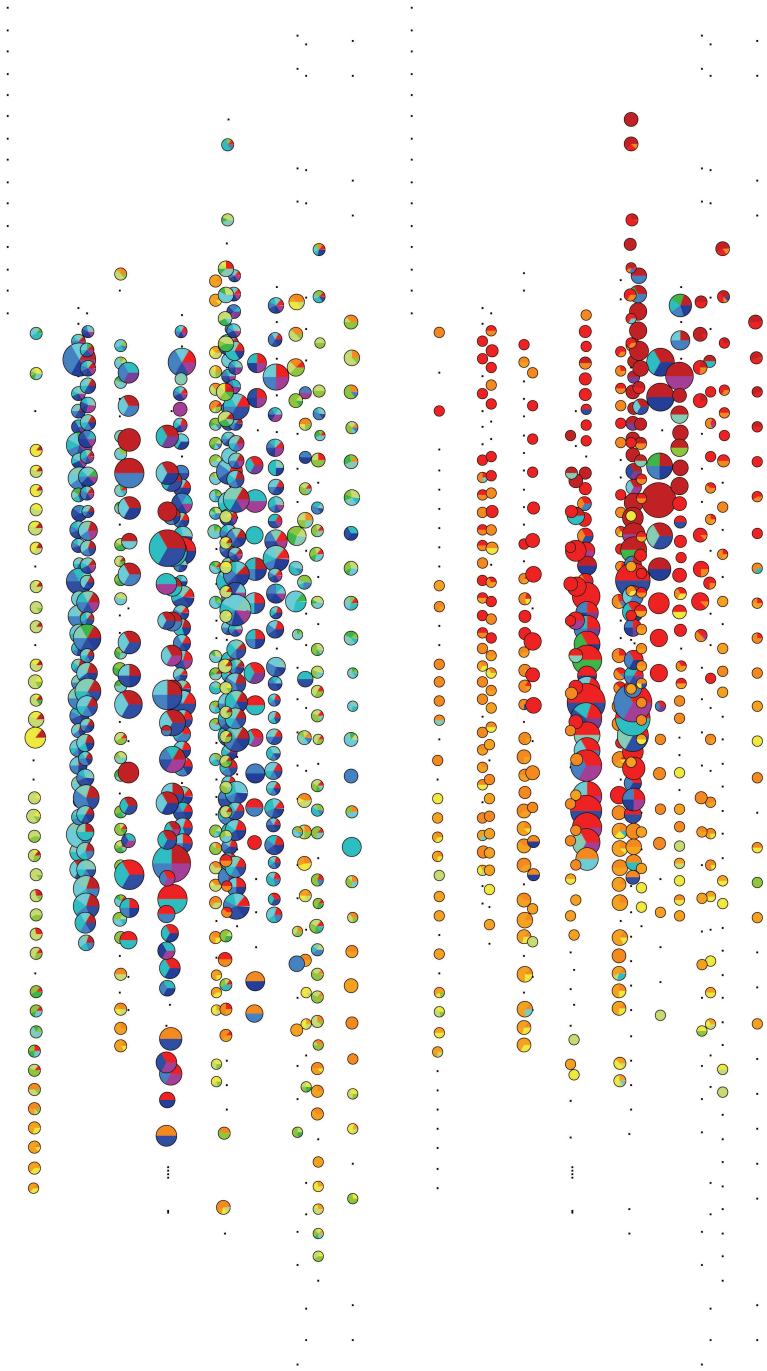

Figure 4.5: Schematic view of a signal event (left) and background event (right). Colored circles represent hit OMs (black dot are OMs that are not hit) and multiple colors represent multiple hits in that OM. The color of the circle indicates the hit time (red is earliest). The size of the circle is correlated with the number of photoelectrons.

Table 4.3: Number of experimental, background and signal data for 456.8 days. Signal rates are shown with a lower energy threshold of 10^4 GeV. Values at the retrigger and level 1 are extrapolated from the 2000 datasets.

Level	Data	BG Sim	ν_{all} Signal Sim ($d(N_{\nu_e}+N_{\nu_\mu}+N_{\nu_\tau})/dE = 10^{-6} \times E^{-2}$)
Retrigger	2.7×10^9	1.8×10^9	621.7
1	3.91×10^7	3.08×10^7	270.8
2	1.426×10^6	9.17×10^5	192.3
3	4.57×10^4	2.67×10^4	88.8
4	150	60	35.0
5	48	32	29.5
6	2	0	20.0

The level 1 selection criteria required that NHITS > 140 and F1H < 0.72; these criteria reduced the data rate to ~1.7% of trigger while still retaining ~45% of the signal relative to trigger. For 2001/2002, this cut was tightened slightly to NHITS > 160 because of the smaller number of bad OMs.

After the level 1 filtering was performed, the number of data events was still too large to reconstruct with the resources available. So the F1H selection criteria was tightened to F1H < 0.53. At this point the samples were reduced to the point where computationally intensive reconstructions became feasible.

4.5 Reconstruction

Four reconstructions are used in the UHE analysis; the Pandel reconstruction, the UHE bundle reconstruction, the cascade reconstruction, and the limited cascade reconstruction. All of these reconstructions use a maximum likelihood function based on the time of the first hit in an OM. The function uses the time residual (t_{res}) which is defined as the difference between the observed hit time and the hit time expected for a photon which travels directly from the muon (or cascade) to

an OM. The maximum likelihood function is given by

$$\mathcal{L}_{time} = \prod_{i}^{Nhits} p(t_{res,i}|a) \tag{4.2}$$

In ideal conditions, $p(t_{res,i}|a)$ would be a delta function. However, as light travels through ice, it is scattered. This broadens the time residual and gives it a large positive tail as the photon travel time is increased by scattering. The time residual is also broadened by the intrinsic jitter of the PMT, the dark noise rate of the PMT and secondary stochastic radiative losses along the muon track, but the dominant factor is scattering of the photon in ice (Fig. 4.6). The photon hit probabilities and

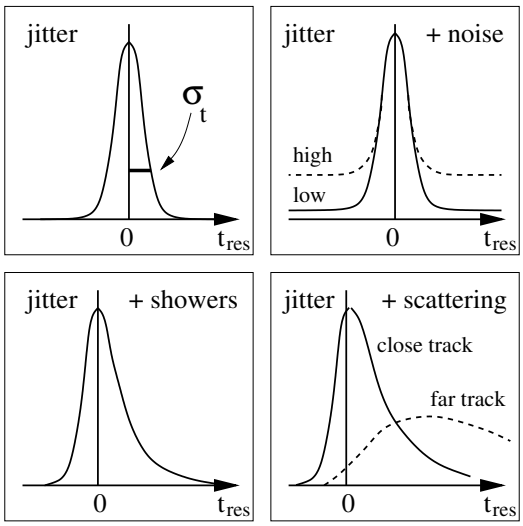

Figure 4.6: Time residual including effects of: (top left) PMT jitter; (top right) PMT jitter and random noise; (bottom left) PMT jitter and secondary cascades; (bottom right) PMT jitter and scattering from ice. Figure taken from [13].

arrival time distributions have already been incorporated into the PTD tables [51] and could be directly drawn from to calculate time residuals for reconstruction. However, it is much faster to parameterize these tables with a simpler function that relates the time residual to distance and use this to calculate the expected time residual. This parameterization, known as the Pandel function, yields similar results as reconstructions using the full PTD tables [13]. The Pandel

function has been further modified to incorporate the jitter of the PMT as well as the possibility of a noise hit causing a non-physical time residual. This modified Pandel function is referred to as the patched Pandel function and is used as the probability distribution function for the Pandel reconstruction.

The Pandel reconstruction minimizes the likelihood function with the patched Pandel function

$$\mathcal{L} = \prod_{i=1}^{NHITS} p_{patched}(d,t) \tag{4.3}$$

and returns a reduced likelihood

$$L = \frac{-log(\mathcal{L})}{NHITS - N_{free}}. \tag{4.4}$$

as well as a vertex (x,y,z), direction (θ,ϕ) and starting time for a muon track.

The UHE bundle reconstruction is similar to the Pandel reconstruction, except that it uses time residuals taken directly from simulations of bundles of cosmic ray muons. These time residuals were fit as a function of distance and energy, so energy is an additional free parameter of this reconstruction. The Pandel reconstruction is used as a seed for the UHE bundle reconstruction.

The cascade reconstruction also uses the patched Pandel function to include scattering in ice, but uses a spherical model of emission when calculating the time residual. Additionally, the probability distribution function is further modified to account for the production of multiple photons using

$$p_n(d,t) = np(d,t)\left(\int_t^\infty p(d,t')dt'\right)^{n-1} \tag{4.5}$$

with the amplitude of the hit used to estimate n, the number of photons. The cascade reconstruction minimizes the probability distribution function given in Eqn. 4.5 to calculate a cascade vertex (x,y,z) and time.

The limited cascade reconstruction removes hits within 60 m of the cascade vertex and reconstructs a new cascade vertex. This reconstruction was originally devised to discriminate between muon tracks and cascades. Low energy muons with a stochastic deposition of light can reconstruct as cascades. By eliminating the OMs within 60 m of the cascade vertex, the fraction of light that is from the underlying muon bundle increases and the muon bundle is more likely to reconstruct poorly as a cascade. In addition to separating muon bundles from UHE cascades from electron and tau neutrinos, this method also works for detecting UHE muons with a large energy deposit along their tracks. This energy deposit is generally about a hundred times higher than the majority of energy deposits from the rest of the UHE muon track and dominates the hit times beyond 60 m from the cascade vertex (see Fig. 4.7 for the energy deposition for a UHE signal event and Fig. 4.8 for the energy deposition for a background muon bundle event).

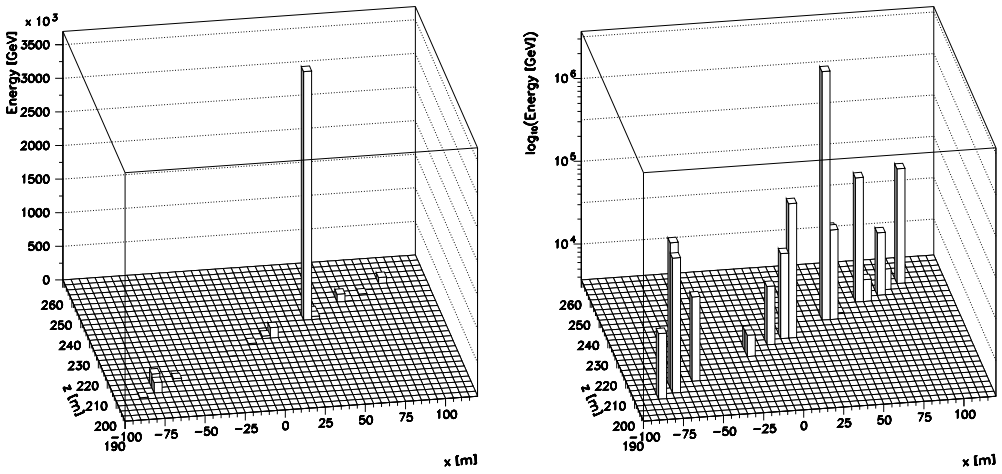

Figure 4.7: Energy deposition along a muon track from a UHE neutrino with an energy of 10^8 GeV as a function of x and z relative to detector center in linear (left) and logarithmic (right) scales.

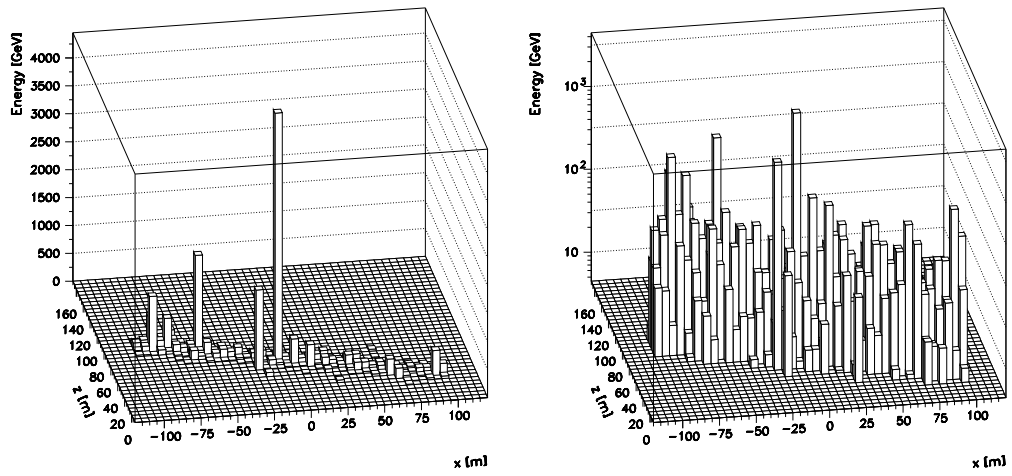

Figure 4.8: Energy deposition along a muon bundle from an iron cosmic ray primary with an energy of 3.5×10^8 GeV as a function of x and z relative to detector center in linear (left) and logarithmic (right) scales.

4.6 Selection Criteria

Once reconstructions have been performed, the data are split into sets according to the likelihood of the cascade reconstruction (L_{casc}). Events with $L_{casc} < 7$ are considered "cascade-like" and the rest are considered "muon-like."

4.6.1 Muon-Like Events

The majority of the background muon bundles and about half of the UHE neutrinos are muon-like (Fig. 4.9). These are generally events which have uniform light deposition along the muon track(s) and are more easily reconstructed by existing reconstruction algorithms than cascade-like events. The zenith angle reconstructed using the UHE bundle reconstruction is shown in Fig. 4.10. The majority of background events come from a downgoing direction, while most of the signal events are clustered around the horizon as expected. Requiring the reconstructed zenith angle be greater than 85° reduces the background by a factor of 10^3.

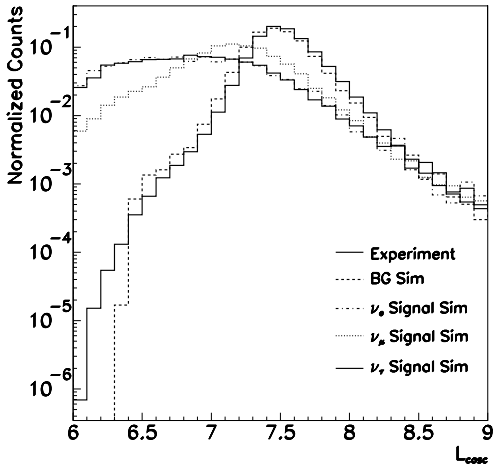

Figure 4.9: Cascade likelihood for experiment, background and E^{-2} neutrino signal simulation after level 2.

The remaining muon bundle events are misreconstructed, since muon bundles come primarily from the downgoing direction. The final selection criteria for the muon-like events requires that these events be well reconstructed by the Pandel reconstruction (L_{muon}). L_{muon} was used because it showed better agreement between background simulations and data than the likelihood of the UHE bundle reconstruction. The selection criterion of $L_{muon} > 6.9$ was chosen so that all background muon bundle events were rejected (Fig. 4.11 and Fig. 4.12), even though 6.9 is not the optimal value. This was done because, despite heroic simulation efforts (see Ch. 3), the statistical uncertainty of the simulation was still quite large. Placing the selection criterion value here results in a very small loss of sensitivity compared to the value found by optimizing the MRF for an E^{-2} muon spectrum (Fig. 4.13).

4.6.2 Cascade-like Events

UHE muon neutrinos that fall into the cascade-like dataset generally deposit a larger fraction of the neutrino energy into a point energy deposit from creation of

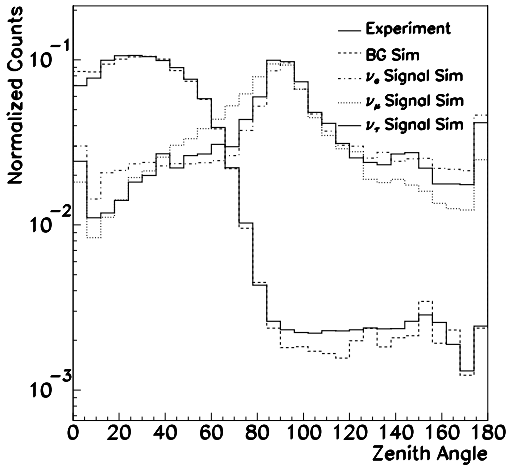

Figure 4.10: Reconstructed zenith angle for experiment, background and E^{-2} neutrino signal simulation after level 2.

an e^+/e^- pair, bremsstrahlung or other process (Fig. 4.14). Background events in the cascade-like subset are characterized by either a large light deposition in or very near the instrumented volume of AMANDA-II or a path which clips the top or bottom of the array (Fig. 4.15). In either case, the energy deposition is significantly less than the energy deposited by a UHE neutrino, allowing application of selection criteria which correlate with energy. As previously mentioned, the F1H variable is a good estimate of energy, but as it has already been applied at an earlier selection level, at this point there is very little discrimination power left in this variable. However, there is still some discrimination power in $F1H_{ELEC}$ (Fig. 4.16), a variable similar to F1H, except that it uses only OMs whose signal is brought to the surface by electrical cables. The signal spreads as it propagates up the cable, causing hits close together in time to be combined. This gives $F1H_{ELEC}$ a different distribution from F1H, but they are both good estimators of energy (Fig. 4.17). The level 3 selection criteria uses the output of a neural net (NN) seeded with $F1H_{ELEC}$, F4H (the fraction of OMs with 4 hits) and F1H as input variables. The neural net was trained using the multi layer

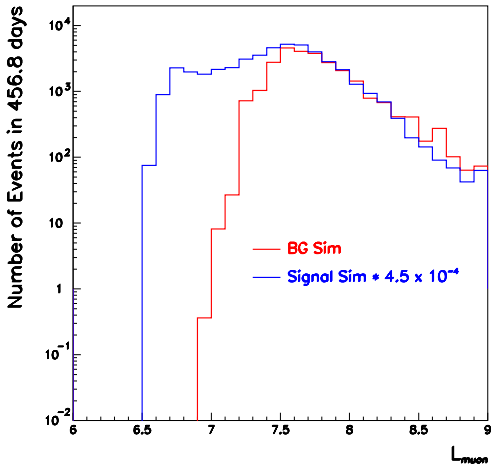

Figure 4.11: L_{muon} distribution at level 3 of this analysis for E^{-2} muon neutrino signal and background simulations. The signal scaling is arbitrary so it will fit on the plot.

perception package in PAW on subsets of background and signal simulation. The level 3 selection criteria requires that NN > 0.93. At this point, the discrimination of the NN is exhausted (Fig. 4.18). However, the input variables themselves still have some discrimination power. Requiring F4H < 0.1 and $F1H_{ELEC}$ < 0.56 removes background events with high weight with very little loss of signal sensitivity (Figs. 4.16 and 4.19). The remaining background muon bundle events are highly energetic and have a different hit distribution than UHE neutrinos. In these background muon bundles, a large light deposition can be washed out by the continuous, dimmer light deposition from hundreds to tens of thousands of muons tracks. In contrast, UHE muons can have one light deposition that is hundreds of times brighter than the light from the rest of the muon track and looks very similar to bright cascades from UHE electron and tau neutrinos. For all cases, the initial cascade reconstruction is generally concentric with this large energy deposition, so ignoring OMs that are within 60 m of the initial cascade reconstruction reduces the fraction of OMs that are triggered with photons from the cascade for background events (Fig. 4.20). For background, the remaining

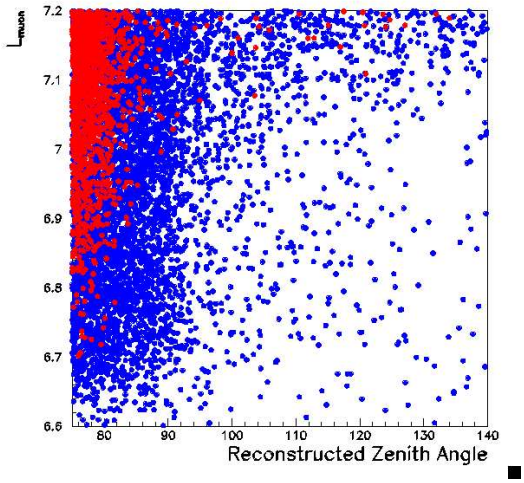

Figure 4.12: L_{muon} versus reconstructed zenith angle. Red dots are background muon bundles and blue dots are UHE neutrino signal.

light will be dominated by light depositions from the tracks of the muon bundles and be less likely to reconstruct as a cascade. In contrast, signal events, with their energetic cascades, will still appear cascade-like and the limited cascade likelihood (L_{60}) will tend to lower values. The final selection criterion for cascade-like events requires that these events be well reconstructed by the limited cascade reconstruction ($L_{60} < 6.6$); this reduces the simulated background expectation to 0 events for this subset.

4.7 Sensitivity and Effective Areas

After applying all selection criteria, there are 0 background muon bundle events expected for 456.8 days. This gives a 90% CL event upper limit of 2.44 [32] and a sensitivity (without incorporating systematic and statistical uncertainties) of 1.2×10^{-7} GeV cm^{-2} s^{-1} sr^{-1}, with 90% of the E^{-2} signal found in the energy range 2×10^5 GeV to 10^9 GeV. Table 4.4 shows the expected number of each flavor of UHE neutrino passing the final selection level for a $10^{-6} \times E^{-2}$ flux. The spectra of the events passing all section criteria are shown in Fig. 4.21. The effective neutrino

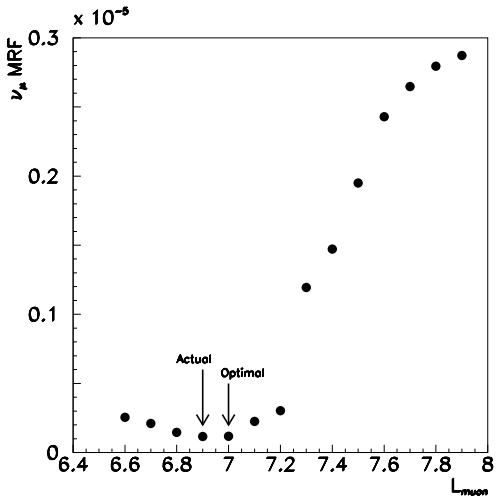

Figure 4.13: Model rejection factor for E^{-2} muon neutrinos as a function of cut level for L_{muon}. Here the optimal MRF is found at a value of 7, but the value used in this analysis is tightened to 6.9 so that all background events are removed with only a small loss in sensitivity.

Table 4.4: Number of simulated neutrino events in the cascade-like and muon-like subsets passing all selection criteria for three years for a neutrino spectrum of $d(N_{\nu_e}+N_{\nu_\mu}+N_{\nu_\tau})/dE = 10^{-6} \times E^{-2}$ GeV $^{-1}$ cm^{-2} s^{-1} sr^{-1}.

Neutrino Flavor	Cascade-like	Muon-like	Total
Electron	7.7	0.1	7.8
Muon	3.9	3.6	7.5
Tau	4.4	0.3	4.7
All Flavors			20.0

area is shown in Fig. 4.22 after all selection criteria have been applied. The values shown are the average of the effective areas from 2000, 2001 and 2002, weighted with the livetimes of each year.

4.8 Systematic Uncertainties

Because there is no test beam which can be used to determine the absolute sensitivity of the AMANDA-II detector, calculations of sensitivity rely on simulation. The dominant sources of uncertainty in this calculation are due to the

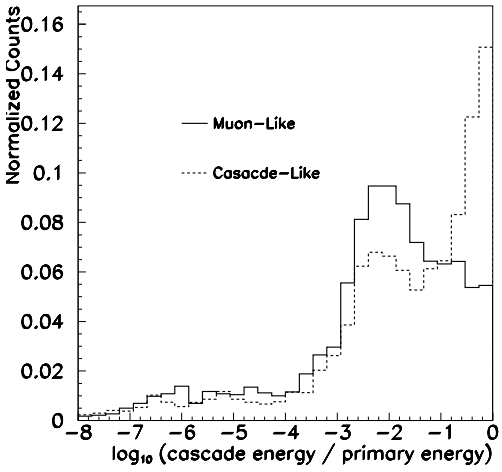

Figure 4.14: The ratio of cascade energy to primary neutrino energy for "muon-like" and "cascade-like" E^{-2} muon neutrinos at selection level 2.

normalization and composition of the cosmic ray flux, detector sensitivity and neutrino cross section. These uncertainties are summed in quadrature separately for background and signal and have been included into the final limit with a flat distribution using the method described in [79].

4.8.1 Normalization of Cosmic Ray Flux

The average energy of cosmic ray primaries at the penultimate selection level is 4.4×10^7 GeV, which is considerably above the knee in the cosmic ray spectrum. At these energies only indirect measurements of the cosmic rays spectrum are possible because of severely reduced flux. Numerous experiments have measured a large spread in the absolute normalization of the flux of cosmic rays at this energy (Fig. 4.23). Estimates of the error in the normalization of the cosmic ray flux range from 20% [47] to a factor of two [67]. This analysis uses the more conservative uncertainty of a factor of two.

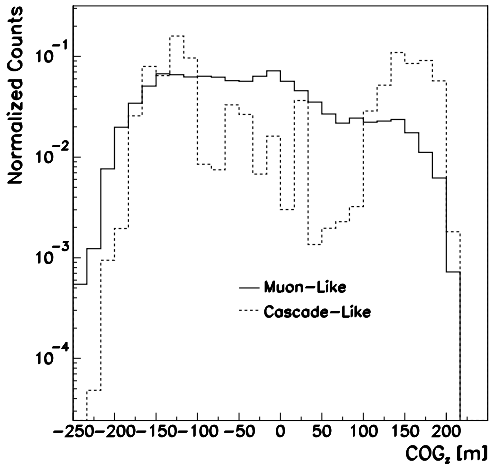

Figure 4.15: The center of gravity of depth for background simulation at selection level 2. Events with a very low or high COG_z clip the top or bottom of the array.

4.8.2 Cosmic Ray Composition

There is considerable uncertainty in the cosmic ray composition above the knee [67]. As described in Section 3.1, cosmic rays are simulated using only iron and proton primaries reweighted to the cosmic ray spectrum using a method described in Glasstetter et al. [37]. This results in the iron flux dominating the proton flux by a factor of 4 - 10 at the highest energies. This is in disagreement with the results from a number of experiments designed to measure the flux of cosmic rays. Generally these experiments have found a spectrum that gets lighter (i.e. more proton dominated) as the energy increases [25]. This can be included in the simulation by altering the weighting of the cosmic ray simulation such that protons become the dominant flux at the highest energies. Table 4.5 shows the difference in passing rates at each selection level for simulated data with proton- and iron-dominated fluxes and experimental data. The ratio of number of events for iron-dominated spectrum to proton-dominated spectrum at the penultimate selection level is 1.94 ± 0.54, including statistical uncertainty. Subtracting the statistical uncertainty gives a factor of 1.4 more iron-dominated events than

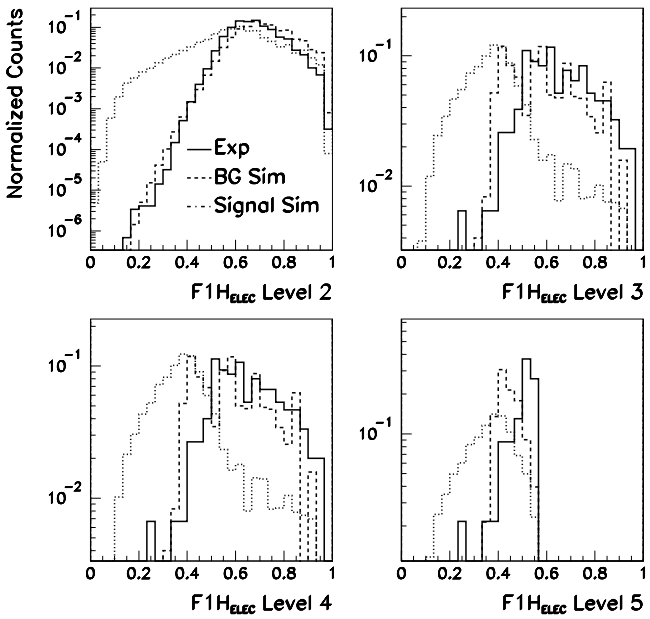

Figure 4.16: $F1H_{ELEC}$ for experiment, background and E^{-2} neutrino signal at selection level 2 through 5. The level 4 selection criteria removes events with $F1H_{ELEC} < 0.56$.

proton-dominated events. This leads to a percentage difference in event rates of 30%, which is taken as the uncertainty due to cosmic ray composition.

4.8.3 Detector Sensitivity

The optical properties of the refrozen ice around each OM, the absolute sensitivity of individual OMs, and obscuration of OMs by nearby power cables can effect the

Table 4.5: Passing rates for experimental data, iron- and proton-dominated cosmic ray simulations at each selection level for 2001. Uncertainties shown are statistical.

Level	Experiment	Iron-dominated	Proton-dominated
2	476000	344947	436078
3	14595	11005 ± 673	11271 ± 300
4	70	27.6 ± 5.4	25.7 ± 6.2
5	22	12.4 ± 2.4	6.4 ± 1.3
6	1	0	0

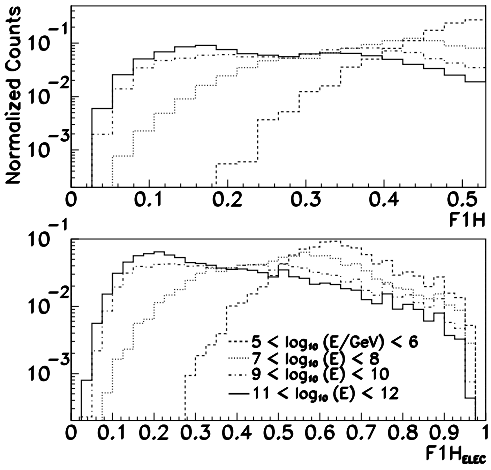

Figure 4.17: F1H (top) and $F1H_{ELEC}$ (bottom) distributions for various energy decades of muon neutrino signal. These variables serve as rough estimators of energy for the UHE analysis.

detector sensitivity. This analysis uses the value obtained in Ahrens et al. [12] where the OM sensitivity was varied by 15% and found to cause a 15% variation in the signal rate. Variations larger than this are not considered because they cause disagreement between the simulated atmospheric neutrino and experiment data rates. This uncertainty is applied to simulations of both background cosmic ray events and neutrino signal events.

4.8.4 Implementation of Ice Properties

As photons travel through the ice they are scattered and absorbed. The absorption and scattering lengths of the ice around the AMANDA-II detector have been measured very accurately using in situ light sources [8]. Uncertainties are introduced due to the limited precision with which these parameters are included in the simulation. Varying the scattering and absorption lengths in the detector simulation by 10% were found to cause a difference in number of expected signal events (for an E^{-2} spectrum) of 34% [7], which is used as a

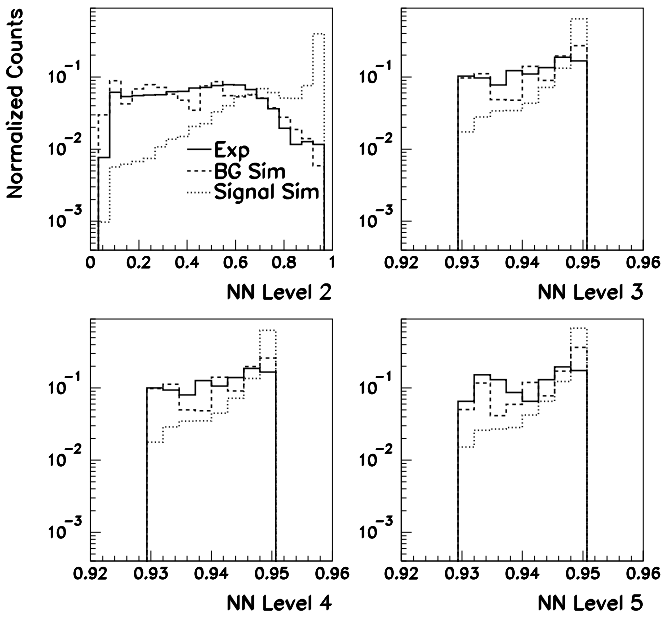

Figure 4.18: The output of the neural net for experiment, background and E^{-2} neutrino signal at selection level 2 through 5.

conservative estimate of the uncertainty due to implementation of ice properties.

4.8.5 Neutrino Cross Section

The uncertainty in the standard model neutrino cross section has been quantified recently [16], taking into account the experimental uncertainties on the parton distribution functions measured at HERA [26], as well as theoretical uncertainties in the effect of heavy quark masses on the parton distribution function evolution and on the calculation of the structure functions. The corresponding maximum variation in the number of expected signal events (for an E^{-2} spectrum) is 10%, in agreement with previous estimates [7].

Screening effects are expected to suppress the neutrino-nucleon cross section at energies in excess of 10^8 GeV (see e.g. [25, 55]). This has a negligible effect on the number of signal events expected for an E^{-2} spectrum because the majority of

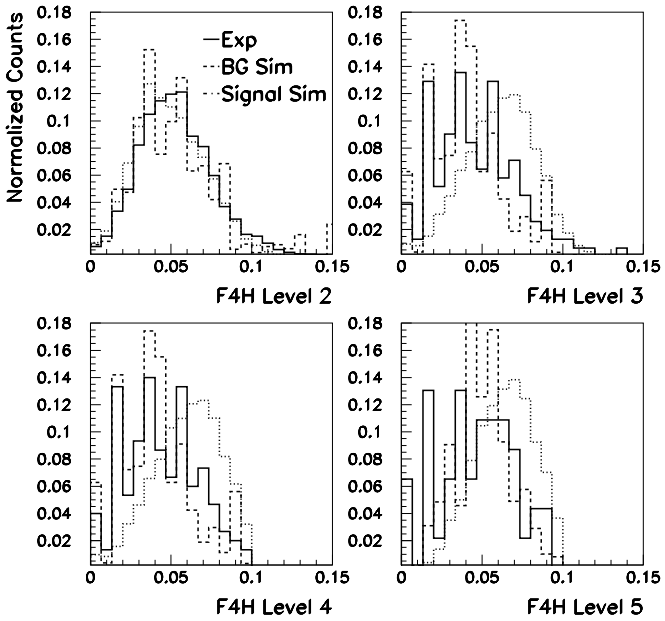

Figure 4.19: F4H for experiment, background and E^{-2} neutrino signal at selection level 2 through 5. The level 4 selection criteria requires events have F4H < 0.1.

signal is found below these energies (Fig. 4.21). Even if the suppression is as extreme as in the Colour Glass Condensate model [42], the event rate decreases by only 11%. These screening models are considered extreme bounds of the possible uncertainty in the neutrino-nucleon cross section. They are presented only to give an idea of the range of possible fluctuations in the cross section and are not included in the cross section uncertainty.

4.8.6 Differences in Simulated Distributions

An examination of the L_{muon} distribution for the "muon-like" subset after level 3 of this analysis suggests the background simulation is shifted by one bin (corresponding to a shift in L_{muon} by -0.1) relative to the experiment (Fig. 4.26). Shifting the simulation distribution to the left by one bin leads to better agreement between the background simulation and experimental distributions and an

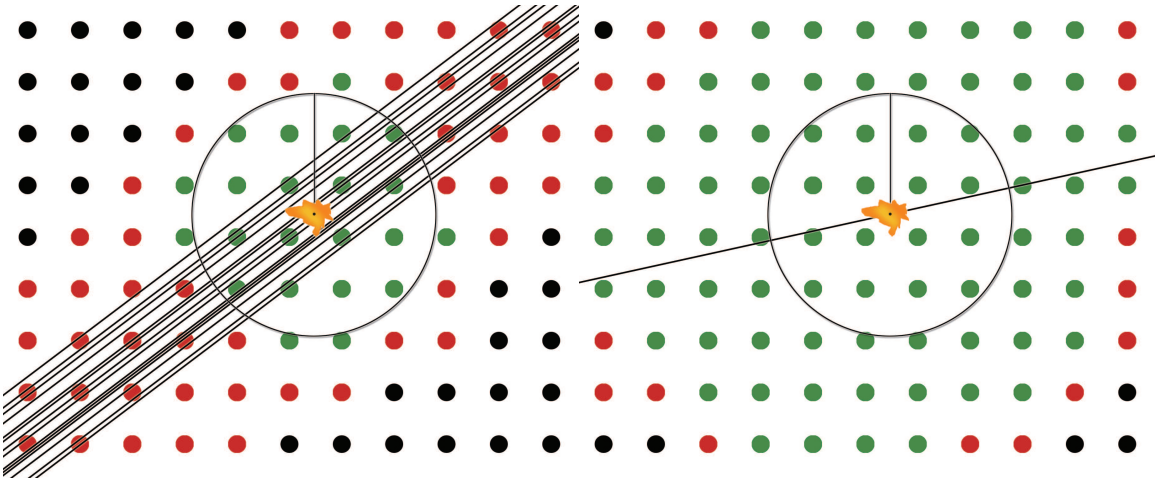

Figure 4.20: Cartoon of light deposition for a cascade for background muon bundles (left) and UHE neutrino signal (right). The black dots are OMs, the red dots are OMs hit by light from the muon track(s) and the green dots are OMs hit by light from the cascade and the muon track(s). At distances greater than 60 m, light in the background event is dominated by the muon tracks, while signal light remains dominated by light from the cascade to much greater distances.

increase in 8% in the number of expected signal events for an E^{-2} spectrum.

4.8.7 The Landau-Pomeranchuk-Migdal (LPM) Effect

At ultra high-energies, the LPM effect suppresses the bremsstrahlung cross section for electrons and the pair-production cross section of photons created in a cascade by an electron neutrino [56, 64]. This lengthens the resultant shower produced by a factor that goes as $\sqrt{E}$ (Fig. 4.24). Above 10^8 GeV, the extended shower length becomes comparable to the spacing between OMs on a string [52]. Additionally, as the LPM effect suppresses the bremsstrahlung and pair productions cross sections, photonuclear and electronuclear interactions begin to dominate which lead to the production of muons inside the electromagnetic cascade. Toy simulations were preformed which superimposed a muon with an energy ranging up to 10^5 GeV onto a cascade with an energy of 10^8 GeV. While the addition of the muon shifted the L_{casc} distribution 5% towards higher (more

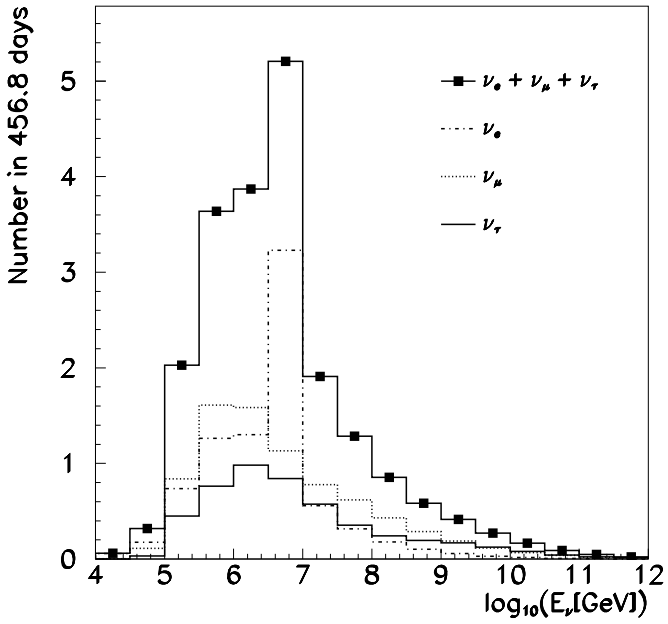

Figure 4.21: The energy spectra of electron, muon, and tau neutrino signal events ($d(N_{\nu_e}+N_{\nu_\mu}+N_{\nu_\tau})/dE = 10^{-6} \times E^{-2}$ GeV $^{-1}$ cm^{-2} s^{-1} sr^{-1}) which pass all selection criteria. The peak in the electron neutrino spectrum just below 10^7 GeV is due to the Glashow resonance.

muon-like) values (Fig. 4.25), the resulting events still passed all selection criteria (Table 4.6) indicating that the effects of muons created inside cascades by the LPM effect are negligible.

The LPM effect is not included in the simulations of electron neutrinos, but it can be approximated by excluding all electron neutrinos with energies in excess of 10^8 GeV. This is an overestimation of the uncertainty introduced by the LPM effect, as extended showers may manifest as several separate showers which are likely to survive all selection criteria and the addition of low-energy muons is not expected to significantly alter the UHE cascade light deposition. Neglecting electron neutrinos with energies in excess of 10^8 GeV reduces the number of expected signal events by 2% for an E^{-2} spectrum.

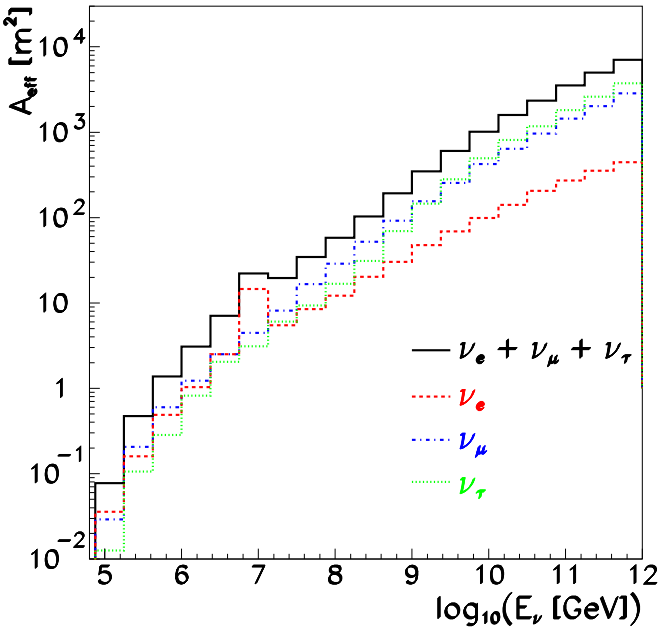

Figure 4.22: The average effective are for electron, muon and tau neutrino signal after all selection criteria have been applied.

4.8.8 Statistical Error of Simulations

No background simulation event survives all the selection criteria. This value has a statistical error that can typically be estimated from the differences in livetime between background simulation and experimental livetimes. However, in this case, optimized simulations (detailed in Section 3.1) were done which make it very difficult to estimate a simulation livetime. Instead, an uncertainty of 1.29, the 1σ Feldman-Cousins upper event limit on zero observed events, is assumed at the final selection level [32].

Signal simulation has an average statistical error of 5% (exact numbers for each flavor and year are shown in Table 3.3).

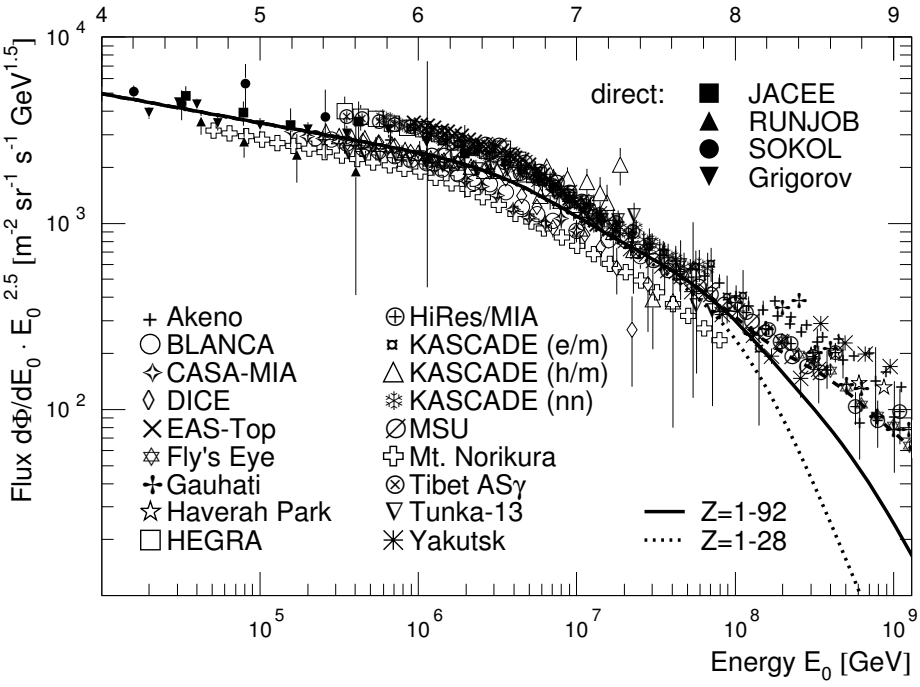

Figure 4.23: Measurements of the all particle cosmic ray flux from direct and indirect measurements. Figure taken from [47].

4.8.9 Summary of Uncertainties

The systematic uncertainties are summarized in Table 4.7. Summing the systematic errors of the signal simulation in quadrature gives a total systematic uncertainty of ± 39%. Combining this with the statistical uncertainty of ~5% per neutrino flavor gives a total maximum uncertainty of 40%. Following a similar method for the background simulation, the systematic uncertainty is +101% / -60%. Scaling the statistical uncertainty of the background simulation by the systematic uncertainty gives a maximum background expectation of fewer than 2.6 events for three years.

Table 4.6: Number of events (out of 500) passing all selection criteria for the UHE analysis for toy simulations of LPM effect. The cascade was placed at two different distances from the center of the detector.

Cascade distance [m]	Muon energy [GeV]	Number
43	none	483
43	1	480
43	10^2	474
43	10^3	482
43	10^4	480
43	10^5	481
180	1	409
180	10^2	423
180	10^3	422
180	10^4	427
180	10^5	424

Table 4.7: Summary of simulation uncertainties for background and signal simulation sets.

Source	BG Sim	Sig Sim
Cosmic Ray Normalization	+100% / -50%	-
Cosmic Ray Composition	-30%	-
Detector Sensitivity	±15%	±15%
Ice Properties		±34%
Neutrino Cross Section	-	±10%
Simulation Distribution	-	+8%
LPM Effect	-	-2%
Total	+101% / -60%	+39% / -39%

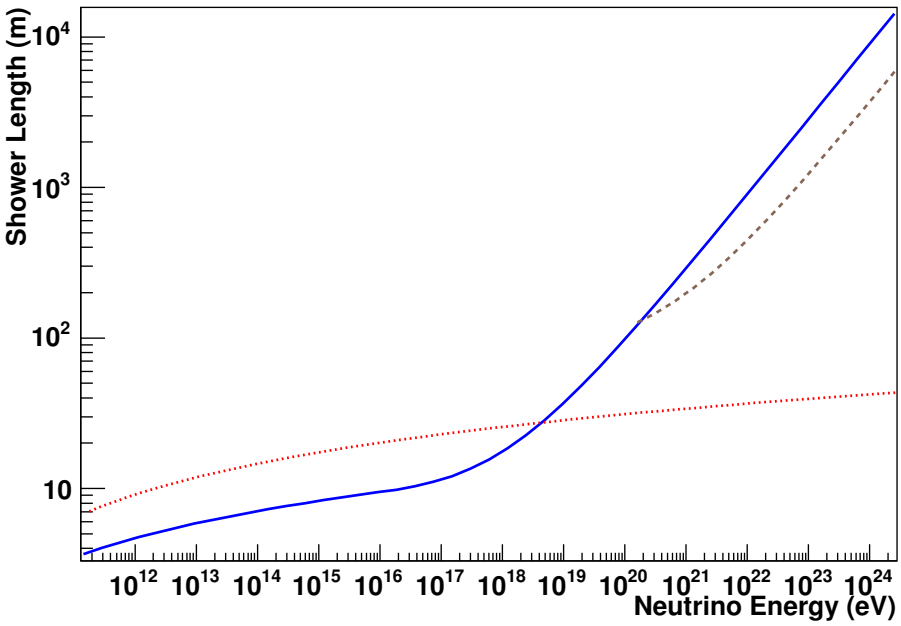

Figure 4.24: The length of a shower enhanced by the LPM effect. The blue line shows the length for an electromagnetic shower, the dashed line shows the length for a hybrid electromagnetic/hadronic shower and the red line shows the length for a hadronic shower. Figure taken from [52].

4.9 Results

Two events are observed in the data sample at the final selection level, while fewer than 2.6 background events are expected for a livetime of 456.8 days (Fig. 4.26). Schematic views of these two events are shown in Fig. 4.27. This leads to a 90% CL average event upper limit of 5.3, combining this with the signal expectation of 20 events from a $10^{-6} \times E^{-2}$ spectrum gives an upper limit on the all-flavor neutrino flux of

$$E^2\Phi_{90\%CL} \leq 2.7 \times 10^{-7} \text{GeV cm}^{-2} \text{ s}^{-1} \text{ sr}^{-1} \tag{4.6}$$

including systematic uncertainties, with 90% of the E^{-2} signal found between the energies of 2×10^5 GeV and 10^9 GeV (Fig. 4.28).

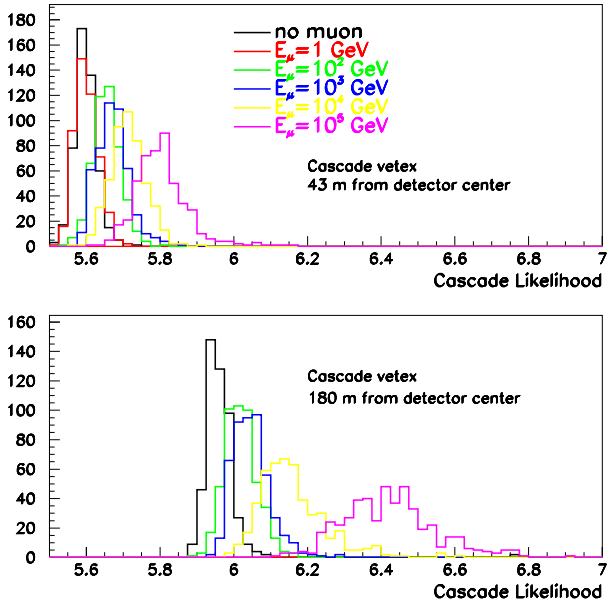

Figure 4.25: The L_{casc} distribution for toy simulations in which a muon of successively higher energies is superimposed onto a 10^8 GeV cascade.

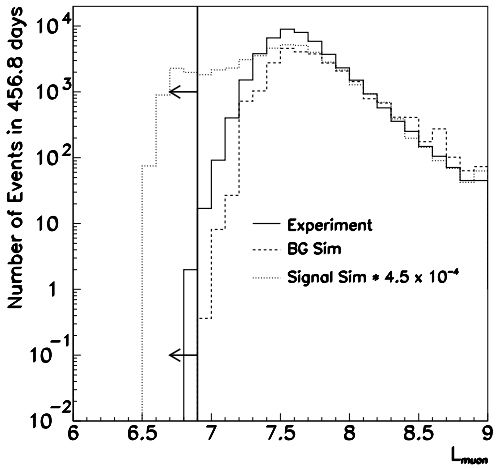

Figure 4.26: L_{muon} distribution for the experiment, background air shower, and E^{-2} muon neutrino signal simulations after level three of this analysis. Two experimental events survive the final selection criteria of $L_{muon} < 6.9$. The signal simulations are reduced by a factor of 4.5×10^{-4} to fit in the plot.

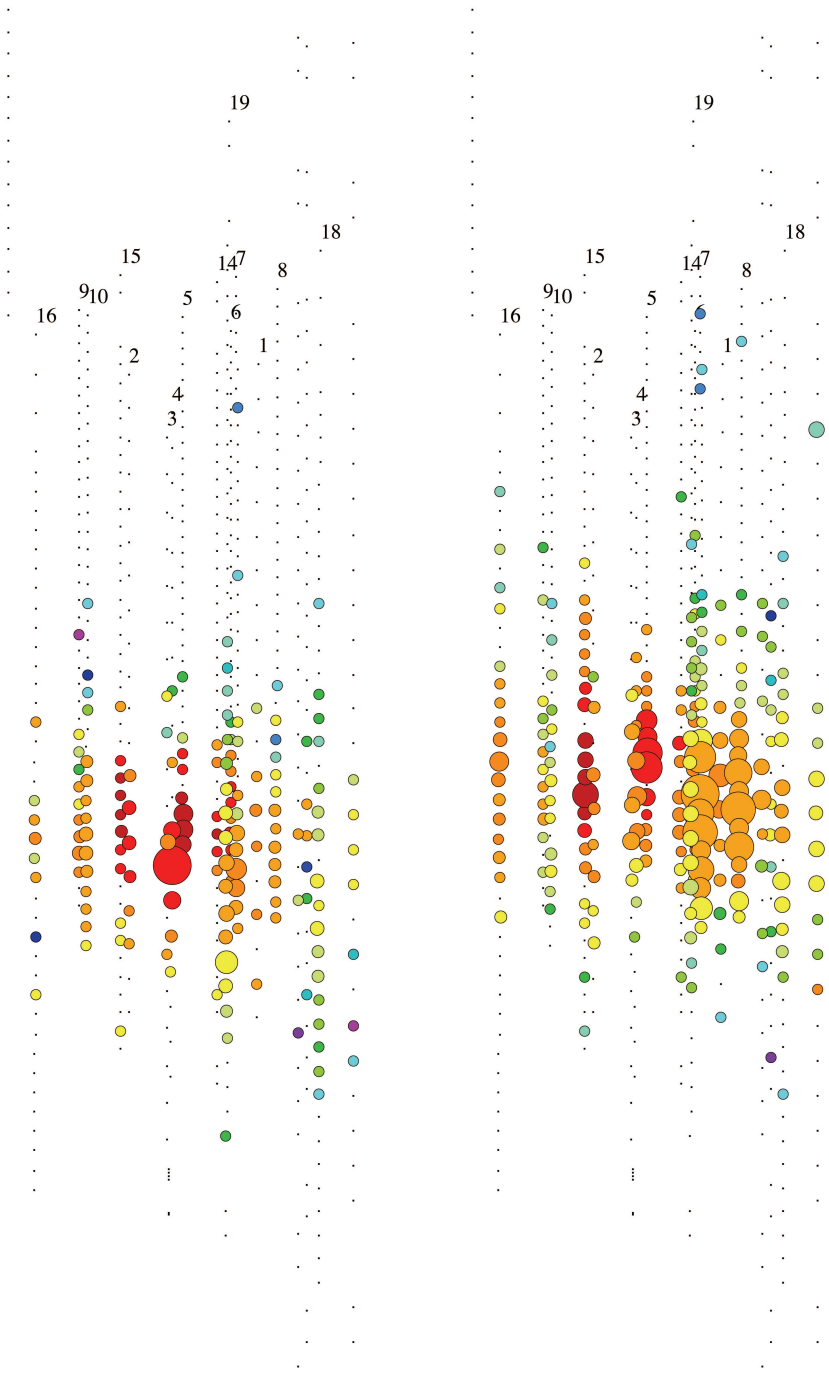

Figure 4.27: Schematic view of the events which pass all selection criteria for 2001 (left) and 2002 (right). Here only the first hit in each OM is shown so that the structure can be seen more clearly. Colored circles represent hit OMs (black dot are OMs that are not hit). The color of the circle indicates the hit time (red is earliest). The size of the circle is correlated with the number of photoelectrons.

4.9.1 Non-E^{-2} Spectra

The number of expected events per neutrino flavor (ν_x and $\bar{\nu}_x$) for spectra with shapes other than an E^{-2} spectrum can be calculated using the formula

$$N_{signal} = T \int dE_\nu d\Omega \Phi_{\nu,all}(E_\nu) A_{eff}(E_\nu, \theta_\nu) \tag{4.7}$$

where T is the total live time (456.8 days), A_{eff} is the neutrino effective area (Fig. 4.22) and $\Phi_{\nu,all}$ is the flux at the Earth's surface. A number of theories predict fluxes which can be tested in this manner (Fig. 4.28 and Table 4.8).

These include Stecker et al.'s hidden-core AGN model [76] which has been updated to reflect recent measurements [75], as well as AGN models in which neutrinos are accelerated in optically thin regions [39, 61, 62, 69]. Including uncertainties, this analysis excludes at a 90% CL the AGN models from Halzen & Zas [39] and Mannheim et al. [62]. The previously rejected [7] models from Protheroe [69] and Stecker et al. [76] are also rejected at the 90% CL by this analysis (see Fig. 4.29 and Table 4.8).

Fluxes of neutrinos from the decay of topological defects [70] or Z-bursts [49, 87] peak at too high of an energy to be detected by this analysis. Neutrinos from the interaction of cosmic rays with cosmic microwave background photons are produced at too low of a flux for this analysis to detect (see Table 4.8).

Although the number of events predicted for Stecker's [75] hidden-core AGN model was too low to eliminate it at the 90% CL, it is possible to set limits on the parameters in the model. In this model, the flux of neutrinos is normalized to the extragalactic MeV photon flux measured by COMPTEL [63]. It is assumed that the flux of photons from AGNs is responsible for 10% of this MeV background [75]. If the neutrino flux scales linearly with this value, then the maximum contribution

Table 4.8: Flux models, the number of neutrinos of all flavors expected at the Earth at the final selection level, and the MRFs for 456.8 days of livetime. A MRF of less than one indicates that the model is excluded with 90% confidence.

Model	ν_{all}	MRF
AGN (Protheroe [69])[a]	20.6	0.3
AGN (Stecker et al. [76])[a]	17.4	0.3
AGN (Halzen & Zas [39])[a]	8.8	0.6
AGN (Mannheim et al. [62])[a]	5.9	0.9
AGN RL B (Mannheim [61])[a]	4.5	1.2
Z-Burst (Kalashev et al. [49])	2.0	2.7
AGN (Stecker [75])	1.8	2.9
GZK ν norm AGASA (Ahlers et al. [9])[b]	1.8	2.9
GZK ν mono-energetic (Kalashev et al. [50])	1.2	4.4
GZK ν α=2 (Kalashev et al. [50])	1.1	4.8
GZK ν norm HiRes (Ahlers et al. [9])[b]	1.0	5.3
TD (Sigl et al. [70])	0.9	5.9
AGN RL A (Mannheim [61])[a]	0.3	18.0
Z-Burst (Yoshida et al. [87])	0.1	53.0
GZK ν (Engel et al. [31])	0.06	88.0

[a] These values have been divided by two to account for neutrino oscillation from a source with an initial 1:2:0 ν_e:ν_μ:ν_τ flux.

[b] Lower energy threshold of 10^7 GeV applied.

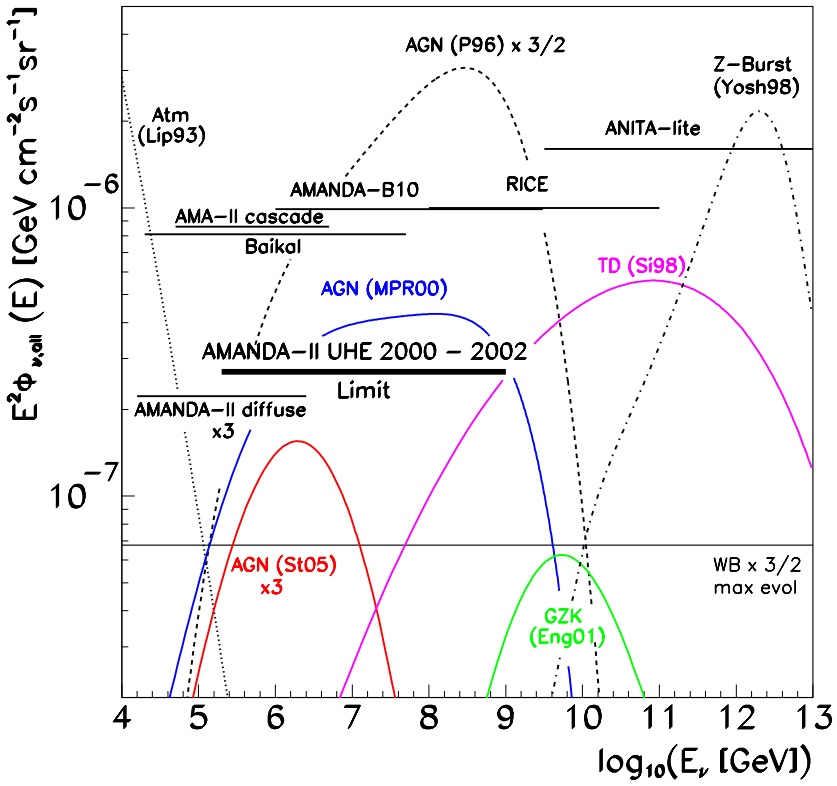

Figure 4.28: The UHE all flavor flux limit. Also shown are existing all flavor neutrino flux experimental limits and theoretical bounds. Experimental limits shown are from the RICE [54], ANITA-lite [24], Baikal [21], AMANDA-B10 [7] experiments, as well as the low-energy diffuse [5] and cascade [6] limits using AMANDA-II. The theoretical bound WB is from [22]. Also shown are several representative models: St05 from [75], MPR00 from [62], P96 from [69], Eng01 from [31], Sig98 from [70], and Yos98 from [87].

of hidden-core AGNs to the extragalactic MeV photon flux must be less than

$$\%_{\mathrm{MeV}} < \frac{\text{90\% CL average event upper limit}}{\text{number of events from AGN}} \times 10\%$$
$$\%_{\mathrm{MeV}} < \frac{5.3}{1.8} \times 10\%$$

Therefore, the contribution of hidden-core AGNs to the extragalactic MeV photon flux must be less than 29%.

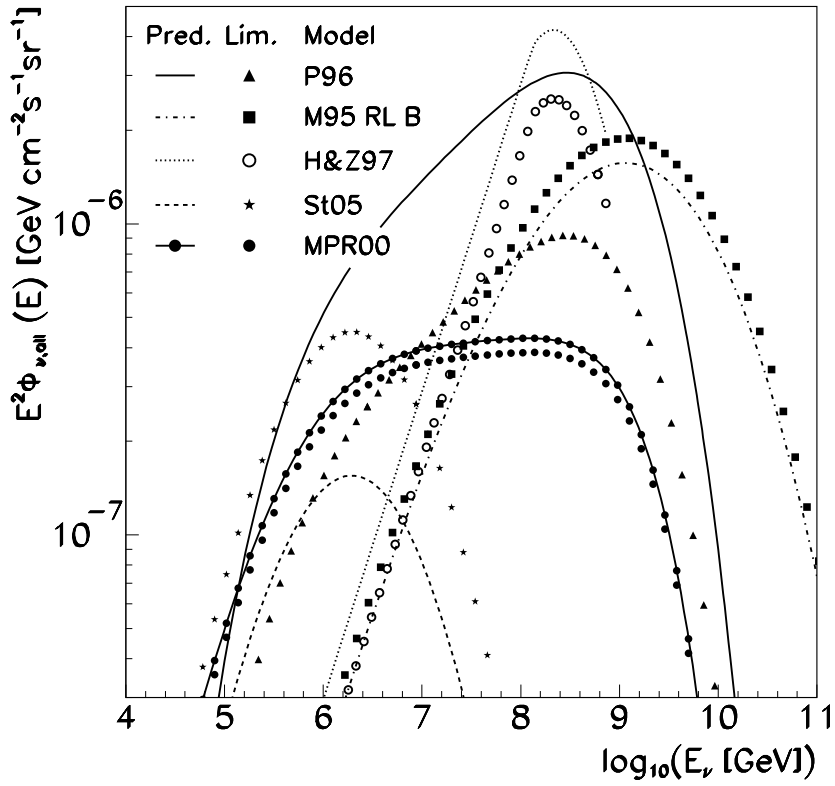

Figure 4.29: The fluxes from various AGN models scaled by their MRFs. Lines denote the model predictions and symbols denote the 90% CL limits on the predictions derived by this analysis.The models rejected at the 90% CL shown are: H&Z97 from Halzen & Zas [39], P96 from Protheroe [69], and MPR00 from Mannheim et al. [62]. Also shown are models close to being rejected: Mann95RL B from Mannheim [61] and St05 from Stecker [75]. See Table 4.8 for exact numbers.

4.9.2 Microscopic Black Hole Creation

As described in Section 1.3, postulating extra dimensions allows the creation of microscopic black holes at center of mass energies on the order of 1 TeV. This additional interaction channel leads to increases in the neutrino-nucleon cross section as high as a factor of 100 at 10^{11} GeV. Simulations were preformed using the highest enhanced cross section predicted by Anchordoqui et al. [18] (1 extra dimension, M_D = 1 TeV and $M_{min}{}^{BH} = M_D$, shown in Fig. 1.6), with the assumption that when a neutrino interacts to form a microscopic black hole, all of its energy is

passed on to an electronic cascade. This represents an overestimation, since only about 75% of the energy from a microscopic black hole goes into a cascade [15]. The resulting samples were reweighted so that their spectrum was consistent with the most conservative GZK flux tested in this paper (Engel et al. [31], labeled "GZK (Engel01)" in Fig. 1.5) and all of the selection criteria detailed above were applied. The number of expected events from this GZK flux with an enhanced cross section is 1 event in 456.8 days of livetime. Since this is less than the 90% CL event upper limit of 5.3, it is not possible to limit the enhancement of the neutrino-nucleon cross section due to the production of microscopic black holes.

However, it is possible to place limits on the black hole cross section relative to the Waxman-Bahcall bound. Following a method outlined in Anchordoqui, Feng & Goldberg [17], the number of downgoing events is proportional to $\sigma_{\nu N}/\sigma_{SM}$. For an unknown, downgoing neutrino flux Φ^{ν}

$$\Phi^{\nu}\frac{\sigma_{\nu N}}{\sigma_{SM}} < \Phi^{\nu}_{max} \tag{4.8}$$

where Φ^{ν}_{max} is the maximum flux limit per neutrino flavor derived by this analysis (9×10^{-8} GeV cm^{-2} s^{-1} sr^{-1}). Dividing both sides of Eqn. 4.8 by the Waxman-Bahcall bound for one neutrino flavor (here 2×10^{-8} GeV cm^{-2} s^{-1} sr^{-1} is the value used by Anchordoqui, Feng & Goldberg [17]) gives

$$\frac{\Phi^{\nu}}{\Phi^{\nu}_{WB}}\frac{\sigma_{\nu N}}{\sigma_{SM}} < 4.5 \tag{4.9}$$

with a similar result for the case of neutrino cross section screening

$$\frac{\Phi^{\nu}}{\Phi^{\nu}_{WB}}\frac{\sigma_{SM}}{\sigma_{\nu N}} < 4.5. \tag{4.10}$$

These result are shown in Fig. 4.30. It should be noted that this calculation

assumes that the downgoing event rate changes linearly with the cross section. Simulations indicate the the event rates follows a form closer to the square root of the neutrino cross section (see 4.9.3 and Table 4.10 for details). The calculations presented above simply expand the results given in [17] to this AMANDA-II UHE limit, without addressing this difference in event rate behavior.

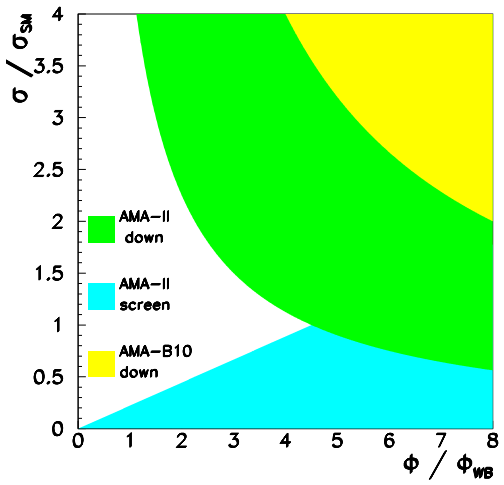

Figure 4.30: Limits to the cross section as a function of Waxman-Bahcall flux. The green and blue areas have been added and together with the yellow area are the regions excluded by this analysis. Figure adapted from [17].

4.9.3 Enhancements to Neutral Current Cross Section

To determine the sensitivity of this UHE analysis to an increased cross section, simulations were performed with the neutral current neutrino-nucleon cross section increased by factors of 10^2, 10^3, and 10^4 and event rates for the Engel et al. [31] GZK flux (labeled "GZK (Engel01)" in Fig. 1.5) and a $2 \times 10^{-8} \times E^{-2}$ GeV cm^{-2} s^{-1} sr^{-1} were calculated (Tables 4.9 and 4.10, respectively).

Event rates at $10^4 \times \sigma_{NC}$ are close to being eliminated at the 90% CL by this analysis. However, a cross section of this size (approximately 0.5 mb at 10^{12} GeV) is already rejected by previous calculations using upper limits on the neutrino

Table 4.9: Number of all flavor neutrino events passing all selection criteria in 456.8 days for an Engel et al. [31] GZK flux simulated with enhanced neutral current cross sections using either the neutrino or shower energy as the generating energy.

σ_{NC} Scale Factor	Number with E_ν	Number with E_{shower}
10^0	0.06	0.44
10^2	0.43	1.7
10^3	2.23	7.9
10^4	4.92	12.3

Table 4.10: Number of all flavor neutrino events passing all selection criteria in 456.8 days for a $2 \times 10^{-8} \times E^{-2}$ GeV cm^{-2} s^{-1} sr^{-1} flux simulated with enhanced neutral current cross sections.

σ_{NC} Scale Factor	Number
10^0	1.2
10^2	7.7
10^3	68.1
10^4	288.2

flux from the RICE experiment [19, 23]. In Anchordoqui et al. [19], event rates for enhanced neutral current cross sections are calculated with the assumption that all the energy of the neutrino is passed to the shower. For comparison, this assumption can be approximated by using the energy of the shower with the most hits, since the hadronic shower generated during neutral current interaction dominates for enhanced neutral current cross sections. With this assumption, a neutral current cross section scaled by 10^3 (0.054 at 10^{12} GeV) is eliminated at the 90% CL by this analysis. The event rates for each cross section scaling for neutrino energy and shower energy weighted samples are shown in Table 4.9. Figure 4.31 shows the scale factor which give an excess of events (i.e. number of events greater than the 90% event upper limit of 5.3 at the final selection level) for the conservative GZK flux from Engel et al. [31] for various neutral current cross section enhancements.

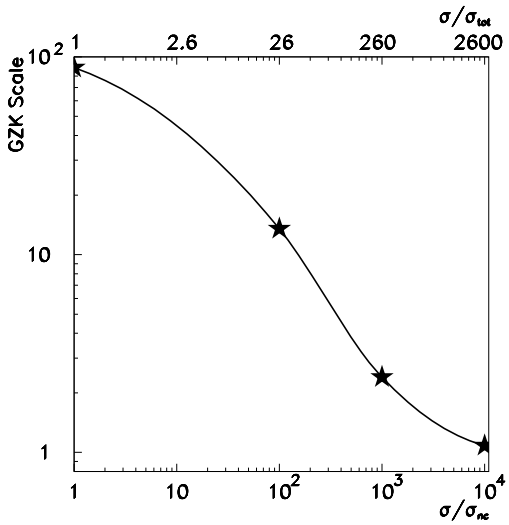

Figure 4.31: Scale factor for Engel et al. [31] GZK flux which causes an excess of events after applying all selection criteria as a function of enhanced neutral current cross section (bottom axis) and total cross section (top axis).

4.9.4 Comparison to Previous Analyses

A previous UHE analysis has been preformed using only the inner 10 strings of the AMANDA-II detector (called AMANDA-B10) using data taken during 1997. This B10 analysis used similar energy-correlated variables to the ones detailed in this work (for a full description see [7]). The B10 analysis used ice properties that were based on an earlier ice model that was clearer than the current model of the ice that was used for this 2000 - 2002 UHE analysis. The average absorption length used for the B10 analysis was ~121 m and the average scattering length was 24 m, compared to an absorption length of ~94 m and a scattering length of 21 m that were used for the AMANDA-II analysis. This led to higher signal and background simulation passing rates. An estimate of the difference in signal passing rate was provided by simulating muon neutrino signal with B10 ice parameters and comparing the E^{-2} passing rate at the final selection level (using selection criteria from this UHE analysis) to signal generated for this UHE AMANDA-II analysis using the current understanding of ice properties. The

Table 4.11: Number of muon neutrino events passing all selection criteria for 2001 simulated with ice properties used in the B10 analysis and ice properties used in this analysis. Signal events are shown for a $10^{-6} \times E^{-2}$ flux (in units of GeV cm^{-1} s^{-1} sr^{-1}).

B10 Ice	AMA-II Ice	Ratio
4.73 ± 0.37	3.32 ± 0.15	1.43 ± 0.13

results are shown with statistical errors in Table 4.11. After correcting for the statistical uncertainty, the ratio of event rates from B10 ice to event rates from AMANDA-II ice is 1.3. When comparing these two analyses, the limit from AMANDA-B10 should be increased by at least a factor of 1.3.

4.10 2000 Analysis

A previous analysis had been performed on the 2000 data and is detailed in the Appendix.

The reconstruction for signal, background and experimental datasets from 2000 was done using all hits from the first 5000 ns, rather than the first hit in each OM. Since the reconstruction algorithms are optimized for only the first hit, this resulted in a poorer reconstruction with a higher likelihood than events from 2001/2002. As a result, the passing rates for E^{-2} signal for 2000 are about 60% of the passing rates for 2001 or 2002. It was too computationally intensive to redo all the reconstructions for 2000. Future analysis may be able to make use of more precise results, but the results from 2000 were still of sufficient quality to merit inclusion in a three year analysis as they were.

Chapter 5

Conclusions

The all-flavor diffuse flux upper limit of

$$E^2\Phi_{90\%CL} \leq 2.7 \times 10^{-7} \text{GeV cm}^{-2} \text{ s}^{-1} \text{ sr}^{-1} \tag{5.1}$$

is the most stringent limit over the energies of 2×10^5 GeV and 10^9 GeV to date. Several predictions of neutrino flux from AGN models has been rejected at the 90% confidence level by this analysis (Table 4.8). This analysis has also placed limits on the fraction of extragalactic MeV background that can be attributed to hidden-core AGNs and has studied the effects of an enhanced neutral current neutrino-nucleon cross section at ultra-high energies.

5.1 Future Outlook

5.1.1 The TWR DAQ

In 2003 the hardware of AMANDA-II was upgraded with the addition of Transient Waveform Recorders (TWR). The TWR system allows the readout of the full pulse in a 10 μs window around the trigger time for each OM. Using this pulse shape, the total number of photoelectrons can be calculated. This is an improvement over the system used for this analysis (the muon DAQ), which only recorded the peak photoelectron value. Additionally, with the TWR system, if enough photoelectrons strike an OM so that it saturates (the OM has a maximum voltage of ~5 V), the magnitude of the pulse can still be estimated from the afterpulse peaks. With the muon DAQ, only eight hits are kept for output, so

these afterpulse peaks are usually lost. If they are retained, there is no amplitude information, so estimation of the number of photoelectrons (N_{pe}) for saturated pulses is very difficult for the muon DAQ. Fig. 5.1 shows the estimated N_{pe} for the

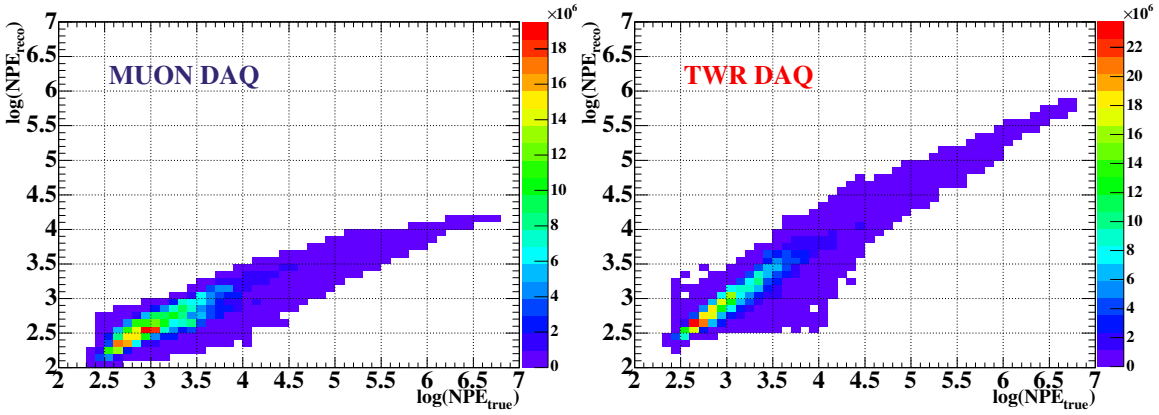

Figure 5.1: Contour plots showing the comparison between reconstructed N_{pe} and true N_{pe} for the muon DAQ (right) and TWR DAQ (left). Figure taken from [72].

muon DAQ and the TWR DAQ versus true N_{pe}. The muon DAQ under estimates the N_{pe} and saturates at lower values than the TWR DAQ.

Being able to accurately count the N_{pe} will aid in the separation of background muon bundles and UHE neutrinos. An analysis is currently underway using data from the TWR DAQ taken in 2003. It's estimated that this analysis may improve the current limits by as much as a factor of two.

5.1.2 The IceCube Detector

Deployment in currently under way on a much larger version of the AMANDA-II detector. The IceCube detector will be a cubic kilometer sized array of 4200 OMs. The OMs will be deployed on 70 strings with 60 OMs on each string with an intra-OM spacing of 17 m. The IceCube detector will extend to greater depths in the ice than the AMANDA-II detector, with a deployment depth between 1400 m and 2400 m. There will be approximately 125 m between each string of OMs. Deployment began in 2004, with 22 of the strings deployed by the end of 2007.

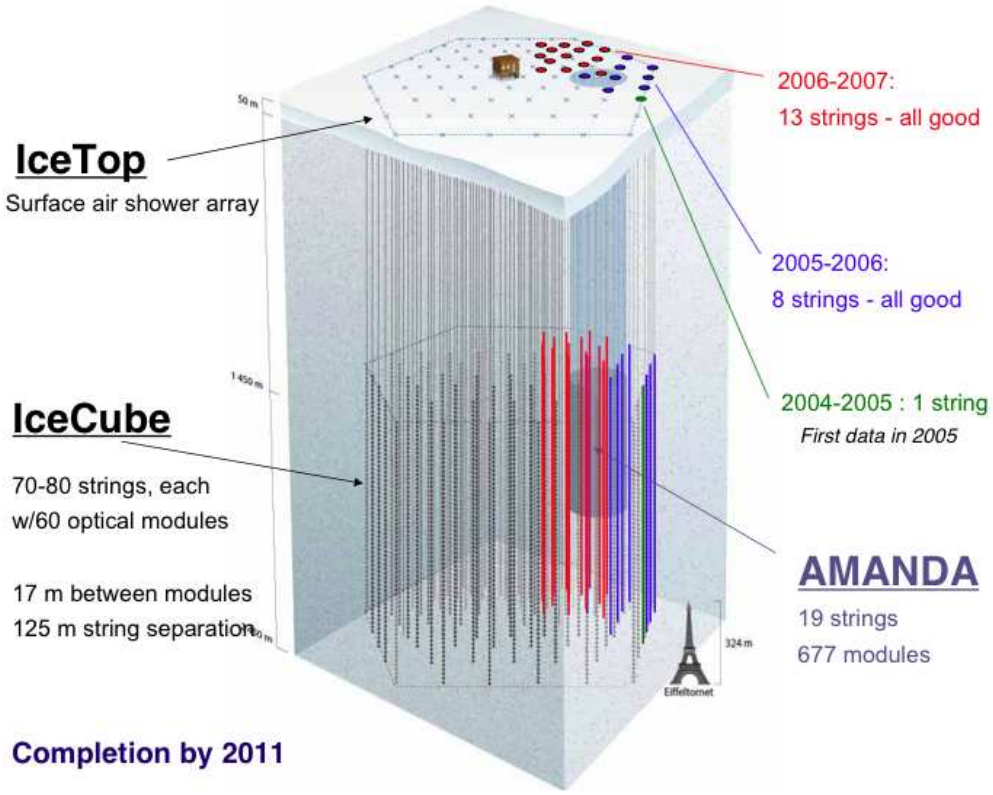

Figure 5.2: The IceCube Detector.

The IceCube detector will use also readout the full waveform in a similar manner to the TWR DAQ described above. The large volume of IceCube will greatly aid the rejection of background. Estimates of the sensitivity of IceCube suggest lower energy diffuse searches (those with energies below ~10^5 GeV) will be improved by a factor of 40 after 1 year of IceCube data taking [14] and existing limits (for a four year livetime) will be improved by an order of magnitude. A similar improvement is expected at ultra-high energies. Including the expected improvement for use of the TWR system, an improvement of roughly a factor of twenty at the highest energies is expected.

Appendix

A Initial 2000 Analysis

An analysis was conducted using only the 2000 data prior to the analysis presented in this work. The selection criteria for the analysis presented in the rest of this work was initially determined using the 2001/2002 datasets. These selection criteria were extended to the year 2000. Both analyses (the single 2000 analysis detailed below and the 2000 - 2002 analysis detailed in the rest of this work) found results that were consistent with background, so for simplicity, only one set of selection criteria were used for all three years, referred to below as the three-year analysis. The paragraphs below are referring to an earlier analysis of just the 2000 data, referred to as the 2000 analysis and detailed in this work for completeness.

The 2000 analysis used a similar strategy as the three-year analysis. Energy variables were used to separate the lower energy background muon bundles from UHE neutrinos. Reconstruction variables were used to distinguish the primarily horizontal UHE signal from the downgoing background.

The filtering up to level 2 of the experiment, background and signal simulation datasets for 2000 was the same as the processing for the three-year analysis described in Chapter 4. The selection criteria are listed in Table A.1 and described below.

After level 2, the data were split into two sets according to the output of a neural net (NN1). NN1 was trained with signal events, with events with energies above 10^8 GeV labeled as signal and events with energies below 10^8 GeV labeled as background. Events with NN1 > 0.9 tended to be higher energy and selection criteria with an emphasis on energy were used to separate signal from background. Events with NN1 $\leq$ 0.9 were lower energy and a mixture of

reconstruction and energy variables were used. Next, a second neural net (NN2) was applied to the datasets. NN2 used two reconstructed zenith angles and the radial distance between the center of gravity of hits and the detector center as input variables and was trained on simulated background and signal events. The next selection criterion required that NN2 > 0.973 for the low-energy datasets and NN2 > 0.84 for the high-energy datasets.

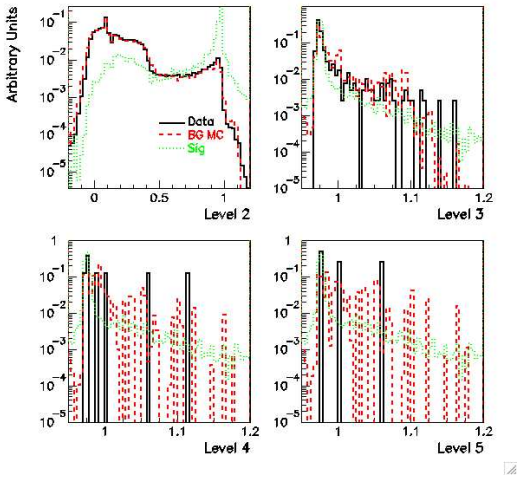

Figure A.3: NN2 distribution for experiment, background and E^{-2} muon neutrino signal simulation at selection levels 2 - 5 of the 2000 analysis.

Next, a selection on NHITS is applied to the low-energy dataset. Then a selection criterion based on the time residuals of the hits is applied. NLATE is the number of hits in an event with a time residual greater than 150 ns and NEARLY is the number of hits with a time residual less than -15 ns. Signal will tend to have more late hits because of afterpulsing, so it will have higher values of NLATE / NEARLY. Next a selection on the distribution of hits around the moment of inertia is applied, with values which show clustering near the top or bottom of the fit track retained. Events with a zenith angle from the UHE bundle reconstruction greater than 70° are discarded in an effort to remove downgoing background muon bundle events. Finally, events with an average hit probability (pha) > 10^{-4}

Table A.1: Selection criteria. "Low energy" and "high energy" refer to events with a NN1 value less then or greater than 0.9, respectively.

Level	"Low Energy"	"High Energy"
0	Preprocessing	Preprocessing
1	F1H < 0.72 NHITS > 160	F1H < 0.72 NHITS > 160
2	F1H < 0.53	F1H < 0.53
3	NN2 > 0.973	NN2 > 0.84
4	NHITS > 565	NN3 > 0.96
5	NLATE/(NEARLY+1) > 50	NCH < 125
6	|smooth(moi)| > 0.15	$F4H_{OPT}$ < 0.12
7	zenith > 70	-
8	$\log_{10}$(pha(HE)) > -0.4	-

are kept.

The level 4 selection criteria for the high-energy dataset used a neural net (NN3) trained on F1H, the zenith angle of an intermediate cascade reconstruction, and the likelihood of the Pandel reconstruction. Selection level 5 for the high-energy dataset retains events with NCH > 125. Finally, selection criterion using the fraction of optical OMs with four hits ($F4H_{OPT}$) was applied.

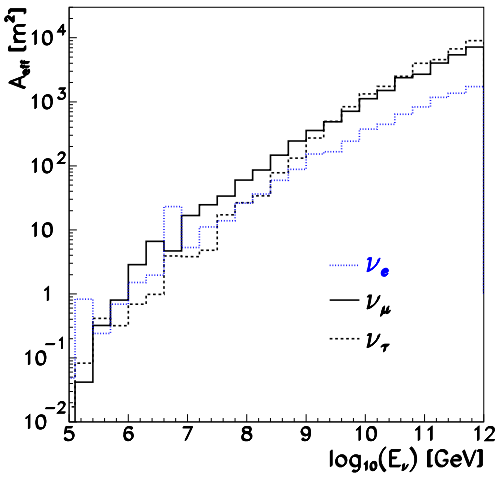

Figure A.4: Effective area for electron, muon and tau neutrinos for the 2000 analysis after all selection criteria were applied.

After applying all selection criteria, 1.3 background events were expected in a

livetime of 138.8 days, with an uncertainty of 1.6 (see Section 4.8 for a description of simulation uncertainties). Fig. A.4 shows the effective neutrino area after all selection criteria were applied. The 90% CL average event upper limit given by Feldman & Cousins [32] for 1.3 events is 3.49, which gave a sensitivity of 3.7×10^{-7} GeV cm^{-2} s^{-1} sr^{-1}, with 90% of the E^{-2} signal found in the energy range 1.8×10^5 GeV to 1.8×10^9 GeV.

Five events were found in the 2000 data. This was consistent with a background expectation of up to three events (including systematic uncertainties). This led to an all flavor limit on the diffuse neutrino flux of

$$9.9 \times 10^{-7} \text{ GeVcm}^{-2} \text{ s}^{-1} \text{ sr}^{-1} \tag{A.2}$$

valid over the energy range of 1.8×10^5 GeV to 1.8×10^9 GeV. These results are superceded by the results in the rest of this work.

Bibliography

[1] "To read makes our speaking English good." – Xander Harris.

[2] R. Abbasi et al. Observation of the ankle and evidence for a high-energy break in the cosmic ray spectrum. *Physics Letters B*, 619:271–280, 2005.

[3] R. Abbasi et al. Observation of the GZK cutoff by the HiRes experiment. (astro-ph/0703099v1), 2007.

[4] J. Abraham et al. Properties and performance of the prototype instrument for the Pierre Auger Observatory. *Nuclear Instruments and Methods in Physics Research A*, 523:50–95, 2004.

[5] A. Achterberg et al. Multi-year search for a diffuse flux of muon neutrinos with AMANDA-II. *Physical Review D*, 2007. in publication.

[6] M. Ackermann et al. Search for neutrino-induced cascades with AMANDA. *Astroparticle Physics*, 22:127–138, 2004.

[7] M. Ackermann et al. Flux limits on ultra high energy neutrinos with AMANDA-B10. *Astroparticle Physics*, 22:339–353, 2005.

[8] M. Ackermann et al. Optical properties of deep glacial ice at the south pole. *Journal Of Geophysical Research*, 111:D13203, 2006.

[9] M. Ahlers et al. Neutrinos as a diagnostic of cosmic ray galactic-extragalactic transition. *Physics Review D*, 72:023001, 2005.

[10] J. Ahrens et al. Limits on diffuse fluxes of high energy extraterrestrial neutrinos with the AMANDA-B10 detector. *Physics Review Letters*, 90:251101, 2003.

[11] J. Ahrens et al. Search for neutrino-induced cascades with AMANDA. *Physical Review D*, 67:012003, 2003.

[12] J. Ahrens et al. Search for point sources of high-energy neutrinos with AMANDA. *Astrophysical Journal*, 583:1040–1057, 2003.

[13] J. Ahrens et al. Muon track reconstruction and data selection techniques in AMANDA. *Nuclear Instruments and Methods in Physics Research A*, 524:169–194, 2004.

[14] J. Ahrens et al. Sensitivity of the IceCube detector to astrophysical sources of high energy muon neutrinos. *Astroparticle Physics*, 20:507–532, 2004.

[15] J. Alvarez-Muñiz, J. Feng, F. Halzen, T. Han, and D. Hooper. Detecting microscopic black holes with neutrino telescopes. *Physical Review D*, 65:124015, 2002.

[16] L. Anchordoqui, A. Cooper-Sakar, D. Hooper, and S. Sakar. Probing low-x QCD with cosmic neutrinos at the pierre auger observatory. *Physics Review D*, 74:043008, 2006.

[17] L. Anchordoqui, J. Feng, and H. Goldberg. Particle physics on ice: Constraints on neutrino interactions far above the weak scale. *Physical Review Letters*, 96:021101, 2006.

[18] L. Anchordoqui, J. Feng, H. Goldberg, and A. Shapere. Black holes from cosmic rays: Probes of extra dimensions and new limits on TeV-scale gravity. 2002. hep-ph(0112247v3).

[19] L. Anchordoqui, Z. Fodor, S. Katz, A. Ringwald, and H. Tu. Upper bounds on the neutrino-nucleon inelastic cross section. *Journal of Cosmology and Astroparticle Physics*, 6(13):1–20, 2005.

[20] E. Andres et al. Observation of high-energy neutrinos using cherenkov detectors embedded deep in antarctic ice. *Nature*, 410:441–443, 2000.

[21] V. Aynutdinov et al. Search for a diffuse flux of high-energy extraterrestrial neutrinos with the NT200 neutrino telescope. *Astroparticle Physics*, 25:140–150, 2006.

[22] J. Bahcall and E. Waxman. High energy neutrinos from astrophysical sources: An upper bound. *Physics Review D*, 59:023002, 1998.

[23] V. Barger, P. Huber, and D. Marfatia. Ultra high energy neutrino-nucleon cross section from cosmic ray experiments and neutrino telescopes. *Physics Letters B*, 642:333–341, 2006.

[24] S. Barwick et al. Constraints on cosmic neutrino fluxes from the antarctic impulsive transient antenna experiment. *Physics Review Letters*, 96:171101, 2006.

[25] D. Bergman and J. Belz. Cosmic rays: The second knee and beyond. *Journal of Physics G: Nuclear and Particle Physics*, 2007. in publication, astro-ph(07043721v1).

[26] S. Chekanov et al. An NLO QCD analysis of inclusive cross-section and jet-production data from the ZEUS experiment. *The European Physical Journal C*, 42:1–16, 2005.

[27] J. Chiang, C. Fichtel, C. von Montigny, P. Nolan, and V. Petrosian. The evolution of gamma-ray loud active galactic nuclei. *The Astrophysical Journal*, 452:156–163, 1995.

[28] D. Chirkin and W. Rhode. Muon monte carlo: a high-precision tool for muon propagation through matter. (hep-ph/0407075), 2004.

[29] The AMANDA Collaboration. 2001. http://www-zeuthen.desy.de/nuastro/software/siegmund/siegmund_old/pro/siegmund.html.

[30] The IceCube Collaboration. 2007. http://internal.icecube.wisc.edu/amanda/software/sieglinde/.

[31] R. Engel, D. Secker, and Stanev T. Neutrinos from propagation of ultra-high energy protons. *Physics Review D*, 64:093010, 2001.

[32] G. Feldman and F. Cousins. Unified approach to the classical signal analysis of small signals. *Physical Review D*, 57(7):3873, 1998.

[33] J. Feng and A. Shapere. Black hole production by cosmic rays. *Physical Review Letters*, 88(2):021303, 2002.

[34] T. Gaisser, F. Halzen, and T. Stanev. Particle astrophysics with high energy neutrinos. *Physics Reports*, 258:173–236, 1995.

[35] R. Gandhi, C. Quigg, M. Reno, and I. Sarcevic. Ultrahigh-energy neutrino interactions. *Astroparticle Physics*, 5:81–110, 1996.

[36] R. Gandhi, C. Quigg, M. Reno, and I. Sarcevic. Neutrino interactions at ultrahigh energies. *Physics Review D*, 58:093009, 1998.

[37] R. Glasstetter et al. Analysis of electron and muon size spectra of EAS. *Proceedings of the 26th International Cosmic Ray Conference, Utah, USA*, HE.2.2.03, 1999.

[38] K. Greisen. End to the cosmic ray spectrum? *Physics Review Letters*, 16:748–750, 1966.

[39] F. Halzen and E. Zas. Neutrino fluxes from active galaxies: A model-independent estimate. *The Astrophysical Journal*, 488:669–674, 1997.

[40] N. Hayashida et al. Observation of a very energetic cosmic ray well beyond the predicted 2.7 K cutoff in the primary energy spectrum. *Physical Review Leters*, 73:3491–3494, 1994.

[41] D. Heck. The air shower simulation program CORSIKA. (DESY-PROC-1999-01):227, 1999.

[42] E. Henley and J. Jalilian-Marian. Ultra-high energy neutrino-nucleon scattering and parton distributions at small x. (hep-ph/0512220v1), 2005.

[43] G. Hill. Application of importance sampling to the atmospheric muon generator "basiev". *AMANDA-IR 20000904*, 2000.

[44] G. Hill, A. Karle, and P. Desiarti. Evidence for insufficient absorption in the AMANDA Monte Carlo, 2001. http://icecube.wisc.edu/ ghill/absorption/absorption.html.

[45] G. Hill and K. Rawlins. Unbiased cut selection for optimal upper limits in neutrino detectors: the model rejection potential technique. *Astroparticle Physics*, 19:393–402, 2003.

[46] S. Hundertmark. Proceedings of the 1^{st} Workshop Methodical Aspects of Underwater/Ice Neutrino Telescopes, Zeuthen, Germany. 1998.

[47] J. Hörandel. On the knee in the energy spectrum of cosmic rays. *Astroparticle Physics*, 19:193–230, 2003.

[48] S. Jadach. The tau decay library TAUOLA: Version 2.4. *Computer Physics Communications*, 76:361, 1993.

[49] O. Kalashev, V. Kuzmin, D. Semikoz, and G. Sigl. Ultrahigh-energy cosmic rays from neutrino emitting acceleration sources? *Physical Review D*, 65:103003, 2002.

[50] O. Kalashev, V. Kuzmin, D. Semikoz, and G. Sigl. Ultrahigh-energy neutrino fluxes and their constraints. *Physical Review D*, 66:063004, 2002.

[51] A. Karle. Simulation and analysis methods for large neutrino telescopes. (DESY-Proc-1999-01):174–185, 1999.

[52] S. Klein. Cascades from ν_e above 10^{20} eV. (astro-ph/0412546v1), 2004.

[53] M. Kowalski and A. Gazizov. ANIS: High energy neutrino generator for neutrino telescopes. *Computer Physics Communications*, 171:203–213, 2005.

[54] I. Kravchenko et al. RICE limits on the diffuse ultrahigh energy neutrino flux. *Physics Review D*, 73:082002, 2006.

[55] K. Kutak and J. Kwieciǹski. Screening effects in the ultra high energy neutrino interactions. (hep-ph/0303209v4), 2007.

[56] L. Landau and I. Pomeranchuk. Limits of applicability of the theory of bremsstrahlung by electrons and production of pairs at high energies. *Doklady Akademii Nauk SSSR*, 92:535, 1953.

[57] J. Learned and K. Mannheim. High-energy neutrino astrophysics. *Annual Review Nuclear Particle Science*, 50:679–749, 2000.

[58] J. Learned and S. Pakvasa. Detecting ν_τ oscillations at PeV energies. *Astroparticle Physics*, 3:267–274, 1995.

[59] P. Lipari. Lepton spectra in the earth's atmosphere. *Astroparticle Physics*, 1:195–227, 1993.

[60] P. Lipari and T. Stanev. Propagation of multi-TeV muons. *Physical Review D*, 44(11):3543–3554, 1991.

[61] K. Mannheim. High-energy neutrinos from extragalactic jets. *Astroparticle Physics*, 3:295–302, 1995.

[62] K. Mannheim, R. Protheroe, and J. Rachen. Cosmic ray bound for models of extragalactic neutrino production. *Physical Review D*, 63:023003, 2000.

[63] M. McConnell et al. Latest COMPTEL results on Galactic black hole candidates. *Advances in Space Research*, 19:25–28, 1997.

[64] A. Migdal. *Journal of Experimental and Theoretical Physics*, 5:527, 1957.

[65] S. Movit, P. Roth, P. Toale, and D. Cowen. Downgoing muon t_0 calibration. *AMANDA-IR 20050101*, 2005.

[66] A. Mucke, R. Engel, R. Protheroe, and T. Stanev. Monte carlo simulations of photohadronic processes in astrophysics. *Computer Physics Communications*, 124:290–314, 2000.

[67] Particle Data Group. Review of particle physics. *Physics Letters B*, 592:186–234, 2004.

[68] A. Pohl. *A Statistical Tool for Finding Non-Particle Events from the AMANDA Neutrino Telescope*. PhD thesis, Uppsala Universitet, 2004. Selection procedure outlined at http://www5.hik.se/personal/tpoar/Flare_proposal.html.

[69] R. Protheroe. High energy neutrinos from blazars. (astro-ph/9607165), 1996.

[70] G. Sigl, S. Lee, P. Bhattacharjee, and S. Yoshida. Probing grand unified theories with cosmic-ray, gamma-ray, and neutrino astrophysics. *Physics Review D*, 59:043504, 1998.

[71] A. Silvestri. Performance of AMANDA-II using transient waveform recorders. *Proceedings of the 29th International Cosmic Ray Conference, Pune, India*, pages 431–434, 2005.

[72] A. Silvestri. First results from AMANDA using the TWR system. *Proceedings of International School of Cosmic Ray Astrophysics, 15th Course: "Astrophysics at Ultra-high Energies", Erice, Italy*, 2007.

[73] P. Sommers. First estimate of the primary cosmic ray energy spectrum above 3 EeV from the pierre auger observatory. *Proceedings of the 29th Internation Cosmic Ray Conference*, 7:387–390, 2005.

[74] P. Sreekumar et al. EGRET observations of the extragalactic gamma-ray emission. *The Astrophysical Journal*, 494:523–534, 1998.

[75] F. Stecker. Note on high-energy neutrinos from active galactic nuclei cores. *Physics Review D*, 72:107301, 2005.

[76] F. Stecker, C. Done, M. Salamon, and P. Sommers. Erratum: High-energy neutrinos from active galactic nuclei. *Physics Review Letters*, 69:2738, 1991.

[77] F. Stecker and M. Salamon. High energy neutrinos from quasars. *Space Science Reviews*, 75:341–355, 1996.

[78] P. Sudhoff. Transmission measurements with AMANDA and evaluation for IceCube. *AMANDA-IR 20010701*, 2001.

[79] F. Tegenfeldt and J. Conrad. On Bayesian treatment of systematic uncertainties in confidence interval calculation. *Nuclear Instruments and Methods in Physics Research A*, 539:407–413, 2005.

[80] E. Waxman. Cosmological origin for cosmic rays above 10^{19} eV. *Astrophysical Journal*, 452:L1, 1995.

[81] E. Waxman and J. Bahcall. High energy neutrinos from astrophysical sources: An upper bound. *Physical Review D*, 59:023002, 1998.

[82] T. Weiler. Resonant absorption of cosmic-ray neutrinos by the relic-neutrino background. *Physical Review Letters*, 49(3), 1982.

[83] B. Wiebel-Sooth, P. L. Biermann, and H. Meyer. Cosmic rays VII. individual element spectra: prediction and data. 1997.

[84] R. Wischnewski. Performance of the AMANDA-II detector. *Proceedings of the 26th International Cosmic Ray Conference, Utah, USA*, HE.4.2.07, 1999.

[85] K. Woschnagg. Matching and combining laser and drill geometries, 2000. http://icecube.berkeley.edu/kurt/interstring/matchgeo.html.

[86] K. Woschnagg. Preliminary (non-optical) calibration of strings 14 to 19. *AMANDA-IR 20001002*, 2000.

[87] S. Yoshida, G. Sigl, and Lee S. Extremely high energy neutrinos, neutrino hot dark matter, and the highest energy cosmic rays. *Physics Review Letters*, 81:5505–5508, 1998.

[88] S. Young. *A Search for Point Sources of High Energy Neutrinos with the AMANDA-B10 Neutrino Telescope*. PhD thesis, University of California, Irvine, 2004.

[89] E. Zas, F. Halzen, and R. Vázquez. High energy neutrino astronomy: Horizontal air shower arrays versus underground detectors. *Astroparticle Physics*, 1:297–315, 1993.

[90] G. Zatsepin and A. Kuzmin. Upper limit of the spectrum of cosmic rays. *Journal of Experimental Theory Letters*, 4:78–80, 1966.